Computational Science of Turbulent Mixing and Combustion

Yosuke Shimada

Submitted for the Degree of PhD

Department of Fluid Mechanics and Computational Science
School of Engineering
Cranfield UNIVERSITY

2010

Cranfield University

School of Engineering

PhD Thesis

Academic Year: 2009-2010

Yosuke Shimada

Computational Science of Turbulent Mixing and Combustion

Supervisors: Professor Dimitris Drikakis, Dr Ben Thornber

September 2010

This thesis is submitted in partial fulfilment of the requirements
for the Degree of PhD

Abstract

Implicit Large Eddy Simulation (ILES) with high-resolution and high-order computational modelling has been applied to flows with turbulent mixing and combustion.

Due to the turbulent nature, mixing of fuel and air and the subsequent combustion still remain challenging for computational fluid dynamics. However, recently ILES, an advanced numerical approach in Large Eddy Simulation methods, has shown encouraging results in prediction of turbulent flows. In this thesis the governing equations for single phase compressible flow were solved with an ILES approach using a finite volume Godunov-type method without explicit modelling of the subgrid scales. Up to ninth-order limiters were used to achieve high order spatial accuracy.

When simulating non chemical reactive flows, the mean flow of a fuel burner was compared with the experimental results and showed good agreement in regions of strong turbulence and recirculation. The one dimensional kinetic energy spectrum was also examined and an ideal $k^{-5/3}$ decay of energy could be seen in a certain range, which increased with grid resolution and order of the limiter. The cut-off wavenumbers are larger than the estimated maximum wavenumbers on the grid, therefore, the numerical dissipation sufficiently accounted for the energy transportation between large and small eddies. The effect of density differences between fuel and air was investigated for a wide range of Atwood number. The mean flow showed that when fuel momentum fluxes are identical the flow structure and the velocity fields were unchanged by Atwood number except for near fuel jet regions. The results also show that the effects of Atwood number on the flow structure can be described with a mixing parameter.

In combustion flows simulation, a non filtered Arrhenius model was applied for the chemical source term, which corresponds to the case of the large chemical time scale compared to the turbulent time scale. A methane and air shear flow simulation was performed and the methane reaction rate showed non zero values against all temperature ranges. Small reaction rates were observed in the low temperature range due to the lack of subgrid scale modelling of the chemical source term. Simulation was also performed with fast chemistry approach representing the case of the large turbulent time scale compared to the chemical time scale. The mean flow of burner flames were compared with experimental data and a fair agreement was observed.

Acknowledgements

Firstly I would like to express my thanks to my supervisor Professor Dimitris Drikakis for his advice and supervision throughout the period of this work from October 2007 to September 2010. He guided me the direction of the research with his wide range of knowledge and lead me by his passion for science.

My gratitude also goes to my supervisor Ben Thornber for his advice and support. He literally kept his office door open, and not only has he shared his sophisticated ideas and experience but also encouraged me to face seemingly profound and challenging academic problems.

I would also like to thank other members of our Fluid Mechanics and Computational Science group of Cranfield University, particularly Marco Hahn and Sanjay Patel for fruitful discussions we had regarding computational physics and the developing in-house computational fluid dynamics code.

My colleagues, Kashif Iqbal, Solange Baena, Paul Jemitola, Baba Omar, Ting Ding, Tareq Alawadi, Guido Monterzino, Ramey Jamil, Henry 'Leo' Leonardo, Mudassir Lone, Hakim Oheda, Ken Lai, Peter Thomas, Zeeshan Rana, Mathis Dahlqvist and Tommaso Oggian are appreciated for the time we shared in and out of our laboratory. My life in peaceful Cranfield was excited by their friendship and their interests in science.

Finally I wish to thank my family for their support. The progress of the research coincided with the growing up of my son, Yuki, and the hours I spent with him encouraged me to finish this arduous work.

Yosuke Shimada

Contents

List of Figures

List of Tables

Nomenclature

Acronyms

CFD Computational Fluid Dynamics

CFL Courant-Friedrichs-Lewy

DNS Direct Numerical Simulation

HLLC Harten, Lax and van Leer plus Contact wave

ILES Implicit Large Eddy Simulation

LES Large Eddy Simulation

MEA Modified Equation Analysis

MILES Monotone Integrated Large Eddy Simulation

MUSCL Monotonic Upwind Scheme for Scalar Conservation Lows

RANS Reynolds Average Navier-Stokes Equations

rms root mean square

TNF International Workshop on Measurement and Computation of Turbulent Non-premixed Flames

TVD Total Variation Diminishing

WENO Weighted Essentially Non-Oscillatory scheme

Latin Letters

I Unit tensor

P Stress tensor

q Heat flux

E Inviscid flux vector

$\mathbf{m}$	Commutation error vector
$\mathbf{T}$	Subgrid scale tensor
$\mathbf{U}$	Variable array
$\mathbf{u}$	Velocity vector
a	Speed of sound
At	Atwood number
C	Constant
C_p	Specific heat capacity for constant pressure
C_v	Specific heat capacity for constant volume
D	Diameter of the Sydney bluff body/swirl burner
D_i	Diffusion coefficient of mixture
Da	Damköhler number
E	Total energy
E_a	Activation energy
E_k	Kinetic energy spectrum
f	Mixture fraction
h	Total enthalpy
k	Wavenumber
l	Length scale
l_t	Integral length scale
Le	Lewis number
N	Number of cells in a direction
p	Pressure
Pr	Prandtl number
q	Number of sample stencils in WENO scheme
r	Radial direction of a cylindrical coordinate

r_L,r_R	Slope of the conserved variables in limiter at the left and right side of the interface, respectively
Re	Reynolds number
S_L	Laminar flame speed
S_T	Turbulent flame speed
Sc_t	Turbulent Schmidt number
SN	Swirl number
T	Temperature
t	Time
u	Velocity component
V_{fl}	Flammable mixture volume
W	Molecular weight
X	Mole fraction
x, y, z	Cartesian direction
Y	Mass fraction
Z	Element mass fraction
z	Axial direction of a cylindrical coordinate

Greek Symbols

α	Volume fraction
β	Velocity decay rate
Δ	Cell width
δ	Flame thickness
ϵ	Dissipation rate
η_k	Kolmogorov scale
γ	Specific heat ratio
κ	Thermal conductivity

κ_{SGS}	Segregation factor
μ	Dynamic viscosity
ν	Kinematic viscosity
ν_k	Coefficient of molecular ratio under stoichiometric reaction of species k
ω	Chemical source term
ϕ	Limiter function
ψ	Variable
ρ	Density
τ	Viscous tensor
τ_m	Chemical reaction time scale
τ_r	Mixing time scale
τ_{tr}	Truncation error vector
θ	Normalised temperature
φ	Molecular mixing parameter
ξ_{ij}	Mass ration of molecule i to species j

CHAPTER 1

Introduction

1.1 Overview

'Turbulence is the most important unsolved problem of classical physics.' said Richard Feynman, who was awarded the Nobel Prize in 1965. Forty five years has passed since then, and turbulence still remains a major research topic in the field of science and engineering. One can imagine that the inherent and typical characteristics of turbulence are randomness of the flow motion and the wide range of flow scales. This is easily perceived and therefore, it has been well recognised since before the 20th century when basic turbulence theory was mathematically and physically formulated. For example, the random direction of fluid motion is clearly depicted in Figure 1.1 (left). The deformed clouds in Figure 1.1 (right) imply that the painter knew the basic idea of the turbulent flow structure containing large and small eddies.

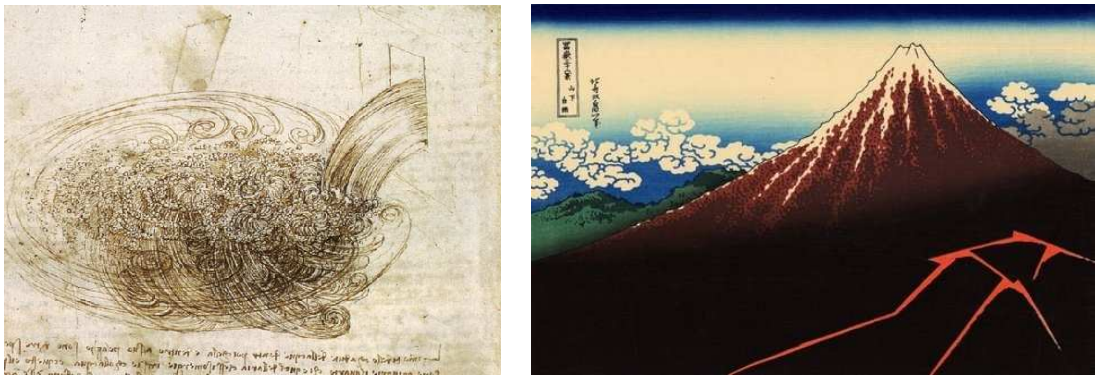

Figure 1.1: A sketch by Leonard da Vinci, around 1515 (left). A print of Hokusai Katsushika, around 1831 (right)

In the past decades numerical simulation has contributed significantly to our knowledge of turbulence. It is common in engineering to use commercial software for designing, development and analysis of fluid dynamic aspects of products. However, understanding the underlying physics and accurately predicting these characteristics are still challenging even with current high power computational tools. Inspecting the

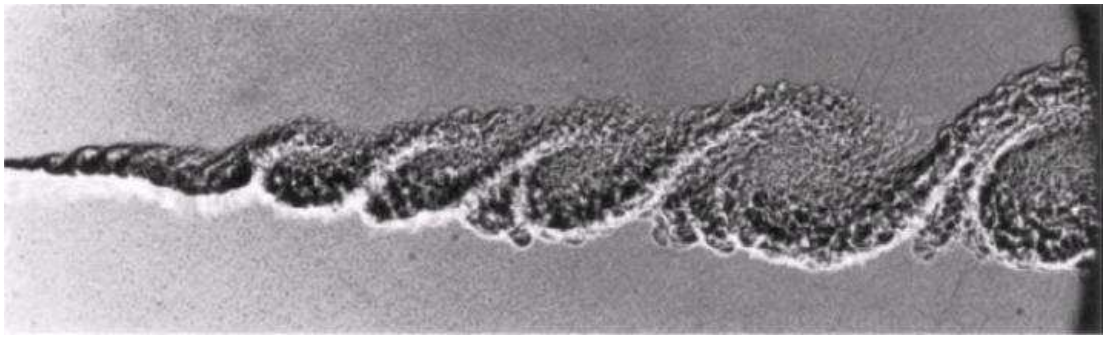

Figure 1.2: Shadowgraph of a turbulent shear flow [11]

experimental photo of Figure 1.2 it can be seen that although the small and large scales look similar their flow structure differ significantly. A typical computational problem is the handling of these different flow scales.

Combustion is another complex problem that has not been fully understood. It includes series of physical phenomena: mixing of the fuel and oxidiser, ignition with chemical reaction and flame propagation, each of these are a very complex process. Time scales of the chemical reactions cause further difficulty. They are typically much shorter than that of fluid dynamics, but for some cases, e.g., NOx formation and supersonic combustion the time scales can be of the same order.

When engineering combustion problems are considered, e.g., plume of jet engine and low NOx emission burners (as shown in Figure 1.3) they are normally categorised in turbulent combustion. This is because turbulence can affect flame structure dynamically, and conversely, chemical reaction can cause instability of the fluids and increase turbulence. Therefore, turbulence and combustion can not be decoupled in real physical phenomena. Difficulties of combustion flow simulation can be summarised as follows:

- Interaction between chemistry and fluid dynamics. Since combustion processes involve a wide range of chemical time and length scales, coupling or decoupling technique to turbulence is the key.
- Modelling of chemical reaction mechanism. Even a simple methane-air combustion may contain hundreds of species and chemical reactions, which demands either enormous computational resource or a simplified model.

This thesis is concerned with the numerical simulation of turbulent gas mixing and combustion. A simple and typical engineering application of this topic is a gas turbine combustor. In most areas of gas turbine engine developments, numerical simulation plays a crucial role. Laminar flow simulation can be used as a main designing tool, particularly in the beginning of the design process of components, such as compressors and turbines, though these flows include turbulence. However, this is not the case for combustors since the combustor flows are predominantly turbulent. Effective and

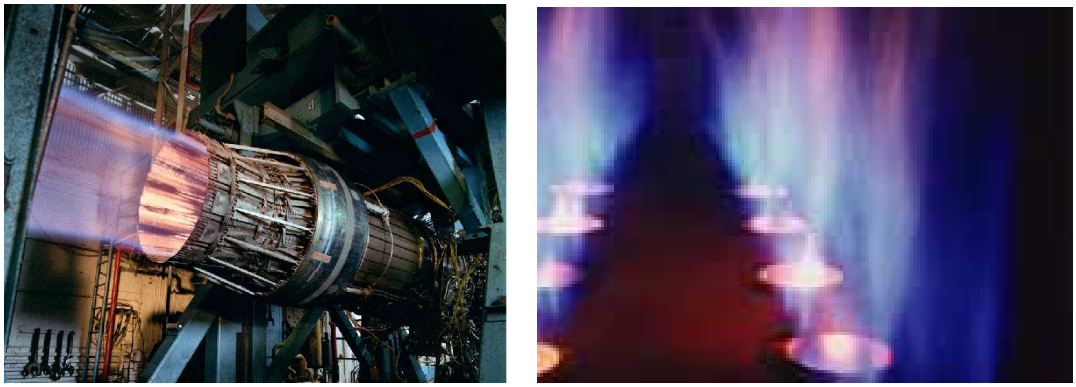

Figure 1.3: Ground test of a jet engine (`http://www.pw.utc.com`) (left) and low NOx emission burners (`http://www.furnace.co.jp`) (right)

accurate computational methods for the turbulent combustion did not exist, therefore, past experience and empirical data still have much importance [52]. As a result, combustor performance cannot be predicted accurately in a development process.

However, the situation has been changing. With the drastic increase of computational power, turbulent combustion has become a problem which can be handled more accurately with reasonable computational resources. Furthermore, advanced computational approach for the turbulent flow has been developed and validated and now, it is ready to be applied to turbulent combustion. With this numerical method, called high-resolution Implicit Large Eddy Simulation (ILES), fuel and air mixing flow and combustion can be simulated.

Regarding the simulation test case geometry, turbulent mixing and chemical reactions in a combustor mainly take place in the near region of the fuel injectors. The primary combustor performance parameters such as combustion gas temperature and fuel consumption rate can be controlled by fuel and air jet injection. Furthermore, swirling and recirculating flows of the injector have been of great interest to industry as they play an important role in flame stabilisation within gas turbine combustors. Hence, the target geometry of this research focuses on the turbulent jet flows.

A brief summary of turbulence is described in the following section. Next, conventional numerical methods are presented followed by research objectives with some information of the thesis structure and a publication list from this research.

1.2 Descriptions of Turbulence

An idea of energy cascade was introduced to handle the relation between turbulent energy distribution and turbulent scales. This is known as Richardson's hypothesis and has become a fundamental idea for most of all theoretical, experimental and computational research on turbulence.

Richardson's hypothesis assumes turbulent flow consists of coherent eddies of various sizes, where large eddies break down into small ones, and in turn, the small eddies break down further into smaller eddies. In this process, energy transfers from the large eddies to small eddies without any loss. This cascade is driven purely by inertial forces and hence, the large scale eddies are not affected by viscous forces. With the decrease in the size of eddies the Reynolds number, which is a nondimensional number representing the relative effect of inertial forces to viscous forces, reduces. When the eddies are broken into the smallest size corresponding to the order of the Reynolds number unity, fluid viscosity works as a driving force to dissipate energy into heat. Therefore, without energy injection, the eddies of all sizes continuously break down and the energy is dissipated. Thus, turbulent flows are essentially dissipative.

This hypothesis was further developed [51] and a mathematical formulation was given. Assuming the energy transfers from the largest scale with integral length scale l_t, to the smallest one (the Kolmogorov length scale η_k) a Reynolds number can be introduced for each turbulent scale as:

$$Re = \frac{u' l}{\nu} \tag{1.2.1}$$

where u' is the turbulent velocity of the motion, which can be expressed as the difference between exact velocity and mean velocity. ν is the flow kinematic viscosity, and l is the length scale, $\eta_k < l < l_t$. The amount of energy transfer from one scale to another is constant and is given by the dissipation ϵ of kinetic energy. Estimating this dissipation as the ratio of kinetic energy u^2, and eddy turn over time scale l/u, yields:

$$\epsilon \approx \frac{u^3}{l} \tag{1.2.2}$$

When the Reynolds number is unity, the Kolmogorov scale is evaluated by viscosity and dissipation rate:

$$\eta_k \approx \left(\frac{\nu^3}{\epsilon}\right)^{1/4} \tag{1.2.3}$$

By considering the above equations, the ratio of the integral length scale to the Kolmogorov length scale can be obtained:

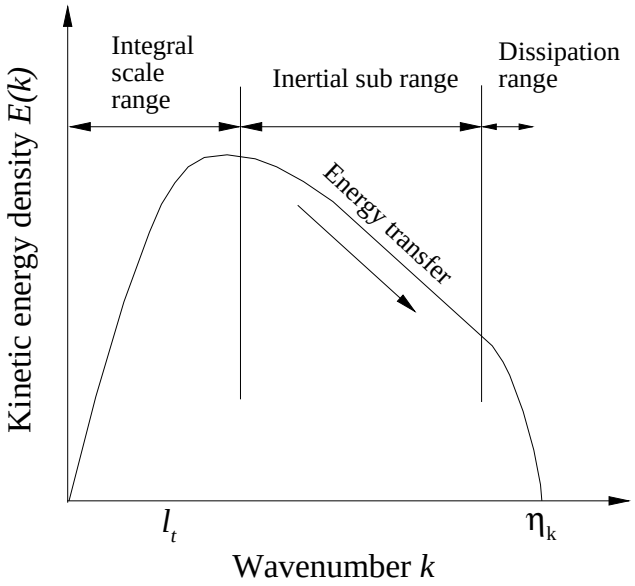

Figure 1.4: Schematic of a kinetic energy spectrum plotted with logarithmic scales

$$\frac{l_t}{\eta_k} \approx Re^{3/4} \tag{1.2.4}$$

A kinetic energy spectrum analysis can now be introduced. The energy contained in a length scale corresponding to wavenumber k can be described in the Fourier space $E_k(k)$. A schematic of a typical kinetic energy spectrum is shown in Figure 1.4.

The energy is accumulated in the low wavenumber range, corresponding to the large scales. In the middle range, inertial forces control the energy and the energy transfers successively to smaller scales according to the cascade hypothesis. This region is called the inertial sub range. Finally, in the high wavenumber range the energy falls into the Kolmogorov scales and dissipates by viscosity. This is called the dissipation range. Through dimensional analysis the form of the energy spectrum in the inertial sub range can be expressed with a constant C:

$$E_k(k) = C\epsilon^{2/3}k^{-5/3} \tag{1.2.5}$$

Although the concept of an energy cascade and Kolmogorov formulation has not been theoretically proven, it has been verified by experimental measurements, e.g., in Figure 1.5. The figure shows that the energy transfer is independent of the large flow scale, and that the energy dissipates in proportion to a $k^{-5/3}$ law in the inertial sub range.

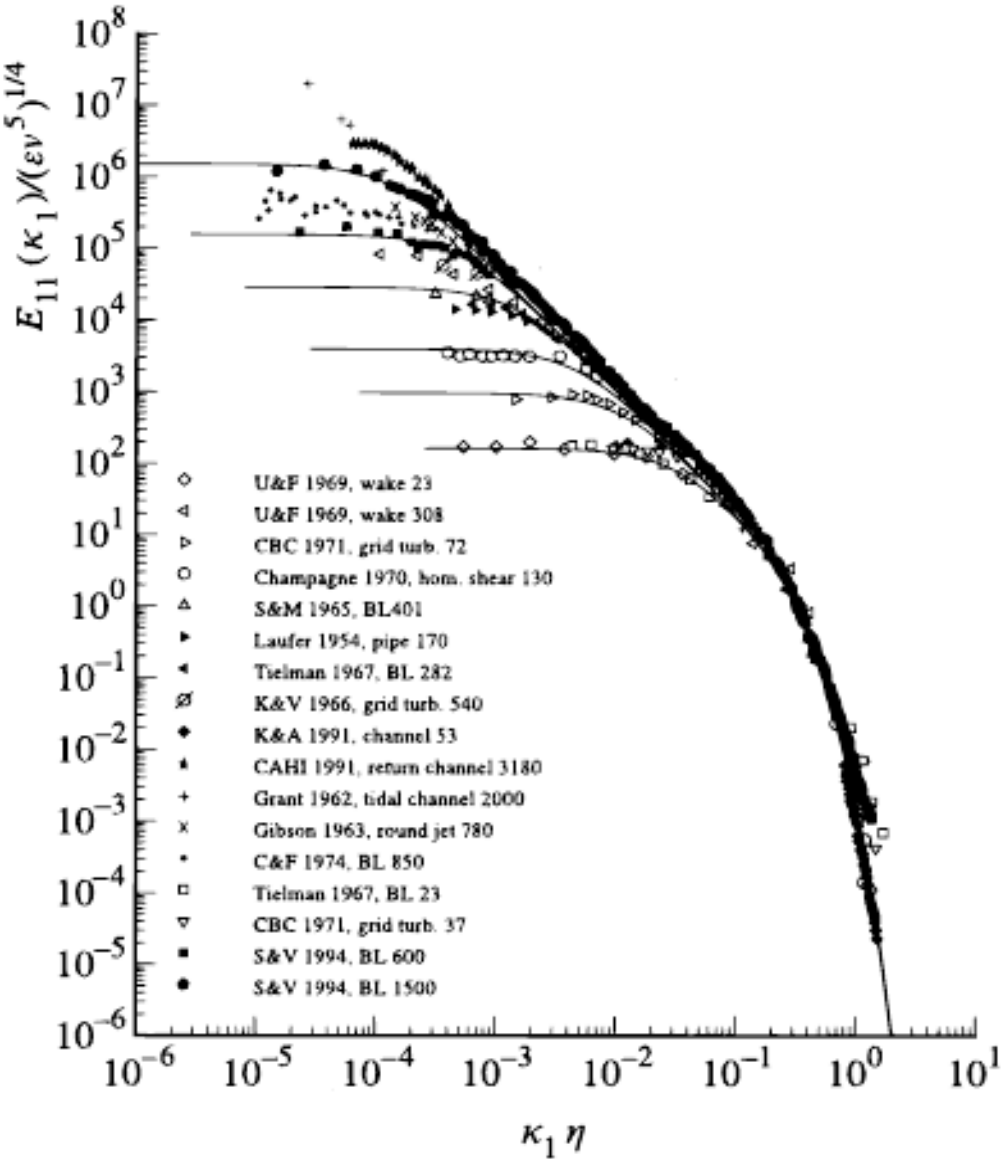

Figure 1.5: Kinetic energy profile obtained by various experiments [72]

1.3 Conventional Numerical Approaches

Numerical research on turbulent flows has progressed with the development of Computational Fluid Dynamics (CFD) techniques and the recent increase in computational power. Within the context of CFD, there are three main approaches: Direct Numerical Simulation (DNS), Reynolds Averaged Navier-Stokes Simulation (RANS) and Large Eddy Simulation (LES). These approaches differ in how precisely they describe eddies.

1.3.1 Direct Numerical Simulation

DNS is based on the simplest concept, i.e., to solve eddies of all scale contained in the flow. Since DNS results are ideally more accurate than other techniques they are often used for comparison and validation of newly developed numerical methods. In the computation of a compressible viscous flow, the momentum equation of the instantaneous flow is solved:

$$\frac{\partial \rho \mathbf{u}}{\partial t} + \nabla \cdot (\rho \mathbf{u}\mathbf{u}) + \nabla p = -\nabla \cdot \tau \tag{1.3.1}$$

where $\mathbf{u}$, ρ, p and τ stand for velocity vector, density, static pressure and viscous tensor, respectively.

However, a critical problem for DNS is the computational cost. A typical example to explain this difficulty is introduced in [72]. Let us consider a turbulent flow containing large eddies of size l_t. Since the flow shape is dependent on this integral scale, the computational domain size must be at least the same size as l_t. In order to solve the smallest eddies in the domain, the mesh size should be of the same order as the Kolmogorov length η_k, which is related to the integral scale by Equation (1.2.4). Then, the three dimensional grid points in the domain can be l_t^3/η_k. The number of time iterations can be $t_{phys}/\Delta t$ where t_{phys} is the physical simulation time and Δt is the typical time step which is of the same order as $\Delta x/u$. Therefore, the computational time t_{comp} is calculated as:

$$t_{comp} \propto \frac{l_t^3}{\eta_k} \frac{t_{phys}}{\Delta t} \propto Re^3 \tag{1.3.2}$$

Since the computational time is proportional to the Reynolds number cubed, for a high Reynolds number flow this will increase easily to the order of several decades. Accordingly, it is widely accepted that DNS approach is unrealistic except for low Reynolds number flows. For the same reason DNS results are still only available for very simple domains and hence, little DNS research on injector flows has been carried out, e.g.,[10].

Regarding combustion flows, the situation can be worse. As described in the previous section, the time scale of the chemical reaction is usually shorter than that of the turbulent motion, which leads to a shorter time step. Furthermore, the number of chemical species involved in the global reactions and the number of chemical reaction steps requires more computational resources. These capabilities and limitations of DNS on combustion flow simulation was summarised in [96]. Recently, DNS of simple flow with a Reynolds number of 11,000 was performed in [12] and the detailed results confirmed the importance of autoignition initiated by radical for flame stabilisation. However, the task required a huge amount of computational resource; 10 days with a 50 tera FLOPS supercomputer consisting of about 10,000 processors .

In practical engineering problems, the Reynolds number can easily exceed the order of 10^6, which is beyond the acceptable simulation cost for DNS. Fortunately for these complex systems the main interests lie in the properties of mean flow and its variance. Within the computational approach two concepts of 'mean' flows can be considered: temporally averaged flows obtained by long time sampling period and spatially filtering flows obtained by masking small structures of the flow. These concepts require mathematical models for some or all scales of the flow structure. These have been developed in RANS and LES techniques.

1.3.2 Reynolds Averaged Navier-Stokes Simulation

RANS is based on the temporal averaging of the governing equations. Although it gives a relatively poor prediction of the turbulence compared to DNS, this approach has been adopted in most commercial CFD solvers and applied to many engineering problems including injector flows, e.g., [17]. This is because it is computationally inexpensive and provides results that agree well with experimental work (particularly for the stationary flow), even in complex and high Reynolds number flows.

In this approach an operation is applied in which the continuous variables ψ of the real flow is decomposed into a fluctuating turbulent component ψ' and a density weighted Favre average $\tilde{\psi}$:

$$\tilde{\psi} = \frac{\overline{\rho\psi}}{\overline{\psi}} \tag{1.3.3}$$

where $\overline{(.)}$ designates a Reynolds average. With this decomposition, the instantaneous momentum equation (1.3.1) can be rewritten with averaged values and an additional Reynolds stress term, which represents correlation between averaged and fluctuating components of the flow:

$$\frac{\partial\overline{\rho}\tilde{\mathbf{u}}}{\partial t} + \nabla\cdot(\overline{\rho}\tilde{\mathbf{u}}\tilde{\mathbf{u}}) + \nabla\overline{p} = \nabla\cdot(\overline{\tau} - \overline{\rho}(\widetilde{\mathbf{u}'\mathbf{u}'})) \tag{1.3.4}$$

The averaged flow is resolved and can be regarded free from fluctuations while turbulent flow characteristics can be expressed in the Reynolds stress term. This term controls turbulent effects in all scales, from the smallest Kolmogorov scales to integral flow scale, and needs to be modelled because this term cannot be calculated from averaged values. Accordingly in RANS, simulation of governing equations require turbulence models for all scales. This resolves time-averaged steady flow and only provides time averaged turbulent information.

Modelling of the Reynolds term is the main issue in the RANS simulation and hence, many models have been developed. In order to match the models to the references, which themselves are typically based on experiments or DNS data, turbulence models can contain many coefficients to be determined. Furthermore, in many cases, these coefficients are problem dependent since flow scales and turbulent motion, particularly introduced in large scale eddies, are different among flow geometry, fluid properties and boundary conditions of the problems. It implies the limitation of the concept of RANS, namely to represent turbulence of all scales in any type of flow with a single artificial model.

Due to these features, it is generally accepted that turbulent characteristics are not predicted accurately in RANS and an alternative technique is required for more accurate and time dependent simulations of turbulent flows.

1.3.3 Large Eddy Simulation

LES is based on the concept of spatial filtering for the governing equations. The filtering concept is lead by an observation that the small structures contain only small amount of energy as shown in Figure 1.4. The properties of small turbulence can then be treated as universal for all locations and all types of flows. Similar to DNS, a direct computation is performed for the large scale flow motion with calculations based on models for small scale motion. Turbulent modelling is still necessary but only for the small scales, therefore, in terms of accuracy and computational cost, LES can be considered as an intermediate approach between DNS and RANS.

Flow variable ψ is decomposed into large scales $\tilde{\psi}$ (the same notation used in RANS but different meaning in LES) and small scales ψ''. With this decomposition, the flow is separated into scales larger than the filter (grid scale) and smaller than the filter (subgrid scale). The grid scale is solved directly and only small subgrid scales are modelled. Since the motion of the small scales are not captured, the local fluctuation can be relaxed. Figure 1.6 shows the LES capturing the local motion, compared with DNS (or exact solution) and RANS approaches.

From the energy cascade point of view, which was explained in the previous section, the subgrid scale modelling of LES can be described as follows: The energy contained in large eddies whose wavenumbers are in the integral scale and inertial sub ranges can be solved directly, in other words, without modelling (see Figure 1.4). On the other hand, the small scale eddies corresponding to large wavenumbers, being in the dissipa-

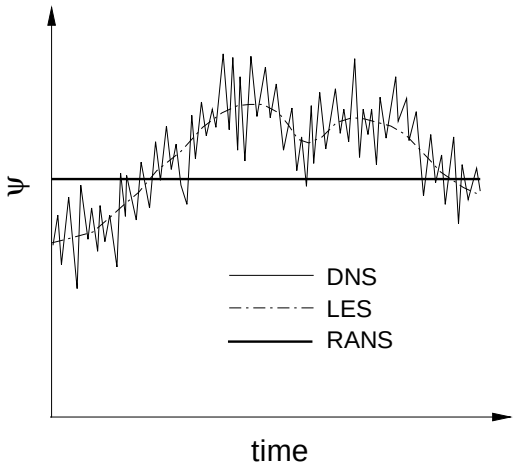

Figure 1.6: Comparison of three different numerical approach

tion range need to be modelled. This can be considered as an intermediate approach, because DNS solves all wavenumbers from the integral scales range to dissipation range without the use of models, whereas RANS solves all wavenumbers with models.

The filtered form of the Navier-Stokes momentum equation (1.3.1) is normally expressed as:

$$\frac{\partial \overline{\rho}\tilde{\mathbf{u}}}{\partial t} + \nabla \cdot (\overline{\rho}\tilde{\mathbf{u}}\tilde{\mathbf{u}}) + \nabla \overline{p} = \nabla \cdot (\overline{\tau} - \overline{\rho}(\widetilde{\mathbf{u}''\mathbf{u}''})) \tag{1.3.5}$$

The subgrid stress tensor is equivalent to the Reynolds stress tensor in RANS and modelling is necessary to close the system. This term represents the difference between the filtered non-linear term in the governing equation and the non-linear term in the filtered equations.

The Smagorinsky model is an eddy viscosity representation that is the most widely applied subgrid scale model. It is based on the same idea of the Boussinesq approximation in RANS. Conservative equations, e.g., mass, momentum and energy equations, are written in a matrix form:

$$\frac{\partial \mathbf{U}}{\partial t} + \nabla \cdot \mathbf{E} = -\nabla \cdot \tau \tag{1.3.6}$$

where **U** and **E** represent a variable array and an inviscid flux vector, respectively. The subgrid stress term **T** which corresponds to the second term in the right hand side of equation (1.3.5) can be written as:

$$\mathbf{T} = -C\Delta^2 \left|\frac{\partial \mathbf{U}}{\partial x}\right| \frac{\partial \mathbf{U}}{\partial x} \tag{1.3.7}$$

where C is generally estimated $0.1 - 0.2$ in this equation, Δ is the cell width. Although the model is considered as a typical subgrid model, it is well known that the model is too dissipative. Also, the model is sensitive to the coefficients and needs to be calibrated for each problem.

The Smagorinsky model was significantly improved in [28] where the model coefficients can be determined dynamically; tuning of the Smagorinsky model is therefore not necessary. This model is also widely used and the subgrid stress can be represented as follows:

$$\mathbf{T} = -C\Delta^4 \left|\frac{\partial \mathbf{U}}{\partial x}\right| \frac{\partial^3 \mathbf{U}}{\partial x^3} \tag{1.3.8}$$

An alternative model, which is the so-called similarity model was introduced in [7]. This is based on the assumption that the smallest resolved scales is similar to the largest unresolved scales and the subgrid scale stress can be expressed as follows:

$$\mathbf{T} = -C\Delta^2 \left(\frac{\partial \mathbf{U}}{\partial x}\right)^2 \tag{1.3.9}$$

This model is known to be insufficiently dissipative, and often used with a more dissipative model, e.g., Smagorinsky type model.

These models can describe the subgrid scale term in equation (1.3.5), however, the formulation implicitly contains a commutation assumption:

$$\widetilde{\frac{\partial \psi}{\partial x}} = \frac{\partial \tilde{\psi}}{\partial x} \tag{1.3.10}$$

where ψ represents any variable. The assumption holds true only when the grid spacing is equal, but in many problems of complex geometry flow this is not the case. Another potential error can arise when the equation applied to the computation has a truncation error. The main source of this truncation error is the unavoidable process of discretisation and rounding of the continuous values. When all these possible errors are accounted and written explicitly, the LES momentum equation (1.3.5) can be rewritten as follows:

$$\frac{\partial \overline{\rho}\tilde{\mathbf{u}}}{\partial t} + \nabla \cdot (\overline{\rho}\tilde{\mathbf{u}}\tilde{\mathbf{u}}) + \nabla \overline{p} = -\nabla \cdot \overline{\tau} - \nabla \cdot \mathbf{T} - \nabla \cdot \tau_{\mathbf{tr}} - \mathbf{m} \tag{1.3.11}$$

where τ_{tr} is the truncation error term and $\mathbf{m}$ is the commutation error term. Therefore, equation (1.3.5) holds under the assumption that:

$$\nabla \cdot \mathbf{T} \gg \nabla \cdot \tau_{\mathbf{tr}} + \mathbf{m} \tag{1.3.12}$$

and the right hand side can be neglected. However, it is not usually shown that the affect of commutation error is truly negligible. On the contrary, it is shown e.g., in [29], that the truncation error is significant and can be of the same order as the subgrid scale term in case the order of the scheme is not high, which violates the above inequality.

The flow profiles obtained via LES are reasonably accurate and so it has proven to be more suitable than RANS in the research on turbulent jet flows. However, conventional LES requires an explicit filtering of the flow, which means subgrid scale modelling for the particular flow is crucial. This is not an easy task since (as mentioned earlier) the error terms inherent to discretisation of the governing equations affect the dissipation mechanism of turbulence.

1.4 Objectives of the Research

The aim of this research is to investigate computational modelling for accurate simulation of turbulent mixing and combustion flows. To achieve the aim of the research, the subject is broken down into three objectives.

- Simulation of turbulent mixing non reactive jet flows. In this simulation, an advanced numerical computational method based on LES in conjunction with high-resolution and high order modelling, namely ILES, is applied for the first time to the complex engineering injector flow.
- Parametric survey of the turbulent non reactive jet flows. In this simulation, effects of some important parameters to the flow field, e.g., swirl intensity, inflow conditions, grid resolution, density ratio and other physical properties of the flow are investigated.
- Simulation of turbulent combustion flows. In this simulation, chemical reactions are combined with turbulent flow computation in the ILES technique.

1.5 Structure of the Thesis

Chapter 2 : The ILES with high-order high-resolution methods are introduced. It states the differences between high-resolution and non high-resolution methods, followed by the description of key process of the methods; namely reconstruction and Riemann solver. The built-in subgrid scale model of the ILES is discussed and compared with models used in conventional LES. Time stepping method used in the research and solution process of the computational code are briefly described.

Chapter 3 : Simulation of the non reactive jet flow is presented. It commences with introduction of the past research and reference experimental investigations. Next, governing equations and numerical methods are detailed. It shows results of instantaneous and mean flow velocity field and species field. Effects of some parameters such as boundary conditions, grid resolution and order of accuracy are presented with analyses of kinetic energy spectrum. Effects of Atwood number which is a density ratio of fuel and air is investigated extensively. Some other effects of fluid properties on the flow field are shown in the end.

Chapter 4 : Simulation of the combustion flow is described. After introducing experimental references, methodology is detailed in order of setting of the governing equations, selection of the chemical reaction scheme and modelling approach of the simulation. Simulation with finite rate reaction approach combined with ILES is demonstrated. Results of ILES fast chemistry approach are then shown and compared with experimental data.

Chapter 5 : Concluding remarks are presented with some key results. Recommendations for the future work are also given.

1.6 Publications

The following publications have resulted from this work:

- Y. Shimada, B. Thornber and D. Drikakis. Large eddy simulation of turbulent jet flow in gas turbine combustors. *Notes on Numerical Fluid Mechanics and Multidisciplinary Design.* 110:337-343,2010.
- Y. Shimada, B. Thornber and D. Drikakis. High-order implicit large eddy simulation of gaseous fuel injection and mixing of a bluff body burner. *Computers and Fluids.* Accepted.
- Y. Shimada, B. Thornber and D. Drikakis. Large eddy simulation of swirl flow in gas turbine combustors. In *Proceedings of the Sixth International Symposium on Turbulence, Heat and Mass Transfer.* Rome, Italy, September 2009.

The following presentation was made on the technical meeting.

- Y. Shimada, B. Thornber and D. Drikakis. Implicit large eddy simulation of turbulent jet flows in combustors. *Computational Combustion using High Performance Computing Spring School.* Cambridge, UK, April 2009.

CHAPTER 2

High-order High-resolution Implicit Large Eddy Simulation

2.1 Introduction

ILES techniques together with high-resolution methods were developed to overcome the disadvantages of the conventional LES approach described in the previous chapter [22, 18, 20, 32]. Firstly, it should be noted that high-resolution methods are not numerical simulation with fine grid size, but a defined term for certain numerical methods which are detailed in this chapter. This method was originally developed for the purpose of solving the advective terms of the governing equations accurately. However, after a close relationship of the properties of high-resolution methods to the unresolved scale turbulence modelling for LES was found [99], applications of the high-resolution methods to LES were attempted. As a consequence, some extensive research [18, 26, 55] confirmed the applicability of high-resolution methods for generation of viscosity for turbulence modelling. The idea was to control the embedded properties of the high-resolution methods and mimic them as a subgrid scale modelling for LES and was named Monotone Integrated LES (MILES). Since the unresolved scale modelling are expressed implicitly and do not appear in the governing equations, the MILES method is also called Implicit LES. An important insight into ILES is that the numerical accuracy does not only depend on the mathematical modelling but also on the numerical methods. In other words, models and numerical methods cannot be considered separately [22]. The ILES concept can be explained as, instead of setting explicit filters for the determination of the subgrid scales it is assumed in ILES, that the numerical discretisation implicitly accounts subgrid scales and hence, setting explicit filters for the determination of subgrid scale is unnecessary [18]. This ILES concept is based on the fact that the leading order of the numerical truncation error is similar in behaviour to a typical subgrid scale model. These errors are manifested as a dissipation occurring in the reconstruction process of high-resolution methods incorporated in Godunov schemes [22]. Since the early studies into ILES (stated above), research using ILES has been conducted for both basic configuration flows and complex engineering flows, and has shown promising results.

2.2 High-resolution Method

Modern high-resolution methods that solve the advective term of the governing equations accurately, are equipped with non spurious oscillations features at the same time. This can be found in the description of the high-resolution schemes in [39] and classified in [18], which satisfies the following properties:

- Provide at least second-order of accuracy in smooth areas of the flow.
- Produce numerical solutions relatively free from spurious oscillations.
- In the case of discontinuities, the number of grid points in the transition zone containing the shock wave is smaller in comparison with that of first-order monotone methods.

These descriptions clearly point out that the high-resolution method can circumvent Godunov's theorem which states 'There are no monotone, linear schemes of second or higher order of accuracy'. The theorem implies that (a) linear higher-order methods provide superior accuracy to first-order methods in smooth regions of the flow, but they produce spurious oscillations near high gradients and (b) that monotone first-order methods avoid spurious oscillations but are too inaccurate for practical simulations. Godunov applied the solution of the local Riemann problem for the discretised formulation of the governing equations. Although his classical method is limited by his theorem and only first-order accurate, its physical foundation is attractive. The key to circumvent the theorem was found in the assumption of linear schemes [18]. Therefore, in order to design a scheme providing higher than first order of accuracy and free from spurious oscillations, a non-linear method is required. With a non-linear differencing technique, the high-resolution methods can provide 'physically meaningful' results in all flow regions, even in the vicinity of high gradients, while a non high-resolution method can lead to an ill-behaved solution in a high gradients region.

The typical procedure of the high-resolution methods is depicted in Figure 2.1. First, according to a basic concept of a finite volume method, the continuous variables (Figure 2.1 (top)) are represented by a piecewise volumetric average values (Figure 2.1 (second-left)). These values are considered to be constant everywhere in the volume ('cell' in CFD). In the first-order Godunov method, the simulation proceeds to the Riemann solver shown in Figure 2.1 (third-left). In the high-resolution methods however, a high order reconstruction step in Figure 2.1 (second-right) follows. An interpolation, sometimes called limiting, is manipulated in this step to reconstruct the cell interface values, which concerns the unresolved distribution of the original continuous values and hence, increases the order of spatial accuracy. Normally, the reconstructed values are not identical at the left hand and right hand side of the cell interface. In the Godunov method (for both first-order and higher order methods) this discontinuity is solved locally by the Riemann solver (Figure 2.1 (third)). Once the cell interface values are determined, the fluxes can be calculated and a time stepping method integrates

these fluxes to produce the next time solution, which are given as cell averaged values (Figure (2.1 (bottom)) following the finite volume concept.

In the Godunov type methods the order of the method depends on the order of the spatial reconstruction. However, since the high-order interpolation is based on the assumption of a smooth flow, the order of the spatial accuracy can be reduced to a first-order piecewise constant reconstruction in areas where discontinuities can be seen. Then, using a higher-order reconstruction can result in decreasing the order of accuracy in the vicinity of high gradients regions, particularly shock waves. Therefore, the accurate simulation of the high-resolution methods depends on their two intrinsic processes: the reconstruction and the Riemann solver. These are explained in the following sections.

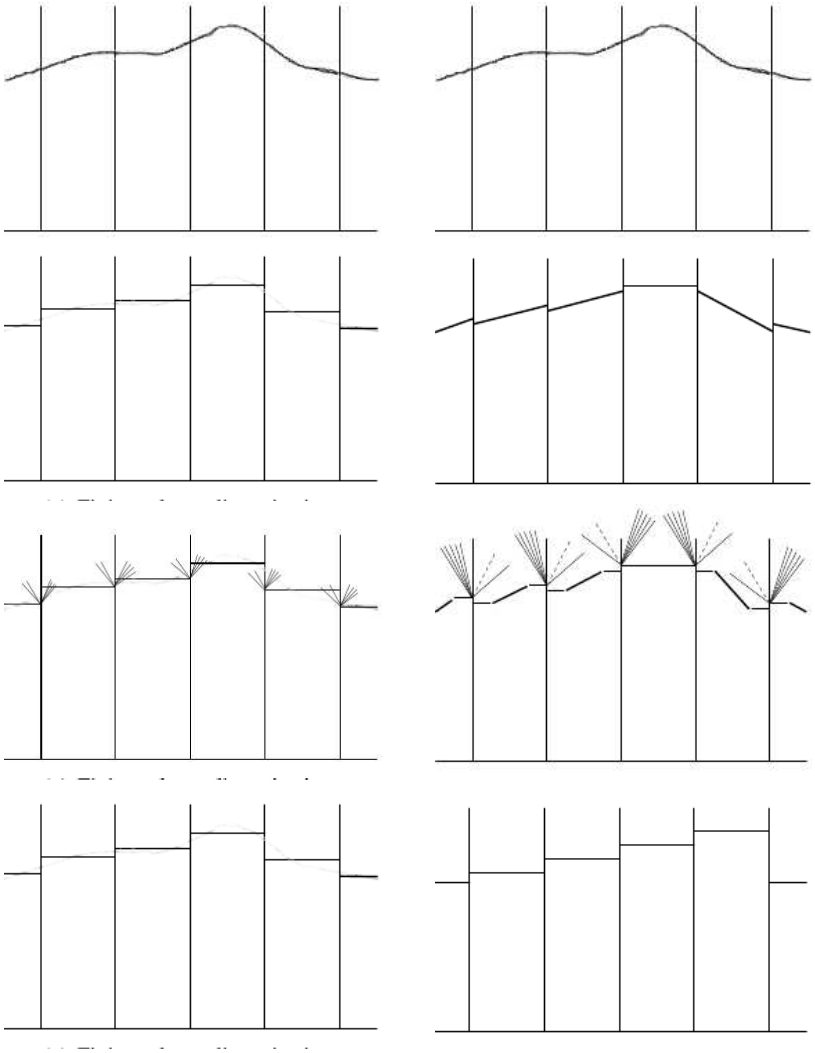

Figure 2.1: Solution process of the original Godunov method (left) and the High-resolution method (right). Solution proceeds from top to bottom: Initial data (top), Averaging and Reconstruction (second), Riemann Solution (third) and Reaveraging (bottom) ,after [22]

2.3 Reconstruction Process

In this thesis, second, fifth and ninth-order spatial accurate methods were tested. For second and fifth-order accuracy, the Monotonic Upstream-centred Scheme for Conservation Laws (MUSCL) scheme originally developed in [94] was applied.

The left and right variables **U** at the cell interfaces for the MUSCL scheme were extrapolated as:

$$\mathbf{U}_{i+1/2,L} = \mathbf{U}_i + \frac{1}{4}\left((1-C)\phi(r_L)(\mathbf{U}_i - \mathbf{U}_{i-1}) + (1+C)\phi\left(\frac{1}{r_L}\right)(\mathbf{U}_{i+1} - \mathbf{U}_i)\right) \tag{2.3.1}$$

$$\mathbf{U}_{i+1/2,R} = \mathbf{U}_{i+1} + \frac{1}{4}\left((1-C)\phi(r_R)(\mathbf{U}_{i+2} - \mathbf{U}_{i+1}) + (1+C)\phi\left(\frac{1}{r_R}\right)(\mathbf{U}_{i+1} - \mathbf{U}_i)\right) \tag{2.3.2}$$

where $i + 1/2$ expresses cell interfaces between cells i and $i + 1$, $-1 \leq C \leq 1$ is a free parameter and ϕ is a limiter function based on the slopes r of the conserved variables within the four point stencil for the second-order accurate scheme. A popular second-order limiter function was proposed by Van Leer [95]:

$$\phi^{2nd} = \begin{cases} 0 & (r \leq 0) \\ 2r/(1+r) & (r > 0) \end{cases} \tag{2.3.3}$$

with the left and right hand ratio of the slopes:

$$r_L = \frac{\mathbf{U}_{i+1} - \mathbf{U}_i}{\mathbf{U}_i - \mathbf{U}_{i-1}} \tag{2.3.4}$$

$$r_R = \frac{\mathbf{U}_{i+1} - \mathbf{U}_i}{\mathbf{U}_{i+2} - \mathbf{U}_{i+1}} \tag{2.3.5}$$

A fifth-order accurate MUSCL scheme consisting of six stencils was proposed in [50]:

$$\phi_L^{5th} = \frac{2/r_{i-1,L} + 11 + 24r_{i,L} - 30r_{i,L}r_{i+1,L}}{30} \tag{2.3.6}$$

$$\phi_R^{5th} = \frac{-2/r_{i+2,R} + 11 + 24r_{i+1,R} - 30r_{i+1,R}r_{i,R}}{30} \tag{2.3.7}$$

where the ratio of the slopes are:

$$r_L = \frac{\mathbf{U}_{i+1} - \mathbf{U}_i}{\mathbf{U}_i - \mathbf{U}_{i-1}} \tag{2.3.8}$$

$$r_R = \frac{\mathbf{U}_i - \mathbf{U}_{i-1}}{\mathbf{U}_{i+1} - \mathbf{U}_i} \tag{2.3.9}$$

For the ninth-order spatial accurate scheme the Weighted Essentially Non-Oscillatory (WENO) methods based on [6, 42, 53] was adopted. The principal approximation method of WENO is to average high-order stencils by a weighted combination by way of a local smoothness to produce a higher order stencil. This averaging reduces the sensitivity to small changes in the sample stencils and it also reduces the effects of the truncation errors. Thus, WENO schemes obtain $2q-1$ order of accuracy with q being the number of sample stencils. For ninth-order WENO method $q = 5$ and hence, five stencils across the interface are used. In accordance with [6], the cell interface value can be expressed as:

$$\mathbf{U}_{j+1/2} = \sum_{i=1}^{q} \left(C_{II,_i} \sum_{k=1}^{q} (C_{I,ik} \mathbf{U}_{j+k-q}) \right) \tag{2.3.10}$$

with

$$C_{II,i} = \frac{\dfrac{1}{(\delta + C_{III,i})^2}}{\displaystyle\sum_{i=1}^{q} \frac{1}{(\delta + C_{III,i})^2}} \tag{2.3.11}$$

where coefficients $C_{I,ik}$, $C_{II,ik}$ and $C_{III,i}$ can be found in [6], and δ is a small number, e.g., 10^{-6}.

2.4 Riemann Solvers

The cell interface values are reconstructed with the high-order limiters. However, the left hand and right hand side of the reconstructed data have discontinuities. In order to solve these discontinuities whilst retaining the fundamental physical and mathematical characteristics of the governing equations, the high-resolution methods incorporate the local Riemann solver. In the Riemann solver a system of hyperbolic conservation laws with discontinuous initial boundary condition is concerned:

$$\begin{aligned} &\frac{\partial \mathbf{U}}{\partial t} + \mathbf{E}(\mathbf{U}(x)) = 0 \\ &\mathbf{U}(x,0) = \mathbf{U}^{(0)}(x) \\ &\mathbf{U}(0,t) = \mathbf{U}_L(t), \;\; \mathbf{U}(L,t) = \mathbf{U}_R(t) \end{aligned} \tag{2.4.1}$$

The solution is physically characterised by a wave system consisting of a rarefaction waves, a contact discontinuity and a shock wave.

For the Riemann problems analytical solutions are available. Hence, for some simple governing equation systems or some simple low computational cost problems exact Riemann solvers can be adopted. However, noting that a large proportion of the computational time is spent on solving the Riemann problems and that approximate Riemann solvers can produce nearly identical results compared to the exact solution [93]. Therefore, an approximate Riemann solver is preferred for complex governing equations or high computational cost problems. Practically, almost all computational codes adopt approximate Riemann solvers.

The HLLC (Harten, Lax and van Leer plus Contact wave) Riemann solver [93], which was developed as a modification of the original HLL Riemann solver, has been widely used and adopted in this thesis.

Figure 2.2 illustrates a typical wave pattern for the Euler equations concerned in the HLLC Riemann solver. The solution can consist of four constant conditions, separated by the three basic waves stated above. The left and the right wave can either be a rarefaction wave or a shock wave but it is assumed here that the rarefaction wave is on the left hand side and shock wave is on the right hand side. The middle wave is a contact discontinuity. In the left and right end regions where the velocities are u_L and u_R, respectively, conditions can be simply defined by the initial conditions at $t = 0$. The two mid conditions between rarefaction and shock waves remain to be calculated. In Figure 2.2 a left-running rarefaction wave is moving at a speed which is given by the difference of the local velocity and the local speed of sound, $u - a$. This rarefaction decreases the pressure and the density of the gas. The boundary on the high pressure side (right in this figure) is called the head, and boundary on the low-pressure side (left in this figure) is called the tail. Inside the head and tail, the velocity and other conditions follow a smooth, non-linear transition from u_L to u_L^*. On the other side, a right-running shock wave can be observed moving at a speed of $u + a$. The shock wave is a non-linear wave that increases the pressure, density, temperature and entropy as it passes through the fluid in condition u_R. The state u_R^* can be determined from state u_R through the Rankine-Hugoniot relations. The region between the expansion and the shock is often referred to as the star region. In the star region, two state u_L^* and u_R^* are connected through a contact discontinuity travelling with the wave speed u. The characteristics in this area run parallel to each other and neither expansion nor compression can occur. Hence, both the velocity u^* and the pressure p^* are constant in the star region, but other flow properties show discontinuities.

The above description of HLLC approximate Riemann solver can be written:

$$\tilde{\mathbf{U}} = \begin{cases} \mathbf{U}_L & (x/t \leq u - a) \\ \mathbf{U}_L^* & (u - a < x/t < u) \\ \mathbf{U}_R^* & (u < x/t < u + a) \\ \mathbf{U}_R & (x/t \geq u + a) \end{cases} \tag{2.4.2}$$

The HLLC flux can be expressed:

$$\mathbf{E}_{i+1/2}^{HLLC} = \begin{cases} \mathbf{E}_L & (0 \le u - a) \\ \mathbf{E}_L + (u-a)(\mathbf{U}_L^* - \mathbf{U}_L) & (u - a < 0 < u) \\ \mathbf{E}_R + (u+a)(\mathbf{U}_R^* - \mathbf{U}_R) & (u < 0 < u + a) \\ \mathbf{E}_R & (0 \ge u + a) \end{cases} \tag{2.4.3}$$

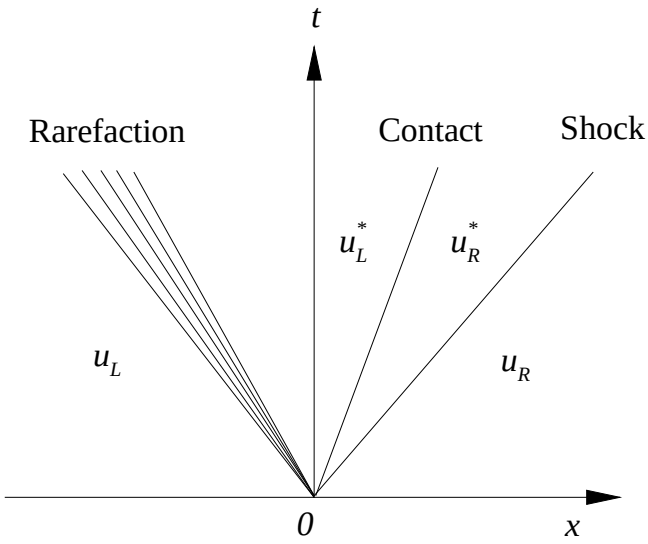

Figure 2.2: Schematic of a typical wave system of a Riemann problem

2.5 Implicit Subgrid Scales Modelling

The high-resolution methods can be employed for solving the advective terms in the governing equations of ILES for turbulent flows. This combination is based on a modified equations analysis (MEA) that shows that the embedded properties of finite volume, high-resolution methods demonstrate mathematically and physically similar behaviour to traditional subgrid scale models typically used in conventional LES. They can provide a local non-linear numerical viscosity acting as a dynamic stabiliser for the solution, which is equivalent to a purely dissipative turbulent viscosity model. They also provide a backscatter mechanism related to scale-similarity models in classical LES. The formulation of ILES can be compared to the one in LES. When no filtering is applied to the Navier-Stokes momentum equation (1.3.1), the explicit subgrid scale term and the commutation error term do not appear, yielding:

$$\frac{\partial \overline{\mathbf{u}}}{\partial t} + \nabla \cdot (\overline{\mathbf{u}\mathbf{u}}) + \frac{1}{\overline{\rho}} \nabla \overline{p} = -\nabla \cdot \overline{\tau} - \nabla \cdot \tau_{\mathbf{tr}} \tag{2.5.1}$$

where $\tau_{\mathbf{tr}}$ is the truncation term dependant on the discretisation scheme and the solution procedure, i.e., high-resolution methods: The over bars denote an average originating from the finite volume scheme. Therefore, the cell averaging operation of the finite volume can be regarded as an implicit spatial filtering. The leading order of the remaining truncation error term has been analytically examined by way of MEA [22, 26, 55]. According to this analysis, a comparison of the subgrid scale terms of ILES to the explicit subgrid scale terms, used in conventional LES, is briefly described here.

A discrete, one dimensional equation is considered:

$$\mathbf{U}_i^{n+1} = \mathbf{U}_i^n - \frac{\Delta t}{\Delta x}(\mathbf{E}_{i+1/2} - \mathbf{E}_{i-1/2}) \tag{2.5.2}$$

where superscript n and subscript i designate time step and spatial position respectively. The reconstruction step of the high-resolution method calculates the left and right hand side values of the cell interface and the Godunov fluxes are resolved by a linearised Riemann solver [22]:

$$\mathbf{E}_{i+1/2} = \frac{1}{2}(\mathbf{E}_{i+1/2,R} - \mathbf{E}_{i+1/2,L}) - \frac{|\mathbf{E}'|}{2}(\mathbf{U}_{i+1/2,R} - \mathbf{U}_{i+1/2,L}) \tag{2.5.3}$$

where $\mathbf{E}'$ is the derivative of the flux with respect to $\mathbf{U}$, $\partial\mathbf{E}/\partial\mathbf{U}$.

For this general form of the modified equation an effective subgrid stress, namely a truncation error can be:

$$\tau_{\mathbf{tr}} = -C_1 \Delta^2 \mathbf{E}' \frac{\partial^2 \mathbf{U}}{\partial x^2} - C_2 \Delta^2 \mathbf{E}'' \left(\frac{\partial \mathbf{U}}{\partial x} \right)^2 \tag{2.5.4}$$

where C_1 and C_2 are constants depending on the details of the numerical method and Δ is the cell width. It can be observed that the second term is essentially the same form to the leading order term for the self-similar model in equation (1.3.9).

When the MPDATA scheme [84] is used with a limiter:

$$\mathbf{S}_{i+1/2} = \left(1 - \left| \frac{\mathbf{U}_{i+1} - \mathbf{U}_i}{\mathbf{U}_i - \mathbf{U}_{i+1}} \right| \right) (\mathbf{U}_{i+1} - \mathbf{U}_i) \tag{2.5.5}$$

and the cell interface values are expressed as:

$$\mathbf{U}_{i+1/2,L} = \mathbf{U}_i + \mathbf{S}_{i+1/2} \tag{2.5.6}$$

$$\mathbf{U}_{i+1/2,R} = \mathbf{U}_{i+1} - \mathbf{S}_{i+1/2} \tag{2.5.7}$$

the leading order truncation error results in:

$$\tau_{\mathbf{tr}} = -C\Delta^2|\mathbf{E}'|\left|\frac{\partial \mathbf{U}}{\partial x}\right|\frac{\partial \mathbf{U}}{\partial x} \tag{2.5.8}$$

which is essentially the same form as the Smagorinsky model in equation (1.3.7).

Thus, an analysis of the MEA for ILES implies a similarity to the explicit subgrid scale models applied in the conventional LES: Hence, the truncation term can be considered as a built-in mechanism representing the effect of unresolved scales.

2.6 Time Step Integration

Since the flow fields are inherently unsteady for the Euler equation and the flow components fluctuate rapidly, an explicit Runge-Kutta time integration method was chosen for the time stepping method.

A single stage scheme is the same as the Euler method and is the simplest procedure:

$$\mathbf{U}_j^{n+1} = \mathbf{U}_j^n + \frac{\Delta t}{\Delta x}\mathbf{E}(\mathbf{U}_j^n) \tag{2.6.1}$$

However, this method is first-order accurate in time and therefore, higher order methods with linear combinations of multi-stages are preferred. Then, a normal second-order procedure is expressed as:

$$\mathbf{U}_j^1 = \mathbf{U}_j^n + \frac{1}{2}\frac{\Delta t}{\Delta x}\mathbf{E}(\mathbf{U}_j^n) \tag{2.6.2}$$

$$\mathbf{U}_j^{n+1} = \mathbf{U}_j^n + \frac{\Delta t}{\Delta x}\mathbf{E}(\mathbf{U}_j^1) \tag{2.6.3}$$

And, a third-order Total Variation diminishing (TVD) method can be derived as:

$$\mathbf{U}_j^1 = \mathbf{U}_j^n + \frac{\Delta t}{\Delta x}\mathbf{E}(\mathbf{U}_j^n) \tag{2.6.4}$$

$$\mathbf{U}_j^2 = \mathbf{U}_j^n + \frac{1}{4}\frac{\Delta t}{\Delta x}\left(\mathbf{E}(\mathbf{U}_j^n) + \mathbf{E}(\mathbf{U}_j^1)\right) \tag{2.6.5}$$

$$\mathbf{U}_j^{n+1} = \mathbf{U}_j^n + \frac{1}{6}\frac{\Delta t}{\Delta x}\left(\mathbf{E}(\mathbf{U}_j^n) + \mathbf{E}(\mathbf{U}_j^1) + 4\mathbf{E}(\mathbf{U}_j^2)\right) \tag{2.6.6}$$

With these explicit time integration methods, the timestep size is limited as follows:

$$\Delta t = C_{FL}\frac{\Delta x}{a} \tag{2.6.7}$$

where C_{FL} stands for Courant-Friedrichs-Lewy number (CFL). In the case of a compressible equations system, the CFL number should remain lower than unity so that the computation can track the effects of the pressure wave by inhibiting the larger wave propagation speed than the computational grid spacing. However, by adding an additional stage, a third-order extended stability method was developed to allow a larger CFL number [86]:

$$\mathbf{U}_j^1 = \mathbf{U}_j^n + \frac{1}{2}\frac{\Delta t}{\Delta x}\mathbf{E}(\mathbf{U}_j^n) \tag{2.6.8}$$

$$\mathbf{U}_j^2 = \mathbf{U}_j^1 + \frac{1}{2}\frac{\Delta t}{\Delta x}\mathbf{E}(\mathbf{U}_j^1) \tag{2.6.9}$$

$$\mathbf{U}_j^3 = \frac{2}{3}\mathbf{U}_j^n + \frac{1}{3}\mathbf{U}_j^2 + \frac{1}{6}\frac{\Delta t}{\Delta x}\mathbf{E}(\mathbf{U}_j^2) \tag{2.6.10}$$

$$\mathbf{U}_j^{n+1} = \mathbf{U}_j^3 + \frac{1}{2}\frac{\Delta t}{\Delta x}\mathbf{E}(\mathbf{U}_j^3) \tag{2.6.11}$$

where the CFL number can be up to 2, which is beneficial in terms of computational costs. In this thesis, the third-order extended stability method was applied, however, a second-order method was used for simulations of a parametric survey after no significant difference confirmed in the typical test cases.

2.7 Computational Solution Process

Figure 2.3 summarises the solution process of the ILES computation adopted in this thesis. The three dimensional Navier-Stokes equations are split into each direction, e.g., x, y and z for a cartesian and ξ, η and ζ for a curvilinear coordinate system. The equations are decomposed into inviscid terms which are the same as the Euler equations, and the viscous terms including mass, momentum and energy transport. For the linear viscous terms a second-order central difference scheme is employed while a Godunov-type high-resolution method, described in the previous sections, solves for the non-linear advective flux derivatives in the inviscid terms. High-resolution is achieved through the reconstruction step incorporating different variants of non-linear limiting schemes. After these fluxes are added together the next timestep variables are calculated with a time stepping method as explained in the previous section.

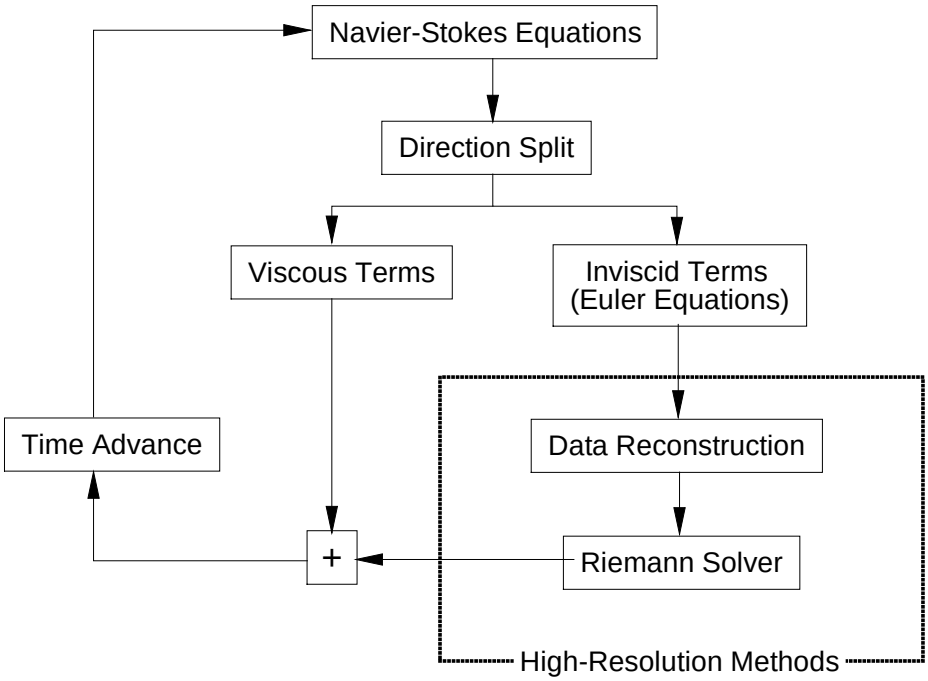

Figure 2.3: Solution process of the ILES computational code

CHAPTER 3

ILES of Non Reactive Flows

3.1 Introduction

Fuel jet injection and mixing with air has a major impact on overall combustor performance and the flow field contains many complex fluid mechanical phenomena: transition of the fuel jet from laminar to turbulent, formation of the recirculation zones, vortex breakdown and turbulent mixing, hence, numerous experiments and computations have been conducted. In the context of numerical research, with the aid of recent developments in computational power, LES has been applied to these flows. This is because LES has been recognised as a more promising approach for time dependent flows than RANS in which only temporally averaged values are available.

In this decade, extensive research has been carried out on several configurations of reactive and non-reactive fuel jet flows in the framework of the International Workshop on Measurement and Computation of Turbulent Nonpremixed Flames (TNF) which is summarised in [8]. In this research, three dimensional computations used conventional LES approaches which solve the filtered governing equations together with subgrid scale models, e.g., a Smagorinsky type model. The results showed a reasonable agreement with experimental data but at the same time showed some limitations. As described in [8], the simulation is sensitive to the subgrid scale model coefficient which effects both velocity and scalar fields. Moreover, the constant turbulent Schmidt number which often used in the conventional LES [47, 65] is involved in the subgrid scale model and this may cause the deviation in the scalar field. Therefore, these coefficients require calibration which can be a difficult task. A well known solution is to apply the dynamic procedure [28], which can avoid an explicit setting of the model coefficient, however, this results in strong dependence of the turbulent viscosity on grid resolution thus, the conventional LES requires sufficiently large grid size. In a conventional LES, the filtered equations are derived assuming the commutation between differentiated and filtered variables, but this assumption is valid only with equal filter length, which is not likely in complex geometries. A number of other issues are reported in past reviews (see, for example, [73]). These problems are basically unavoidable as long as filtering is explicitly operated to the governing equations.

ILES techniques (see reviews [36, 56, 18]) together with high-resolution methods [22,

93] have been developed to overcome the principal disadvantages of the conventional LES approach described above. In ILES computation it is assumed that the numerical discretisation itself accounts for unresolved scales, in other words implicitly modelling the subgrid scales, and hence setting explicit filters for determination of subgrid scale is unnecessary. Furthermore, the use of appropriate limiters in the reconstruction process of high-resolution methods, which are employed in ILES, accomplishes non-linear dissipation to be selectively added to the computational cells.

There are a number of recent and past studies, which have demonstrated the accuracy of ILES in simulations of both basic and complex flows, e.g., [36, 56, 21, 27, 33, 38, 37, 92, 100, 26, 19, 31, 57, 90], as well as studies dealing with theoretical aspects of ILES and associated numerical methods [31, 56, 55, 91].

ILES methods have also been validated in the past with respect to gas turbine combustor flows [27, 33]. In [33] two LES models, a second-order ILES model with 1 and 2 step Arrhenius chemistry, and a fractal flame-wrinkling LES model coupled to a conventional one-equation eddy-viscosity subgrid model, were used. The authors showed reasonable agreement when comparing their predictions with experimental data and with other LES computations of the same case.

The aim of this chapter is to assess the accuracy of higher-order ILES methods for non reactive, multi-species fuel jet flows. The physics of the turbulent mixing jet flows is also investigated by focusing on the effects of swirl and density difference between fuel and air.

3.2 Experimental Research of Fuel Mixing Jets

Experimental research of fuel mixing jets has been extensively performed as the flow structures are strongly dependent on the fuel burner geometry. Until recently time dependent turbulent flow was computationally too costly.

In this decade, several research projects on selected flows and flames have been conducted and detailed flow structures identified. For example, three mixing layers are located in the gaps of four main streams namely, the fuel jet flow, the inner vortex above bluff body, the outer vortex above the bluff body plate and the air flow [15, 16]. The flow observations also revealed that a second recirculation zone emerged on the centreline of the flames further downstream of the primary recirculation zone and that the region between these recirculation zones was characterised by high shear stresses [44, 62]. Other simple and generic shape burner flows were also examined by some groups [1, 64, 66, 67]. However, 3D turbulent fuel and air inflow boundary conditions are not yet available due to measurement difficulty though they are the key properties of the flow development.

The geometry of the fuel jet burner used in this study is shown in Figure 3.1, and was investigated experimentally [15, 59]. This burner geometry was designed and tested at Sydney University. Both non reactive and reactive flows were measured with this

burner. Compressed natural gas (methane is the primary species) and air were used in the experiments. Due to its simple and generic geometry but complex flow structure, this burner is suitable for validation of the ILES methodology. At the fuel injection plane the burner consists of a fuel jet nozzle, a bluff body plate and an annulus oxidiser flow inlet. Fuel is injected in the axial direction through the round exit nozzle (diameter 3.6*mm*) located in the centre of a cylindrical bluff body (diameter 50.0*mm*). The oxidiser is supplied in the axial direction, with or without a circumferential velocity component, from the annulus inlet (width 5.0*mm*) surrounding the bluff body plate. The burner is located in the centre of a wind tunnel which supplies constant air flow as coflow surrounding the injector. The flow field is entirely controlled by the three inflows, namely the fuel inlet velocity, the oxidiser inlet velocity and the coflow velocity.

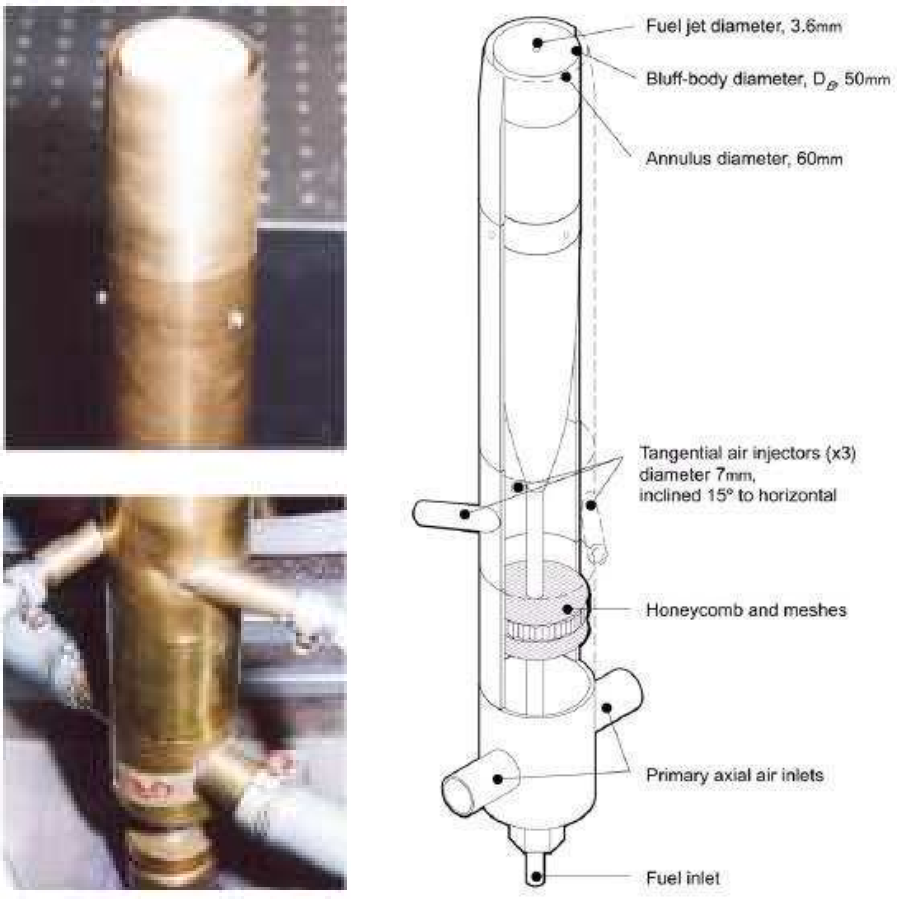

Figure 3.1: Photo of the 'Sydney bluff body burner' (left) [45] and its schematic (right) [61]

3.3 Governing Equations for Non Reactive Flows

The three dimensional compressible mass, momentum and energy conservation laws for a gas mixture were employed.

Regarding multi-species modelling, pressure oscillations in mixed cells have been a significant problem in compressible flows. A quasi conservative model [4] was adopted here since simulations of simple flow configurations showed that the pressure oscillations were eliminated with this multi-species model compared to the mass fraction model or the total enthalpy conservation model [89]. In the quasi-conservative model the volume fraction of fuel is tracked instead of mass fraction and hence, the mixture mass conservation equation was replaced by volume fraction equations for each species and a balance equation of volume fraction.

An instantaneous pressure equilibrium assumption was applied in which both species in the mixture have the same velocity and pressure within a single volume cell. Under these conditions the governing equations are:

$$\frac{\partial \alpha_f \rho_f}{\partial t} + \nabla\cdot(\alpha_f \rho_f \mathbf{u}) = 0 \tag{3.3.1}$$

$$\frac{\partial \alpha_o \rho_o}{\partial t} + \nabla\cdot(\alpha_o \rho_o \mathbf{u}) = 0 \tag{3.3.2}$$

$$\frac{\partial \rho \mathbf{u}}{\partial t} + \nabla\cdot(\rho \mathbf{u}\mathbf{u}) = -\nabla\cdot\mathbf{P} \tag{3.3.3}$$

$$\frac{\partial \rho E}{\partial t} + \nabla\cdot(\rho E \mathbf{u}) = -\nabla\cdot(\mathbf{P}\cdot\mathbf{u}) - \nabla\cdot\mathbf{q} \tag{3.3.4}$$

$$\frac{\partial \alpha_f}{\partial t} + \nabla\alpha_f\cdot\mathbf{u} = 0 \tag{3.3.5}$$

where $\mathbf{u}$ is the velocity vector, α, ρ and E denote volume fraction, density of the gas mixture and total energy per unit volume, respectively, the subscript f and o designate species for fuel and oxidiser. Variables for mixture and each species are related by:

$$\alpha_f + \alpha_o = 1 \tag{3.3.6}$$

$$\rho = \rho_f \alpha_f + \rho_o \alpha_o \tag{3.3.7}$$

and other thermodynamical parameters are specified as in [4]:

$$Y_f = \alpha_f \frac{\rho_f}{\rho}, Y_o = \alpha_o \frac{\rho_o}{\rho} \tag{3.3.8}$$

$$\rho C_v T = \rho_f \alpha_f C_{v,f} T_f + \rho_o \alpha_o C_{v,o} T_o \tag{3.3.9}$$

where Y, p, C_v and T stand for mass fraction, pressure, specific heat for constant volume and temperature, respectively. By these relations multi-species in a single cell is treated as immiscible gas mixture and the volume fraction of each species can be tracked.

The total energy is a sum of internal energy and kinetic energy:

$$E = C_v T + \frac{1}{2}\mathbf{uu} \tag{3.3.10}$$

The stress tensor $\mathbf{P}$ contains pressure and viscous effect based on Stoke's hypothesis:

$$\mathbf{P} = p\mathbf{I} + \frac{2}{3}\mu(\nabla\cdot\mathbf{u})\mathbf{I} - \mu((\nabla\mathbf{u}) + (\nabla\mathbf{u})^T) \tag{3.3.11}$$

where $\mathbf{I}$ and μ stand for the unit tensor and the dynamic viscosity coefficient, respectively. The heat flux $\mathbf{q}$ follows Fourier's equation:

$$\mathbf{q} = -\kappa\nabla T \tag{3.3.12}$$

where κ is the thermal conductivity coefficient. The mixture specific heat ratio γ is evaluated using constant specific heat ratio for each species, and the ideal gas equation of state is used to relate pressure, temperature and specific heat ratio in order to close the system:

$$p = \rho C_v T(\gamma - 1) \tag{3.3.13}$$

Regarding transport properties, viscosity coefficients are calculated by Sutherland's law and the heat conductivity is evaluated using a constant Prandtl number 0.72. In the current simulation diffusion terms are neglected from species and energy equations since usually they are much smaller than turbulent diffusion terms which are embedded in the ILES high-resolution method. However, it should be noted that sensitivity of these transport properties can cause deviation in the multi-species flow simulation.

3.4 Numerical Modelling of Non Reactive Flows

The governing equations are solved using a finite volume Godunov-type method. In this method, the continuous function is discretised to cell averaged variables. The values at the next time step are determined by advective fluxes between surrounding cells. The fluxes at the cell interfaces are calculated by reconstructing cell interface values from cell averaged values, and the fluxes are then computed from the solution of the Riemann problem. Thus, an important characteristics of the Godunov-type method is the limiter which is used in the reconstruction process and controls the order of spatial accuracy.

To achieve a high-order of spatial accuracy, up to ninth-order accurate limiters were used in the simulations. MUSCL limiters were used for a second-order [95] and a fifth-order [50] accurate scheme and the WENO scheme was used for a ninth-order scheme [6].

In the reconstruction process, the velocity components are locally modified according to a procedure detailed in [91] to prevent overly dissipative behaviour of turbulent kinetic energy, particularly in low Mach number flow. This is because the leading order dissipation rate was found to be proportional to the speed of sound and hence, caused excessive dissipation in low Mach number flow [91]. With this modification under subsonic conditions, the leading order of the truncation errors which act as subgrid stresses in the ILES approach, for second, fifth and ninth-order limiters are given by [37, 91]:

$$\varepsilon^{2ndMUSCL} = \frac{\Delta x^2}{12} u u^{(1)} u^{(2)} + \frac{\Delta x^3}{12} C_{FL} a u^{(1)} u^{(3)} \tag{3.4.1}$$

$$\varepsilon^{5thMUSCL} = \frac{\Delta x^5}{60} u u^{(1)} u^{(5)} \tag{3.4.2}$$

$$\varepsilon^{9thWENO} = \frac{\Delta x^9}{1260} u u^{(1)} u^{(9)} \tag{3.4.3}$$

where Δx, a and u denote grid spacing, speed of sound and velocity in direction normal to the cell interface, respectively, the superscript (n) denotes the n-th derivative with respect to the cell interface normal. It should be noted that in the second-order reconstruction scheme the dissipation rate still includes the speed of sound. Further information of the modification is detailed in [92].

As an approximate Riemann solver, the HLLC method [93] was applied. The viscous term was discretised using standard central differences. For time integration, a third-order extended stability explicit Runge-Kutta method was employed.

In the ILES computation stated above, the discretisation to cell averaged values and reconstruction by a limiter are key to obtaining high-order accuracy. Therefore, grid

resolution and the order of accuracy of the limiters are the key parameters for accurate ILES computation.

3.5 Multi-Species Flow Simulation

3.5.1 Simulation Setup

The geometry of the fuel jet burner and the coordinate system are shown in Figure 3.2.

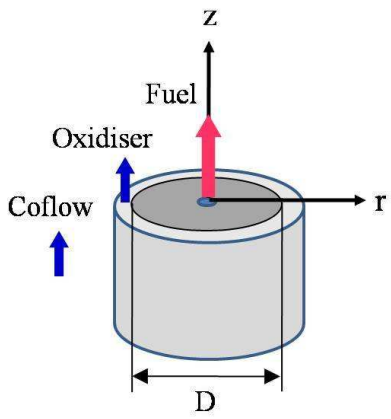

Figure 3.2: Geometry of the fuel jet burner

The computational domain is cylindrical and set downstream of the burner surface, as shown in Figure 3.3 (left). To avoid singularity at the centre axis of the domain, 8×8 square meshes for the course, medium and fine grids, and 16×16 meshes for the mediumcirc grids are distributed as shown in Figure 3.3 (right). The central square meshes has the smallest size in the domain: width and height are $7.5 \times 10^{-5} mm$ and $1.5 \times 10^{-4} mm$ respectively. The whole domain size was similar to that employed by [47, 88, 87] which has a smaller axial length. The axial and radial lengths are $5.0D$ and $8.8D$ respectively, where D is the diameter of the bluff body. To investigate effects of grid resolution and order of reconstruction the computations were carried out with four grid resolutions and three limiters.

In the study of flow structure and comparison of velocity profiles, air was selected for both fuel and oxidiser, corresponding to the experimental study [59]. For evaluation of multi-species mixing flow, methane and air were selected as fuel and oxidiser, respectively. The mean bulk inlet velocity u_{f0} are $61 m/s$ for the air jet, $85 m/s$ for the methane jet, and $20 m/s$ for the oxidiser and coflow, respectively. The Reynolds number based on the fuel inlet velocity and the fuel nozzle diameter is 1.45×10^4. The local Mach number based on the fuel inlet velocity is 0.18 for air jet case and 0.14 for methane jet case. Test cases are summarised in Table 3.1 with N_z, N_r, N_c and N_t being the axial, radial, circumferential (azimuthal) and total cell numbers, respectively. Note that 60

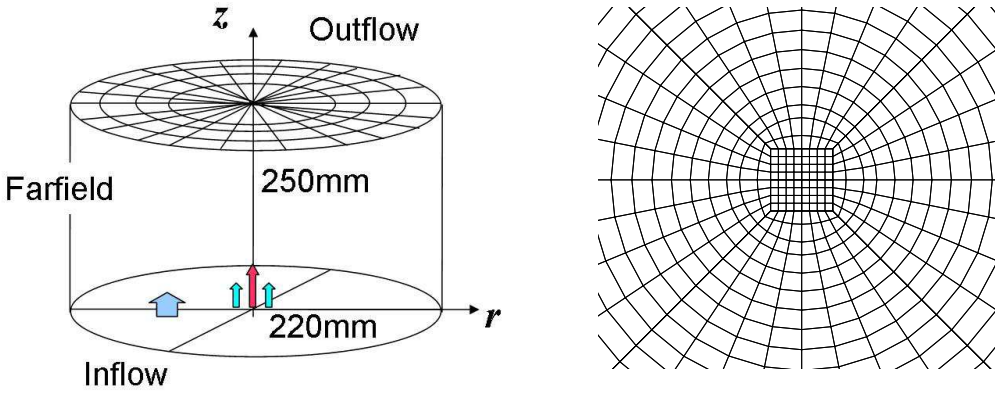

Figure 3.3: Schematic of the computational domain set in the downstream of the burner (left), grid distribution near the centre axis, showing a constant *z* plane (right)

meshes are distributed in the radial direction excluding the central square meshes for the coarse, medium and mediumcirc grid, and 120 meshes for the fine grid.

Table 3.1: Test cases for the non reactive flow simulation

Grid	N_z	N_r	N_c	N_t	limiter	Jet
Coarse	60	62	32	0.12×10^6	5th MUSCL	Air
Medium	300	62	32	0.60×10^6	2nd MUSCL	Air
Medium	300	62	32	0.60×10^6	5th MUSCL	Air
Medium	300	62	32	0.60×10^6	5th MUSCL	Methane
Medium	300	62	32	0.60×10^6	9th WENO	Air
MediumCirc	300	64	64	1.23×10^6	5th MUSCL	Air
Fine	600	124	32	2.38×10^6	5th MUSCL	Air

Random velocity fluctuations were added to the fuel and the oxidiser inflows to match the turbulent intensity to a DNS result [49], but the turbulent intensity profile was simplified as linear from the wall of the nozzle and inlet though the reference paper showed nonlinear profiles. In the reference paper, the Reynolds number based on the mean velocity and half-width of the flow passage is 3300 while in the current simulation test case $Re = 3200$ for the air inlet, based on the air velocity and the half-width of the air inlet, and $Re = 7000$ for the fuel jet, based on the fuel velocity and the radius of the fuel nozzle. Therefore, the referenced Reynolds number is sufficient for the present work.

The inflow gas temperature and static pressure of both species are at standard atmospheric temperature and pressure. A no slip condition was applied on the bluff body plate. On the radial boundary constant axial velocity components and species corresponding to the coflow were set. The downstream plane of the domain was set as

outflow boundary where velocity and species gradients are zero.

The following section will first show the instantaneous flow visualisations to illustrate the turbulent flow structure. Next, temporally and spatially averaged velocity, root mean square (rms) velocity and mixture fraction profiles are compared with experimental data. Following these comparisons, we will then discuss the kinetic energy spectra to assess effects of grid resolution and order of reconstruction limiters in the ILES computation.

3.5.2 Instantaneous Flow Structure

The instantaneous flow field was examined to deduce the structure of the large scale eddies. Figure 3.4(left) shows fuel volume fraction contour flood of the fully turbulent flow field. The simulation was performed on the fine grid with the fifth-order accurate limiter, and the corresponding physical time from fuel injection is $163.9\,ms$. Note that air was applied as fuel in this computation as described in the previous section. The central fuel jet is laminar up to axial distance $z/D = 0.4$. Then the jet breaks up immediately and a highly turbulent region can be seen up to $z/D = 1.0$ where the fuel concentration is reduced to less than 0.5. Low fuel concentration region is formed by recirculation flow over the bluff body plate ($-0.5 < r/D < 0.5, z/D = 0.0$) and below $z/D = 1.0$. Normalised vorticity magnitude at the same instant is shown in Figure 3.4(right). A high vorticity region where mixing of the fuel and air is enhanced exists only in the vicinity of the central fuel jet and up to $z/D = 1.0$.

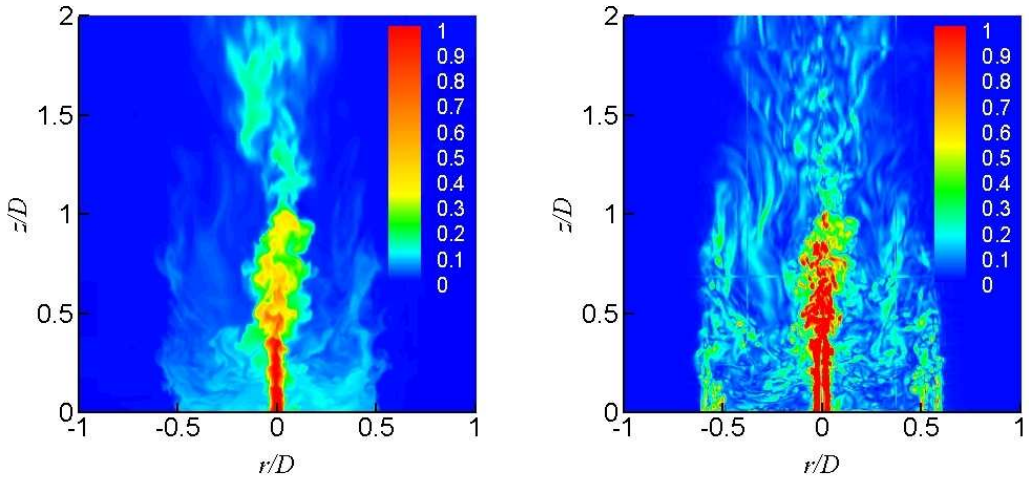

Figure 3.4: Instantaneous snapshot of volume fraction (left) and normalised vorticity magnitude (right) (fifth-order limiter, fine grid)

3.5.3 Sensitivity to Boundary Inflow Condition

As reported in [47], the flow structure is very sensitive to the inlet boundary condition. While the mean velocity inlet boundary was set to be the same as the experimental data, no experimental data is available for the level of turbulence at the inlet and hence axial, radial and circumferential fluctuating components were added based on the results of DNS [49]. Figure 3.5 shows that adding a larger fluctuating component (corresponding to 7.6% of the mean axial velocity of the fuel inflow) shows a larger deviation than a 1.5% fluctuating velocity in some regions e.g., $r/D = 0.05$, $z/D = 0.136$ and $r/D = 0.4$, $z/D = 0.4$. It should be noted however, as will be shown in the next section, that the experimental data for mean radial velocity exhibits discrepancies from ideal results at the centreline, and that the maximum discrepancy corresponds to 4.5% in the graph. Considering this uncertainty the setting of 7.6% fluctuation gives reasonable agreement to the experimental data apart from $x/D = 0.08$, $z/D = 0.136$. These observations confirm that the inflow fluctuation has a large influence to the flow structure and hence, a detailed setup of the inflow velocity fluctuations as the same as the experimental condition should result in a better match to the experimental values.

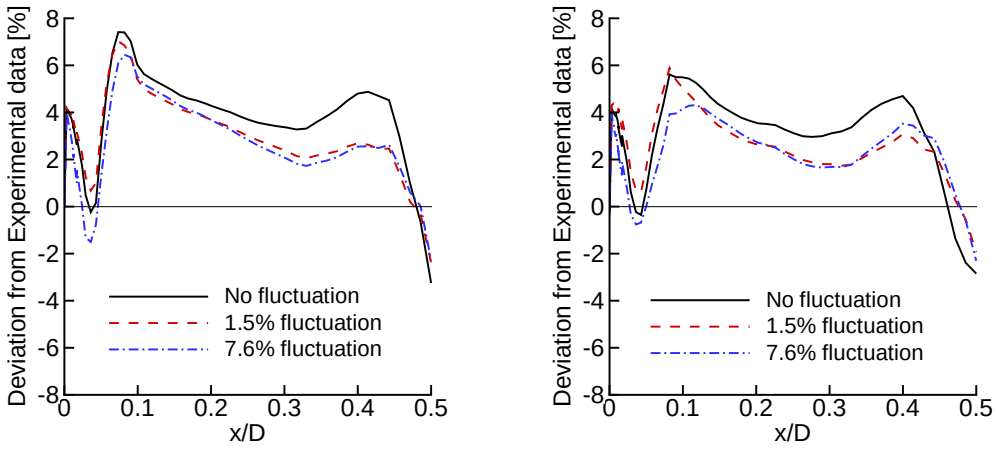

Figure 3.5: Effects of inflow fluctuation at $z/D = 0.136$ (left) and $z/D = 0.4$ (right)

3.5.4 Mean Flow

The temporal velocity fluctuations were examined to set the sampling start and end time for calculation of mean properties. The time histories of 35 spatial points were measured at a single $z - r$ plane. These points are located in and on the edge of the large scale flow structures, i.e., a recirculation zone which is estimated from the instantaneous flow structure. Figure 3.6 (left) shows a time history of axial and radial velocity at $(r/D, z/D) = (0.0, 0.4)$. The sampling start time can be set once the turbulent flow is fully developed and the fluctuation settles down to a statistically steady

condition. From Figure 3.6 (left), the time can be set at after nondimensional time $D/u_{f0} = 40$. In the current simulation the sampling start time was set at 60 which corresponds to approximately four times passage of the coflow through the computational domain. Figure 3.6 (right) shows a time history of the time-averaged axial velocity. Even after a long sampling time the time-averaged values still continue to vary, therefore, the sampling end time is set when the maximum variance in the period of 16.5 (time for coflow to pass the domain) gets down to 0.1% of fuel inlet condition. The sampling end time in this manner was set to 230 meaning that the sampling period is approximately 14 times passage of the coflow through the computational domain. The obtained sampling period is much larger compared to previous research [48] in which 2.4 times of the coflow field was used.

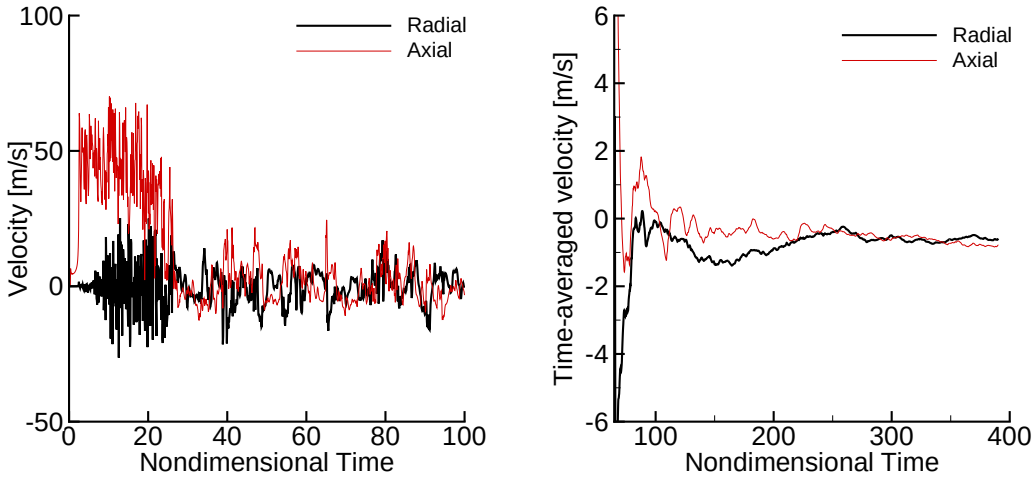

Figure 3.6: Time history (left) and time-averaged velocity (right) at a single spatial location

The instantaneous velocity and mixture fraction field were averaged. Figure 3.7 (left) shows a contour flood of the temporally averaged axial velocity normalised by u_{f0}, the mean fuel inlet velocity at the centre ($r/D = 0.0$). The simulation was performed on the fine grid with a fifth-order accurate limiter. With a long physical sampling time of $114.8\,ms$ which corresponds to more than nine times passage of the coflow through the computational domain, an axially symmetric flow field was obtained. It clearly depicts the location of recirculation zones where the axial velocity is negative at $0.1 < |r/D| < 0.4$, $z/D < 1.0$ region. Figure 3.7 (right) shows the contour of the temporally averaged axial rms velocity of the same flow and the same sampling time. The data is also normalised by u_{f0}. A high rms velocity region lies mainly on the centreline at around $z/D = 0.4$. Although the sampling time is very long, small asymmetries can still be seen in this region. This is clearly illustrated in Figure 3.8. The left hand side graph shows a symmetric 3D picture of the averaged axial velocity while the right hand side shows an asymmetric feature of the averaged axial rms velocity.

Comparisons of the mean flow with experimental data [59] were performed at $z/D = 0.4$, 0.8 and 1.4, corresponding to a location of strong turbulence and the centre of

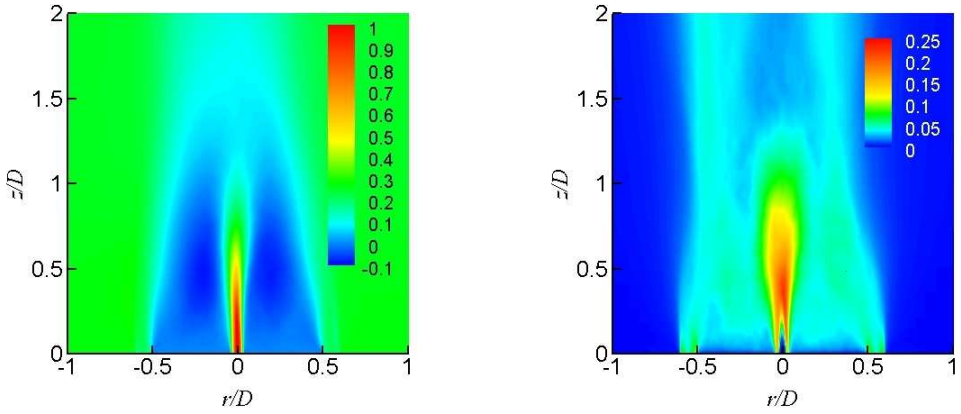

Figure 3.7: Temporally averaged axial velocity (left) and axial rms velocity (right), normalised by the mean fuel inlet velocity at the centre (fifth-order limiter, medium grid)

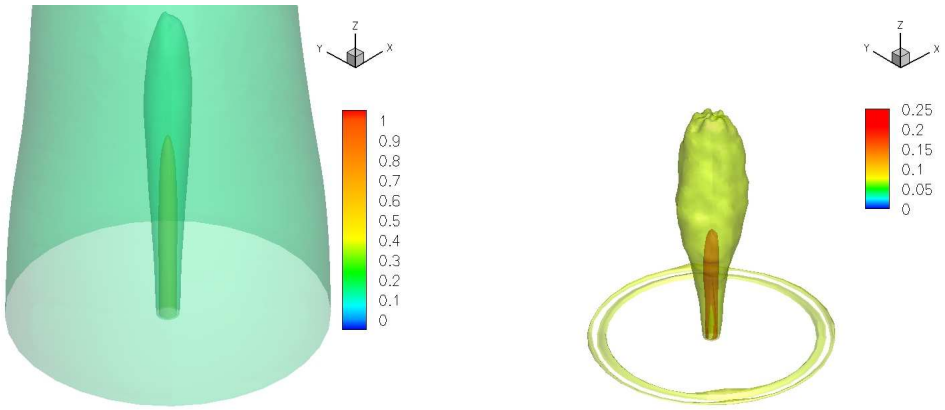

Figure 3.8: Averaged axial velocity of 0.15 and 0.5 iso-surfaces in 3D (left), averaged axial rms velocity of 0.07 and 0.2 iso-surfaces in 3D (right),normalised by the mean fuel inlet velocity at the centre (fifth-order limiter, medium grid)

the recirculation zone, the top boundary of the recirculation zone, and the downstream region, respectively. Although the flow field in Figure 3.7 (left) is almost axially symmetric, circumferential averaging of the flow is applied to take into account the spatial variance of the flow structure, e.g., shown in Figure 3.4.

Figure 3.9 shows mean axial velocity and axial rms velocity. In general, the ILES results match the experimental data well in all axial locations. Note that the experimental data consists of three sets of measurement.

At $z/D = 0.8$ and 1.4, a velocity deviation from the experimental data can be seen at the centreline $r/D = 0.0$ where the velocity gradient is very large and a small axial difference causes a large velocity deviation. Also, a large rms velocity at $(r/D, z/D) = (0.0, 0.4)$ implies that the inflow boundary fluctuation velocity is larger than the experimental data and hence, reduces the axial velocity more rapidly causing a deviation of the axial velocity at the centreline. The radial locations of zero axial velocity are

useful information since they can indicate core of the recirculation zones and the ILES results predict them precisely.

Figure 3.10 shows mean radial velocity and radial rms velocity. Again, in general, the ILES results show good agreement with experimental data. Although deviation can be observed particularly in near central fuel jet region, it should be noted that the velocities are small compared to the axial velocities. The experimental data consists of three sets of measurements and shows a large variance of mean velocity at $z/D = 0.8$ and rms at $z/D = 0.4$ and 0.8, where the rms velocity level is higher than the mean values. In these regions simulations also show some deviation from the experimental data, which implies that the radial velocity and its rms of these regions are sensitive to the flow settings, e.g., the inflow boundary condition. The radial locations of zero radial velocity in this graph indicate the boundary of the recirculation zones and the ILES computation predict them well.

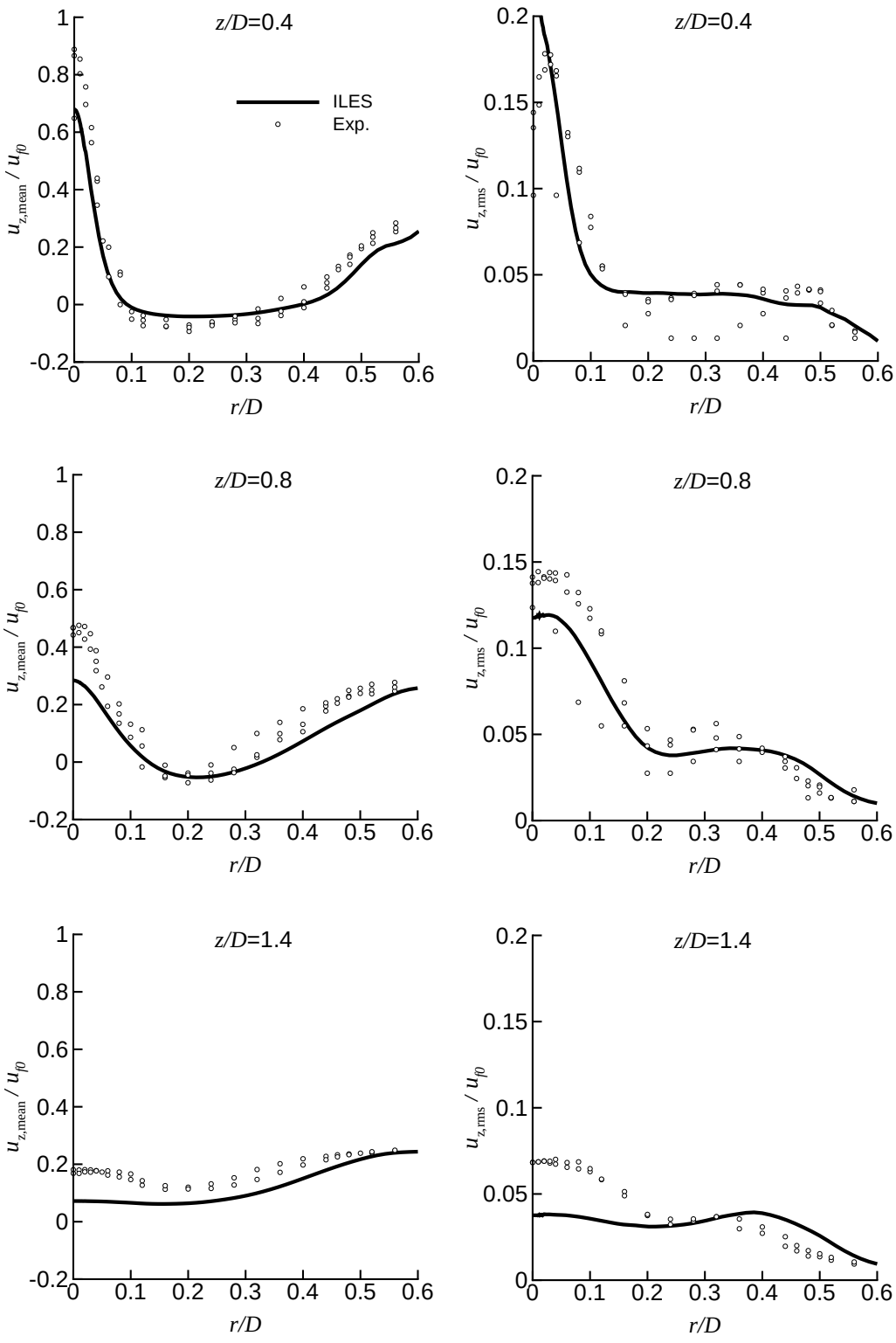

Figure 3.9: Mean axial velocity (left) and axial rms velocity (right) (fifth-order limiter, medium grid)

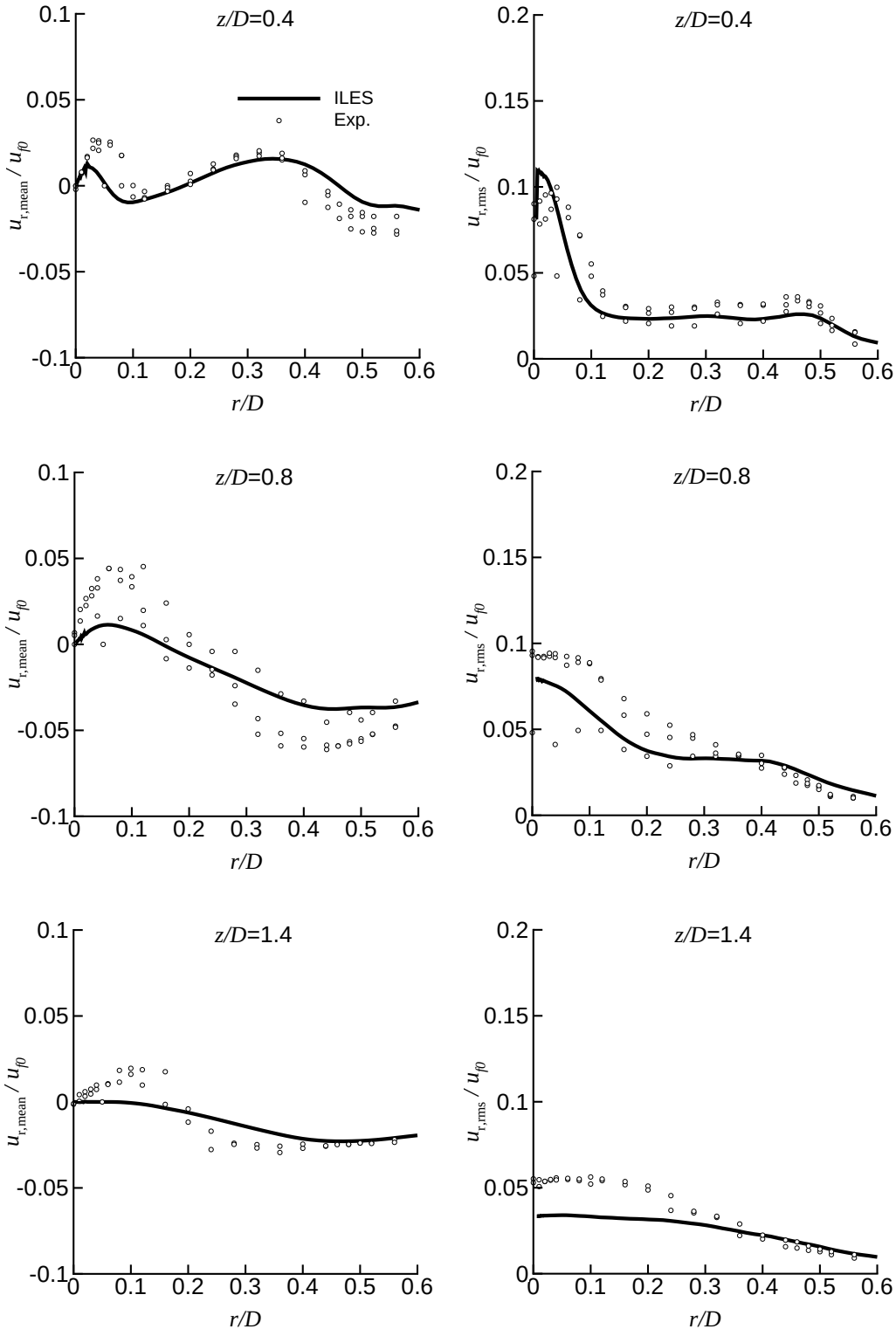

Figure 3.10: Mean radial velocity (left) and radial rms velocity (right) (fifth-order limiter, medium grid)

3.5.5 Multi-Species Mixing Field

Since no chemical reaction is considered, only two quiescent species, i.e., methane and air exist in the field, hence the mixture fraction f can be defined as identical to the fuel mass fraction:

$$f = \frac{\alpha_f \rho_f}{\alpha_f \rho_f + \alpha_o \rho_o} \tag{3.5.1}$$

Figure 3.11 shows the ILES results of mean mixture fraction and rms mixture fraction compared with experimental data [59]. Also, as described in the previous section, the variance of the experimental data implies the sensitivity of the flow. By tracking volume fraction among quasi conservative equations, the ILES shows good agreement with experimental data.

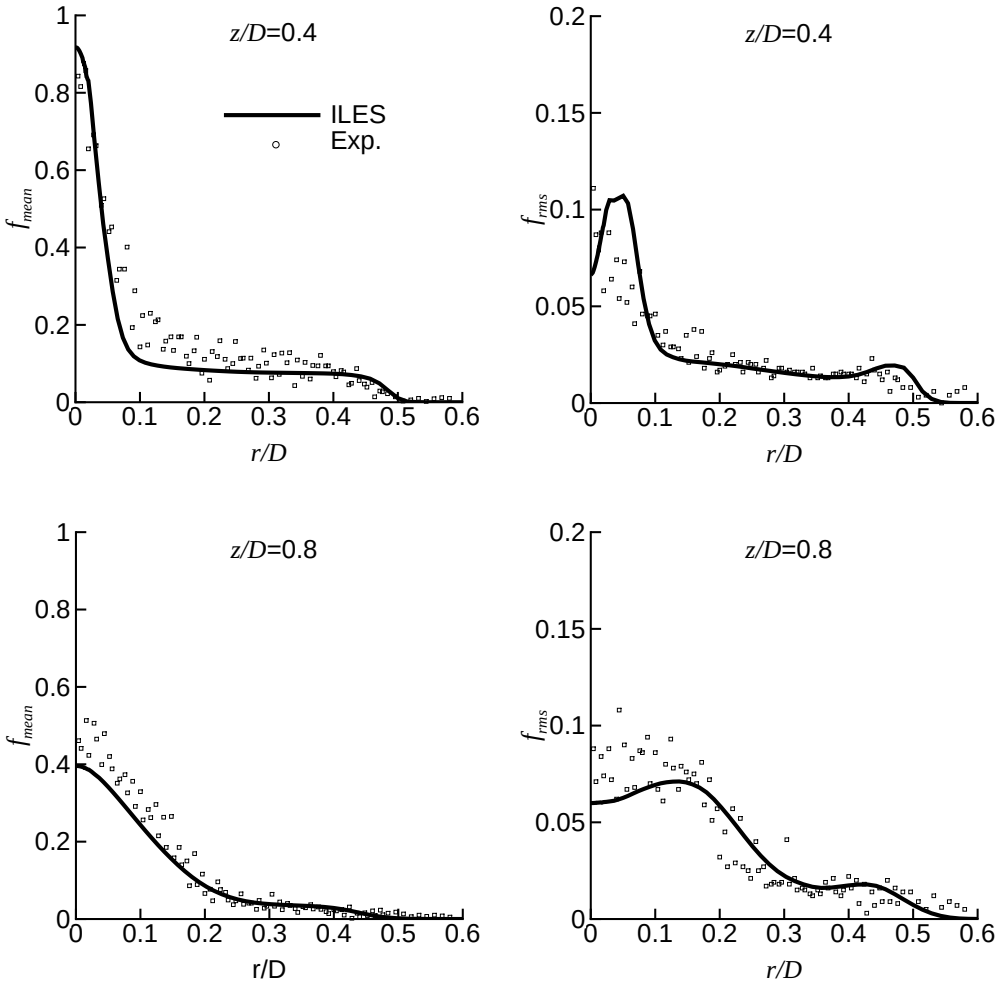

Figure 3.11: Mean mixture fraction (left) and rms mixture fraction (right) (fifth-order limiter, medium grid)

3.5.6 Effects of Grid Resolution

Figure 3.12 (left) shows the comparison of the mean axial velocity profile on the centreline ($r/D = 0.0$) for different grid sizes. The medium and fine grid simulation show good convergence in $z/D < 0.6$ region and with maximum 3% difference in $z/D > 0.6$ region while the coarse grid result indicates maximum 8% deviation from the fine grid data. Note that all simulations in this sub-section were performed with the fifth-order accurate limiter. Figure 3.12 (right) shows axial rms velocity of the same simulation and clearly shows the advantage of the medium and fine grid. At $z/D = 0.4$ rms velocity is still larger than the experimental data which resulted in the deviation of the mean profile in the previous section. The effect of circumferential resolution was investigated by a grid having double points in the circumferential direction. The centreline velocity decayed faster compared to grids having normal points in the circumferential direction. The reason for this is a large fluctuation velocity at near jet nozzle ($0.1 < z/D < 0.3$) as shown in the rms velocity in Figure 3.12 (right).

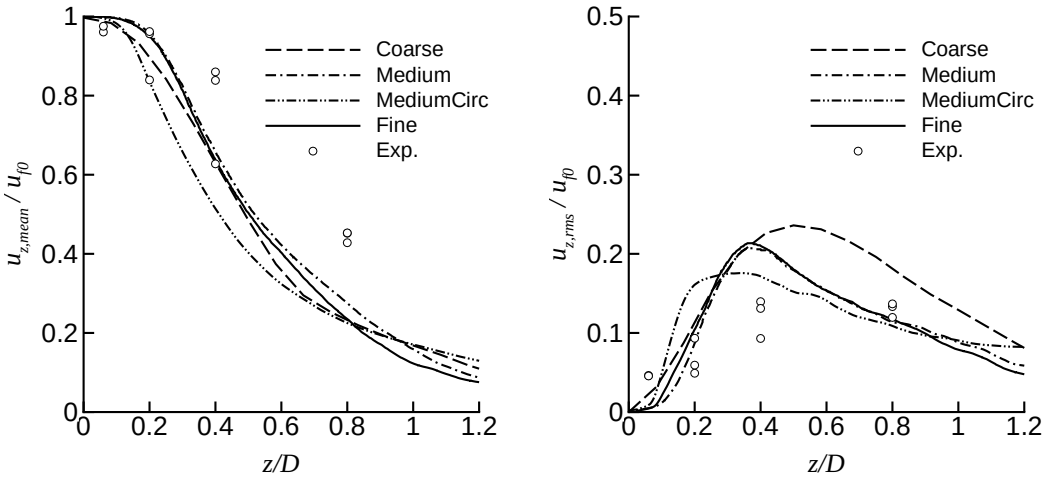

Figure 3.12: Mean axial velocity (left) and axial rms velocity (right) at $r/D = 0.0$ for different grid sizes, normalised by the mean fuel inlet velocity at the centre (fifth-order limiter)

The kinetic energy spectra were analysed to evaluate the performance of the implicit dissipation in the ILES approach by examining the behaviour of the resolved (unaffected by numerical dissipation) and unresolved scales (directly damped by numerical dissipation). The one dimensional kinetic energy spectrum $E_k(k,t)$ is defined as the square of the Fourier transform of the velocity:

$$E_k(k,t) = \frac{1}{2\pi}\left|\int_{\infty}^{\infty} u(x_j,t) exp^{-Ikx_j} dx_j\right|^2 \tag{3.5.2}$$

where k and $u(x_j,t)$ denote wavenumber and velocity component in j direction, respectively. This was computed using the velocity time history at a selected spatial location with physical sampling time $114.8ms$ which corresponds to approximately 28 times

passage of the fuel flow through the computational domain. Firstly, the fluctuating velocity field was examined to determine the appropriate spatial location to calculate the kinetic energy spectra. A region of strong turbulence can be seen at around $z/D = 0.4$ on the centreline in Figure 3.7 (right) hence the point $(r/D, z/D) = (0.0, 0.4)$ was selected. The kinetic energy spectra was calculated based on axial velocity components on the coarse, medium and fine grid. In Figure 3.13 the medium grid and fine grid results are almost identical demonstrating good convergence of the computation and grid independence. An inertial sub range in which the slope of the line is close to $k^{-5/3}$ [51] can be seen for all grids, particularly for the medium and fine grid. In the coarse grid, the 'cut-off'wavenumber k_{co} which describes the deviation point from $k^{-5/3}$ line is around 1.5×10^3. Since any subgrid model does not account subgrid scale perfectly, an increase of the grid resolution can result in reducing the effects of numerical method and hence, the cut-off wavenumbers can be shifted to a higher value. In Figure 3.13 the inertial range extends the cut-off wavenumber up to 2.0×10^4 as the grid resolution increases. Note that the highest wavenumber k_{max} in Figure 3.13 can be obtained about 5×10^4, which is corresponding to the minimum wave length on the grid as $2\pi/k_{max} = 1.3 \times 10^{-4}[m]$. Since the smallest grid spacing which can be seen at the central square mesh $7.5 \times 10^{-5}[m]$ is smaller than k_{max} the highest wavenumber was produced on the grid scale and was resolved.

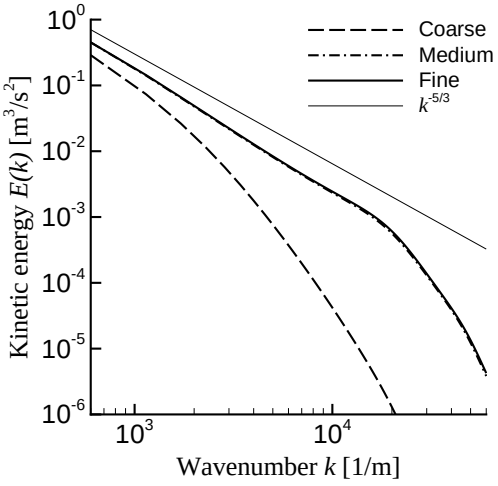

Figure 3.13: Kinetic energy spectra for different grid sizes (fifth-order limiter)

Finally, the maximum wavenumber k_{grid} produced by an instantaneous eddy rotation was estimated from the smallest possible eddy turnover time at a given grid. From the vorticity magnitude illustrated in Figure 3.4(right) the location of the eddies containing maximum vorticity is close to the centreline. With the assumption that the eddy containing maximum vorticity produces maximum velocity frequency, the corresponding k_{grid} are calculated. Table 3.2 shows that for all grid sizes the ratio of k_{grid} calculated above to the k_{co} are smaller than unity on the given grid, which means the ILES accounted for the energy transportation between large and small eddies appropriately.

Table 3.2: Effect of grid resolution on the effective cut-off wavenumbers

Grid	k_{co}	k_{grid}	k_{grid}/k_{co}
Coarse	1.50×10^3	1.10×10^3	0.73
Medium	1.50×10^4	5.15×10^3	0.34
Fine	1.50×10^4	5.37×10^3	0.36

3.5.7 Influence of Order of Spatial Accuracy

Simulations with three different limiters which have second, fifth and ninth-order of accuracy, respectively, were carried out on the medium grid since the medium grid results in the previous sub-section showed good resolution of the kinetic energy with a smaller computational power than the fine grid. Figure 3.14 (left) shows the influence of spatial accuracy of the limiters on the mean axial velocity profile on the centreline ($r/D = 0.0$). The three lines indicate only small differences, showing that the choice of the order of spatial accuracy higher than second order does not have significant effect on the temporally averaged velocity profile in this test case. Also, in Figure 3.14 (right) axial rms velocity profiles of the same simulation illustrate small effects of the order of limiters.

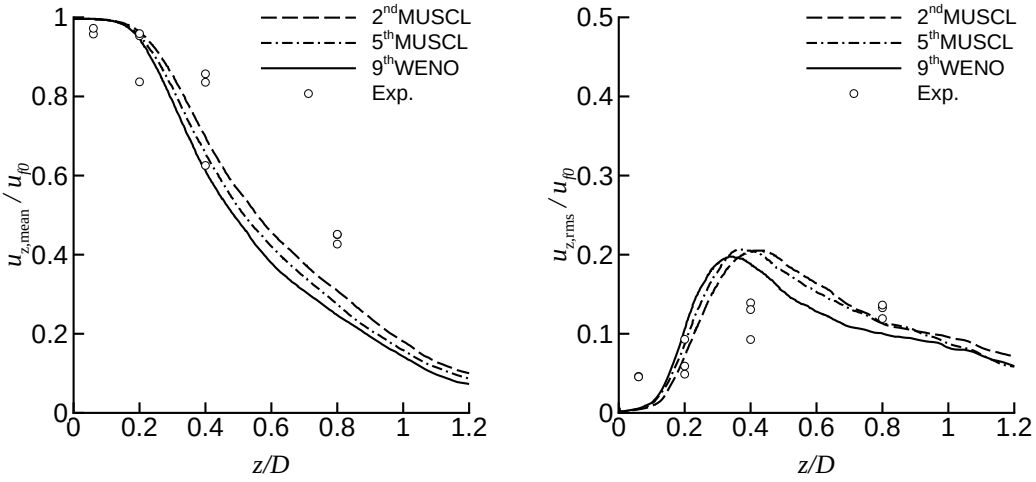

Figure 3.14: Mean axial velocity (left) and axial rms velocity (right) at $r/D = 0.0$ for different limiters, normalised by the mean fuel inlet velocity at the centre (medium grid)

Figure 3.15 shows a comparison of the kinetic energy spectra gained using each of these limiters, focusing on the region close to the effective cut-off. An increase of the cut-off wavenumber can be seen as the order of accuracy of the limiter increases from second to fifth. However, the ninth-order limiter shows high kinetic energy in high wavenumbers ($2.0 \times 10^4 < k < 3.0 \times 10^4$) which implies that the numerical dissipation

in this frequency range was smaller than ideal. As a result, the cut-off wavenumbers are close to the second and fifth order limiter.

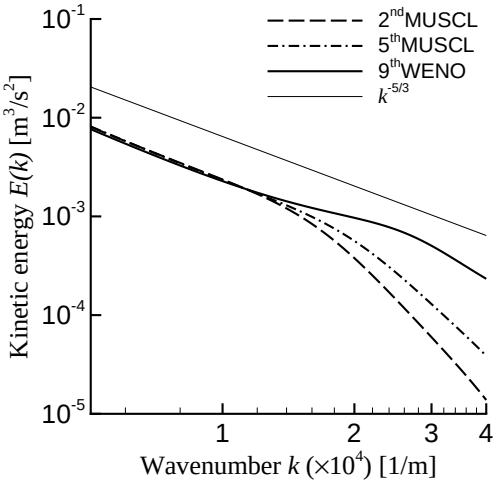

Figure 3.15: Kinetic energy spectra for three different orders of spatial accuracy (medium grid)

Table 3.3 summarises the properties of the kinetic energy spectra for different limiters: k_{co}, k_{grid}, k_{grid}/k_{co} and a comparison of the required simulation time t_{sim} normalised by the time with the second-order limiter. The ratio k_{grid}/k_{co} are smaller than unity for all grid sizes. The fifth-order limiter showed a larger cut-off wavenumber and required only a slightly larger simulation time compared with the second-order limiter. With the ninth-order limiter more than three times of the computational resource was necessary compared to the second-order limiter.

Table 3.3: Effects of limiter choice on energy resolution and simulation time

Limiter	k_{co}	k_{grid}	k_{grid}/k_{co}	t_{sim}
2^{nd} MUSCL	1.20×10^4	5.14×10^3	0.43	1
5^{th} MUSCL	1.50×10^4	5.15×10^3	0.34	1.08
9^{th} WENO	1.50×10^4	5.57×10^3	0.37	3.61

3.6 Effects of Atwood Number

The formation of the complex flow field is triggered by flow instabilities. The velocity differences between the fuel jet and the inflow air causes Kelvin-Helmholtz instability, and the density of fuel ρ_f, which is usually different from density of air ρ_a, induces Rayleigh-Taylor instability in the mixing field. In the research on the effects of density ratio, experimental measurements were conducted for flows with lighter and heavier gas jet injection to the ambient gas [76, 97, 23]. Numerical simulation were performed for a round jet [78, 41]. More fundamentally, Rayleigh-Taylor instability has been widely investigated with a parallel flow, such as by [11, 99, 98]. Here, an important nondimensional parameter describing density ratio of the fuel and air is Atwood number which is defined as:

$$At = \frac{\rho_a - \rho_f}{\rho_a + \rho_f} \tag{3.6.1}$$

Atwood number of gaseous fuel largely varies as shown in Figure 3.16. The density of ethylene is similar to air and hence Atwood number is close to zero while hydrogen has a large number $At = 0.871$. Methane is a common fuel gas and it is sometimes used in laboratory experiments by mixing with hydrogen. Therefore, methane base gases have moderate Atwood numbers, and with volume ratio 1:5, the mixture obtains a similar Atwood number to helium which is well investigated as a typical light weight gas. Despite this large variety of the fuel gases only few research has covered the wide range of the Atwood number. Also, the complex mixing flow field has not been described by density ratio parameters and hence, information of Atwood number effect on the fuel burner flow field is still missing.

3.6.1 Simulation Setup

The computational domain is cylindrical and set as the same as in the previous section. The ILES computations in the previous section showed a 0.60×10^6 grid, consisting of 300, 62, and 32 meshes for axial, radial and circumferential direction was found to be sufficient for flow field analyses, and hence adopted for all computation in this section.

The test cases are summarised in Table 3.4 with u_{f0} and γ_f representing fuel inflow velocity and ratio of specific heats of fuel, respectively. In the test case $At = 0.526$ and 0.740, fuel jets consists of methane and hydrogen with volume fraction ratio 1:1 and 1:5, respectively. Fuel inlet velocities were set such that the momentum flux of the fuel jet can be identical at the nozzle exit. Note that only fuel gases whose weight are lighter than air are considered since Kelvin-Helmholtz instability and flow physics differ for heavy gases. Both the air flow from the annular inlet and the coflow are constant at $20.0 m/s$ for all test cases. Note that the inflow of the fuel jet and air flow are axial and have a simple flat velocity profile. Also note that no velocity fluctuations

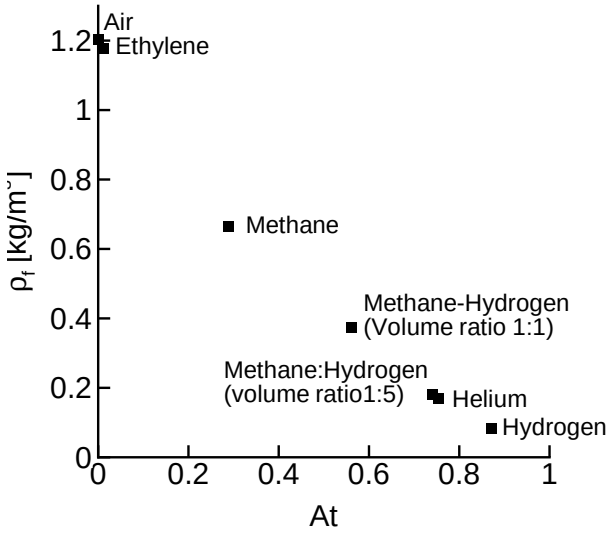

Figure 3.16: Atwood number of fuel against air. Helium and air are plotted as reference

were added to these inflow velocity condition. Pressure and temperature of the fuel and air were the same 1atm and 293K, respectively. No chemical reaction was considered.

Table 3.4: Test cases for investigation of Atwood number effects

Jet(volume ratio)	At	$u_{f0}(m/s)$	γ_f
Air	0	63.2	1.40
Ethylene	0.011	63.9	1.24
Methane	0.288	85.0	1.31
Methane : *Hydrogen*=1:1	0.526	113.3	1.35
Methane : *Hydrogen*=1:5	0.740	163.4	1.39
Hydrogen	0.871	240.6	1.41

The local Mach number at the fuel jet nozzle is 0.18 – 0.19 for all cases since the momentum fluxes at the fuel jet nozzle are the same. The local Reynolds number based on air inflow velocity, the bluff body plate diameter D and air viscosity is 7.0×10^4 for all test cases while the local Reynolds number based on the fuel jet velocity at nozzle exit, fuel nozzle diameter and fuel viscosity varies from 0.8×10^4 to 2.0×10^4. However, the simulation described in the following section showed that no significant difference was observed in the flow field for this range of Reynolds number, and hence the effect of Reynolds number is assumed to be small in this simulation. A numerical simulation on simple circular jets and plane jets by [78] also showed that the Reynolds number effect is much smaller than the density effects.

3.6.2 Mean Flow Structure

The ILES instantaneous flow data was averaged to obtain the mean flow. The fuel burner geometry is axisymmetric but the flow field needs to be averaged spatially, i.e., circumferentially as well as temporally, due to high turbulence, as described in the previous section. The data sampling started after $50.0ms$ when the turbulent flow was fully developed. The sampling period was $100.0ms$ corresponding to eight times passage of the air flow through the computational domain. Figure 3.17 shows mean streamlines, the axial velocity component and fuel volume fraction contours for three different Atwood number test cases. Note that the scale is magnified to the radial direction in order to illustrate the vortices and recirculation zones clearly. In the streamline figures, an inner and an outer vortices can be observed for all test cases. The centre of the vortices are located at around $(r/D, z/D) = (0.1, 0.7)$ and $(0.35, 0.7)$, respectively, and almost unchanged with the increase of Atwood number. The recirculation zone which can be defined as an inner region of the boundary of the inner and the outer vortices lies in $(0 < r/D < 0.5, 0 < z/D < 1.0)$, and also independent of Atwood number. The boundary between the inner and the outer vortices can be observed at around $r/D = 0.2$. The fuel jet from $(0 < r/D < 0.036, z/D = 0)$ and air flow from $(0.5 < r/D < 0.6, z/D = 0)$ collide at a point on this boundary $(r/D, z/D) = (0.2, 1.0)$, mix together, then a portion of the gas flows makes the recirculation zone. The streamlines $z/D < 0.2$, vary for different Atwood numbers due to small velocities and unsteady direction of the flow in this region.

The velocity contours also illustrate that the flow field, except for the central fuel jet region, is not influenced by the change of Atwood number. A large negative axial velocity region including the outer vortex can be observed at $(0 < r/D < 0.5, 0 < z/D < 1.0)$.

The volume fraction contours however, change with the increase of Atwood number due to the increase of the fuel volume flow rate injected into the domain. A large region of constant but relatively low volume fraction is formed neat the injector bluff body plate, $(0.1 < r/D < 0.4, 0 < z/D < 0.5)$. The volume fraction in this region also increases with Atwood number and corresponds to the volume fraction at the mixing point stated above $(r/D, z/D) = (0.2, 1.0)$, and hence the amount of fuel entrained in the recirculation zone can be controlled by the mixing condition at this point.

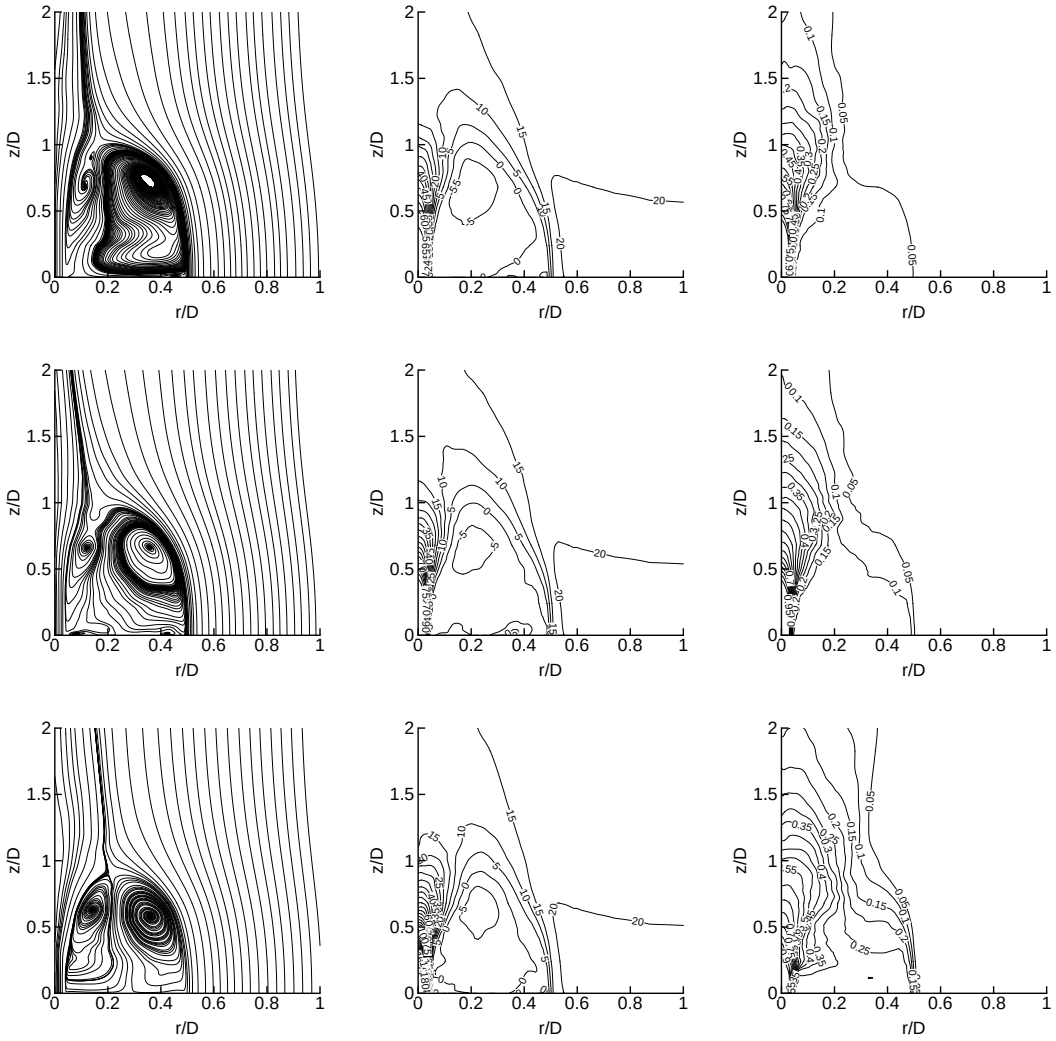

Figure 3.17: Mean streamline (left), axial velocity contour [m/s] (middle) and fuel volume fraction contour (right) for three different Atwood number: $At = 0$ (top), $At = 0.288$ (middle), and $At = 0.740$ (bottom)

3.6.3 Velocity and Mixing Profile

Since the velocity field changes took place only near the fuel jet region the velocity profile was examined along the central axis. Figure 3.18 shows the profile of the mean axial velocity component. The velocities are normalised by the fuel inlet axial velocity u_{f0} of the $At = 0$ (Air jet) case. The fuel jet velocity remains constant at $0 < z/D < 0.4$, then, reduces to collapse to an identical line at $z/D = 1.0$ since the momentum flux is the same for each test cases.

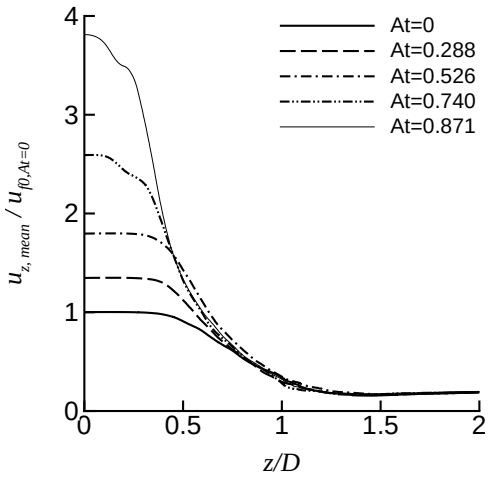

Figure 3.18: Mean axial velocity at centreline for different Atwood number

Figure 3.19 shows the Atwood number effect on the axial velocity decay rate β. This parameter is defined as the maximum gradient of the velocity inverse, u_{f0}/u_z, in the range of $(0 < z/D < 1.5)$ where the velocity reduces continuously as shown in figure 3.18. With the increase of Atwood number the decay rate increases monotonically.

Figure 3.20 shows the mean fuel volume fraction and rms fuel volume fraction for different Atwood number flows. The profiles show radial distributions at constant distance plane from the bluff body plate, $z/D = 0.6$ and 1.0 where the vortices centres and the mixing point $(r/D, z/D) = (0.2, 1.0)$ are located. A corresponding experimental data set is available in [59] for $At = 0.288$ (methane jet case). The mean volume fraction graph at $z/D = 0.6$ shows that it is constant in the outer vortex region $(r/D > 0.2)$ for low Atwood number while the constant volume fraction region is limited to the outer side of the outer vortex, i.e., $r/D > 0.3$, for high Atwood number. At $z/D = 1.0$, since no recirculation flow can be seen at this distance, the volume fraction decreases continuously with the increase of radius. The rms volume fraction graph at $z/D = 0.6$ shows no clear correlation to Atwood number. However, at $z/D = 1.0$, the rms volume fraction has a local maximum at the mixing point $(r/D = 0.2)$ for all test cases and the values increase with Atwood number. This implies that fuel and air mixing is enhanced at this point at high Atwood number.

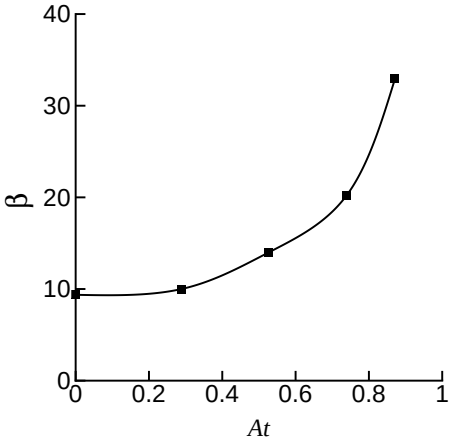

Figure 3.19: Atwood number effect on axial velocity decay rate of the fuel jet

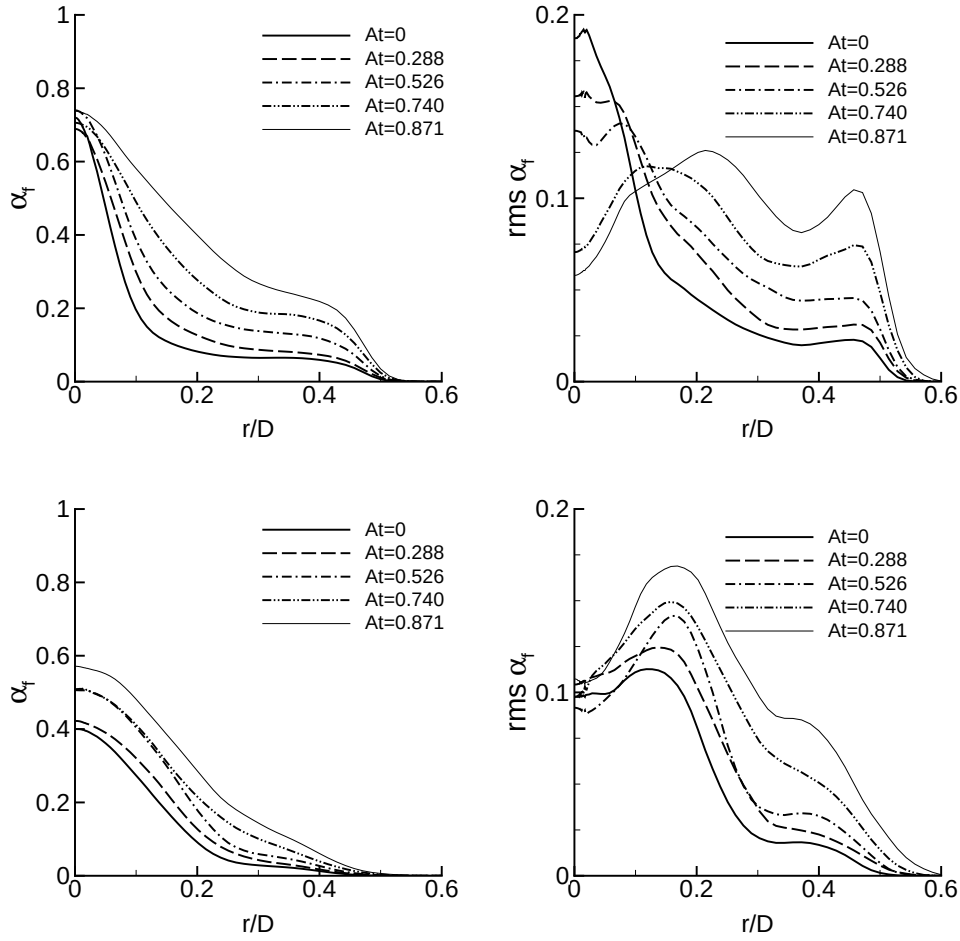

Figure 3.20: Radial distribution of the mean volume fraction (left) and rms volume fraction (right) for different Atwood number at $z/D = 0.6$ (top) and 1.0 (bottom)

3.6.4 Mixing Parameter

The rms volume fraction profile in Figure 3.20 illustrates the region of high turbulent intensity. Considering ignition of the flammable gas mixture it is useful to investigate the degree of mixing of the flow in this region. In order to describe the mixing of multi-species fluids several parameters have been considered. A mass flow rate passing through a plane normal to the jet axis was introduced in [76]. This simple parameter has been used largely for simple jets with and without coflow, however, it does not account for molecular mixing of fuel and air. Furthermore, it is not useful for flows including negative velocity components caused by large eddies and recirculation zones. Therefore, for a complex flow field, a parameter consisting of only scalar variables is preferable. In the research on Kelvin-Helmholtz mixing layer, a molecular mixing parameter based on mixture gas density and volume fraction was applied in [98]:

$$\varphi = 1 - \left(\frac{\rho_{rms}}{\rho_a - \rho_f}\right)^2 (\alpha_a \alpha_f)^{-1} \tag{3.6.2}$$

where the density term $(\rho_{rms}/(\rho_a - \rho_f))^2$ and the volume fraction term $(\alpha_a \alpha_f)^{-1}$ represent the density variance of miscible and immiscible fluids, respectively. Figure 3.21 shows the radial distribution of the mixing parameter at different distance from the bluff body plate for $At = 0.288$ (methane jet) test case. In the recirculation zone ($z/D = 0.4$) the mixing parameter is close to unity, which implies that the fuel and air are well mixed. At the edge of the recirculation zone ($z/D = 1.0$) the mixing parameter shows a local minimum at which the fuel and air flow collide but molecularly they are not well mixed. At a downstream ($z/D = 2.5$) the mixing parameter has no extremum, however, the value is still low and hence, a longer distance from the bluff body plate may be required for a complete mixing.

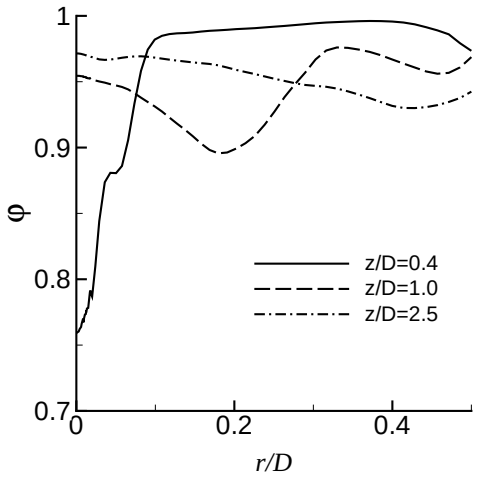

Figure 3.21: Molecular mixing rate for different distance from fuel jet nozzle ($At = 0.288$)

Figure 3.22 shows Atwood number effects on the mixing parameter at $z/D = 1.0$. It is illustrated that the degree of mixing reduces at the mixing point ($r/D = 0.2$) with the increase of Atwood number. The presented ILES results showed that the examined mixing parameter can be used to describe degree of mixing for complex turbulent multi-species flows, though it was originally introduced to analyse simple mixing layers of a parallel flow.

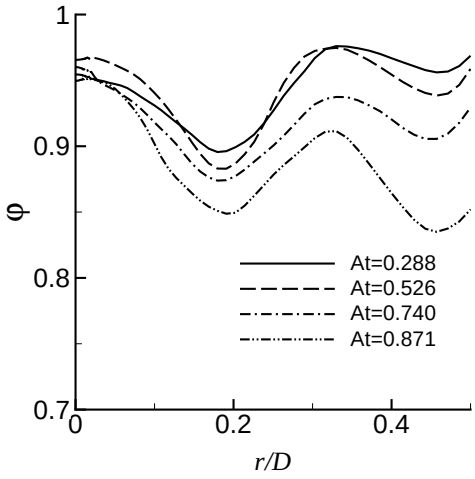

Figure 3.22: Molecular mixing rate at $z/D = 1.0$ for different Atwood number

3.7 Swirl Flow Simulation

Swirl flow is an essential feature of a fuel injector for rapid fuel-air mixing and flame stabilisation in gas turbine combustors. Swirl flow enhances mixing and at the same time forms recirculation zones which contribute to provide sufficient mixture residential time and appropriate fuel concentration for ignition. Therefore, a wide range of investigations have been done experimentally and computationally.

From the viewpoint of reliable ignition of a gas turbine, one requirement for a swirl injector is to form an appropriately large volume of flammable mixture near the injector ([52]). This is particularly essential when considering a jet engine relight operation at high altitude since the injector flow structure changes from that at the ground level. However, experimental research of these off design conditions of the injector flow are not usually conducted due to the high financial cost hence, only limited numbers of papers have been published, e.g., [75]. Therefore, computational research on the effects of gas properties and swirl intensity of swirl injector flows is necessary to understand swirl flow characteristics and to improve combustor design methodology.

3.7.1 Simulation Setup

The geometry of the swirl jet burner is the same as the previous sections. A swirling flow can be obtained by adding a circumferential velocity component to the annulus air inlet, as shown in Figure 3.23. Note that the central fuel jet has only the axial velocity component.

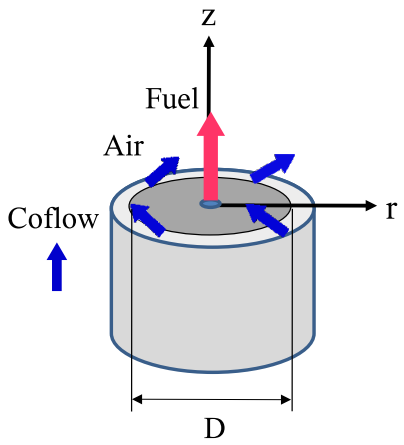

Figure 3.23: Geometry of the swirl flow burner

In the previous sections the ILES computations showed that a 0.60×10^6 grid consisting of 300, 62, and 32 meshes for axial, radial and circumferential direction, respectively, was found to be sufficient for flow field analyses, therefore this grid size is adopted throughout this section.

The simulation test cases are summarised in Table 3.5 with $u_{a0,z}$ and $u_{a0,c}$ representing axial and circumferential air inlet velocity (m/s), respectively. The radial air inlet velocity $u_{a0,r}$ is zero and the coflow is constant at $20.0m/s$ for all test cases. A swirl number SN which describes swirl intensity can be defined as the ratio of the circumferential velocity of air inflow to the axial velocity of air inflow, i.e., $u_{a0,z}/u_{a0,c}$. The Reynolds number based on the air inlet velocity, the bluff body diameter and standard air viscosity is 6.4×10^4 for the non-swirl case, 1.1×10^5 for the low swirl case and 9.7×10^4 for the high swirl case. Turbulent fluctuating components based on a DNS [49] were added to the fuel and air inflow. Simulations were also performed with a different gas. In order to examine pressure and viscosity effect on the flow structure.

3.7.2 Mean Flow Structure

The ILES instantaneous flow data was averaged to obtain the mean flow. The burner flow is axisymmetric but highly turbulent and needs to be averaged spatially, i.e., circumferentially as well as temporally, as described in the previous section. The time-averaged axial velocity contour flood plot for the low swirl case is shown in Figure 3.24 (left). The flow is axially symmetric and contains symmetric recirculation zones

Table 3.5: Inflow velocity [m/s] and gas properties for swirl flow test cases

	u_{f0}	$u_{a0,z}$	$u_{a0,c}$	SN	$\rho_f(kg/m^3)$	$p(atm)$	$\nu(\times 10^{-4} m^2/s)$
Non-swirl	61.0	20.0	0.0	0	1.20	1	0.15
Low swirl	66.0	29.7	16.0	0.54	1.20	1	0.15
High swirl	66.0	16.3	25.9	1.59	1.20	1	0.15
Non-swirl	61.0	20.0	0.0	0	0.93	1	0.15
Non-swirl	61.0	20.0	0.0	0	0.66	1	0.15
Non-swirl	61.0	20.0	0.0	0	0.66	0.5	0.15
Non-swirl	61.0	20.0	0.0	0	0.66	0.1	0.15
Non-swirl	61.0	20.0	0.0	0	0.66	1	0.62
Non-swirl	61.0	20.0	0.0	0	0.66	1	2.50

over the bluff body surface. Also, a large negative velocity (upstream flow) region can be seen near the centreline at $1.0 < z/D < 2.0$.

Next, the circumferential variance of the flow properties is examined since the turbulent flow evolves in three dimensional space. The time-averaged radial velocity at $z/D = 0.2$ is shown in Figure 3.24 (right) which is obtained by 32 data sets of circumferentially distributed points. It can be stated that the circumferential variance is not negligible particularly in the region near the central fuel jet, and hence, temporal and spatial (circumferentially in the current simulation) averaging was applied to obtain 'mean' flow properties. This spatial averaging was not considered in the experiments [62] although their averaging time is much longer.

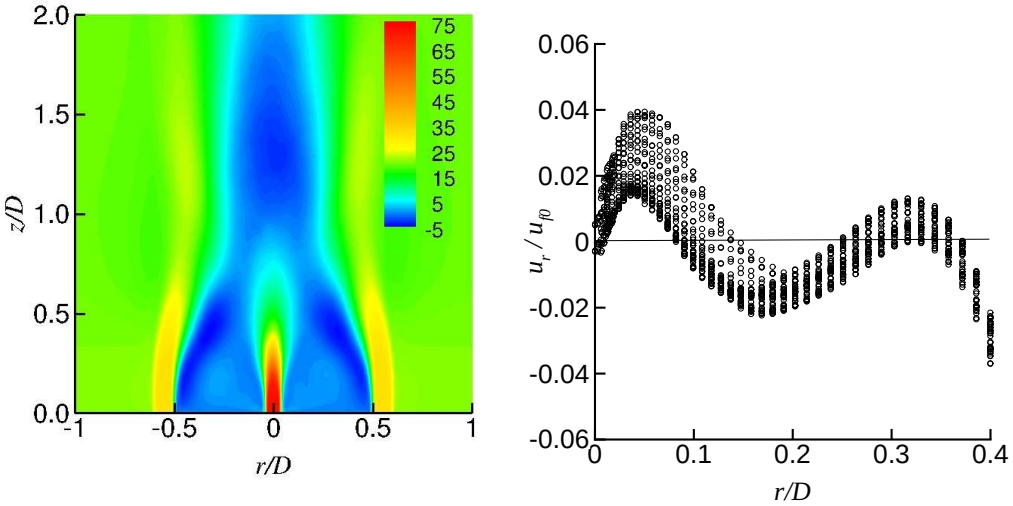

Figure 3.24: Swirl flow simulation: time-averaged axial velocity contour flood [m/s] (left) and circumferential variance of time-averaged radial velocity at $z/D = 0.2$ (right), normalised by the mean axial fuel inlet velocity at the centre

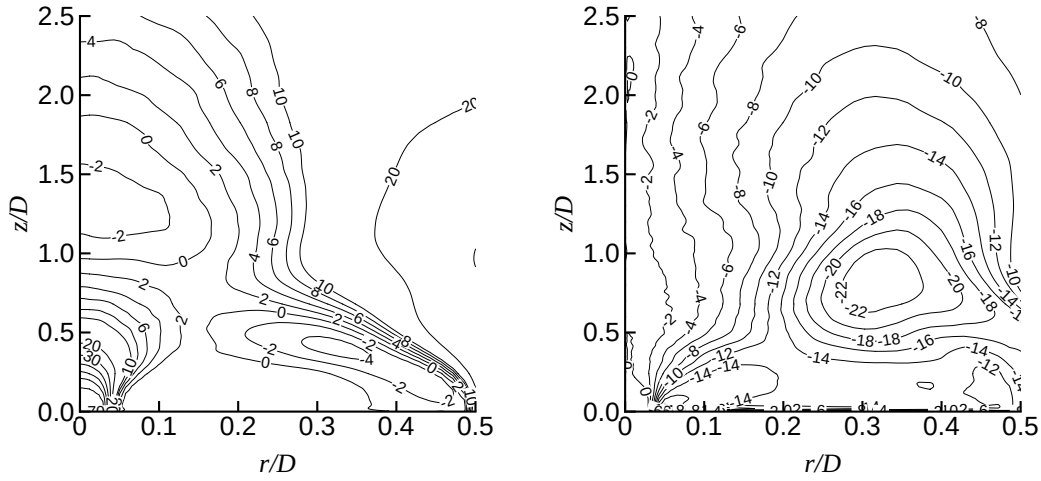

Figure 3.25: Swirl flow simulation: Mean axial velocity [m/s] (left) and circumferential velocity [m/s] (right)

Contours of the mean axial velocity are shown in Figure 3.25 (left). The axial length of a recirculation zone from the bluff body surface is located at $z/D = 0.6$ which is close to the experimental measurement 0.5 [2]. Another recirculation zone can be seen at $z/D = 1.0$ to 1.9 on the centreline, while experiments shows the location at $z/D = 1.0$ to 2.2. From the circumferential velocity contours in Figure 3.25 (right) the maximum circumferential velocity is predicted to be $23.5\,m/s$ which is slightly lower than the experimental observation of $26\,m/s$, but the location $z/D = 0.8$ and $x/D = 0.3$ corresponds to the experiments.

Figure 3.26-3.31 show comparisons of radial distribution of the axial, radial and circumferential mean velocity and rms velocity fluctuation profiles to the experimental data [60] at axial distances $z/D = 0.136, 0.2, 0.4, 0.8, 1.4$,and 2.0, respectively. In Figure 3.26 the axial velocity distribution shows good agreement in most parts of the flow field. At the centreline $r/D = 0.0$, velocities matches well to the experiments except at $z/D = 0.2$, where the velocity gradient is very large (Figure 3.25 (left)) and a small axial difference causes a large velocity discrepancy. At $z/D = 0.4$, the ILES predicts accurately the radial locations of the zero axial velocities which corresponds to the centre of the recirculation zones. The axial rms velocity fluctuations in Figure 3.27 show excellent agreement with experimental data except at the centreline $r/D = 0.0$ and the air annulus $0.5 < r/D < 0.6$, where the level of inflow boundary fluctuations have a large effect as described in the previous section. Circumferential velocities are plotted in Figure 3.28 and show reasonable agreement particularly in $z/D < 1.4$ region. At $z/D = 0.2$ and 0.4, the experimental data are not converged to zero at the centre line and there is still some asymmetry. The rms circumferential velocity fluctuation are compared in Figure 3.29. The computational results give a flat profile at $0.5 < r/D < 0.6$ near the bluff body surface region $z/D < 0.4$, while the experiments show small bumps. This is also due to the specification of inflow fluctuations. Radial

velocities described in Figure 3.30 show some discrepancies in all axial locations, but it should be noted that absolute quantities are smaller in this figure compared to axial and circumferential velocities. Regarding the velocities at the centreline, as previously mentioned, the ILES predicts zero velocities at centreline while experiment show small non zero values. In Figure 3.31 the radial velocity fluctuations show good agreement except for the near centreline and the air inlet region. These observations indicate that the ILES successfully computed flow field without explicit subgrid scale modelling, considering the complex flow structure.

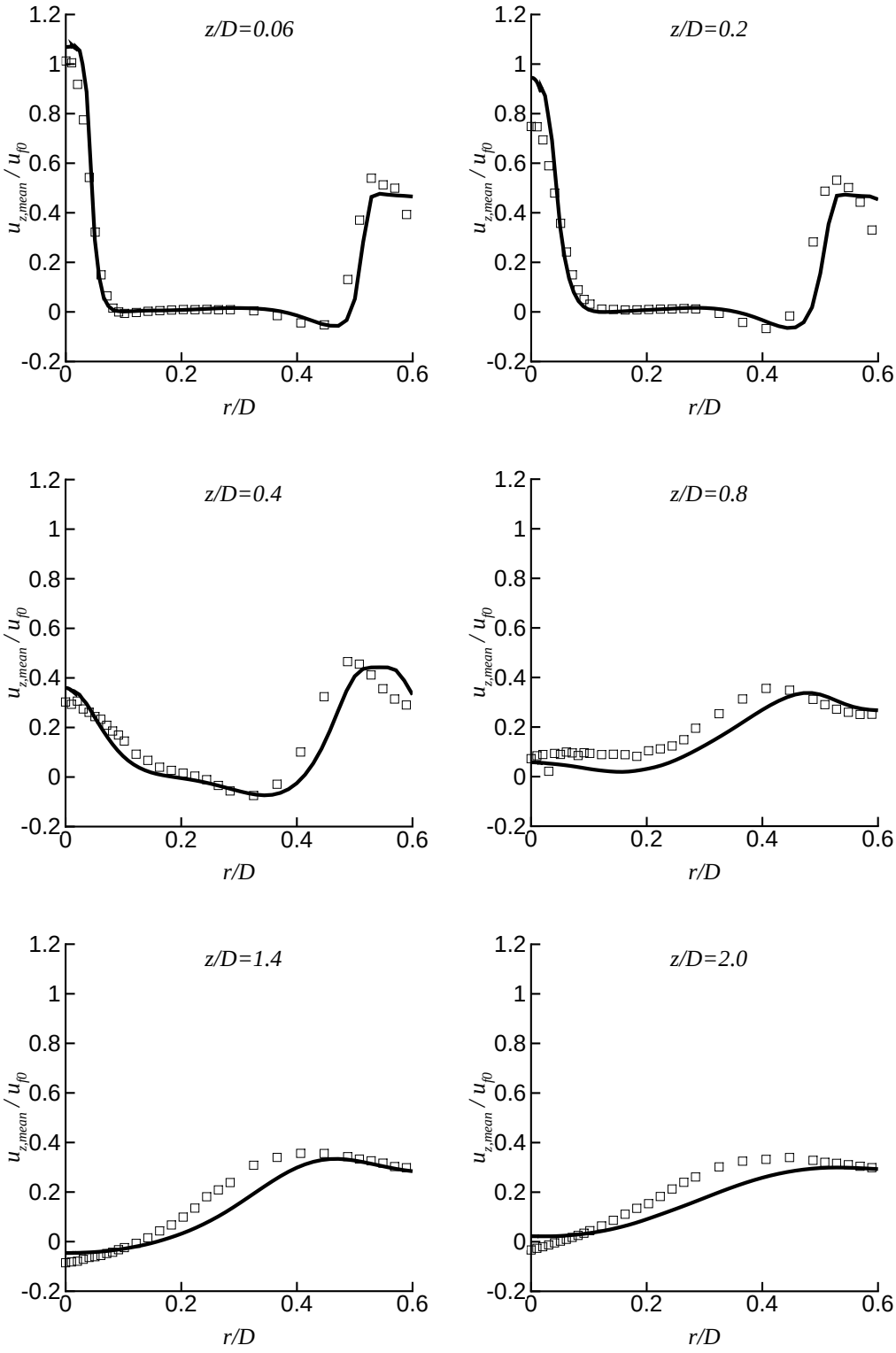

Figure 3.26: Mean axial velocity at different axial distances from the burner surface. The solid line is ILES and the square marks are experiment [60]

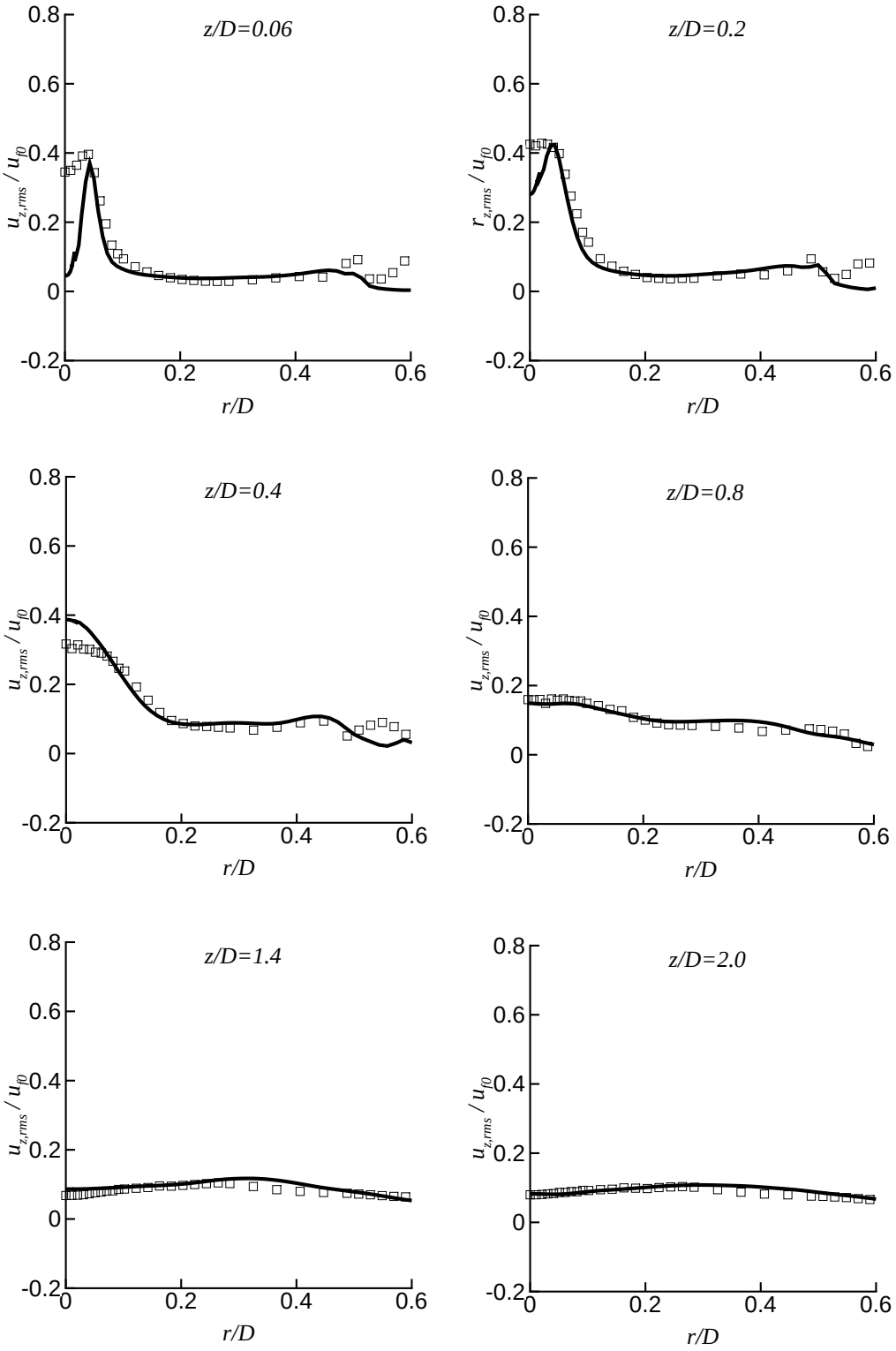

Figure 3.27: Rms axial velocity fluctuation at different axial distances from the burner surface. The solid line is ILES and the square marks are experiment [60]

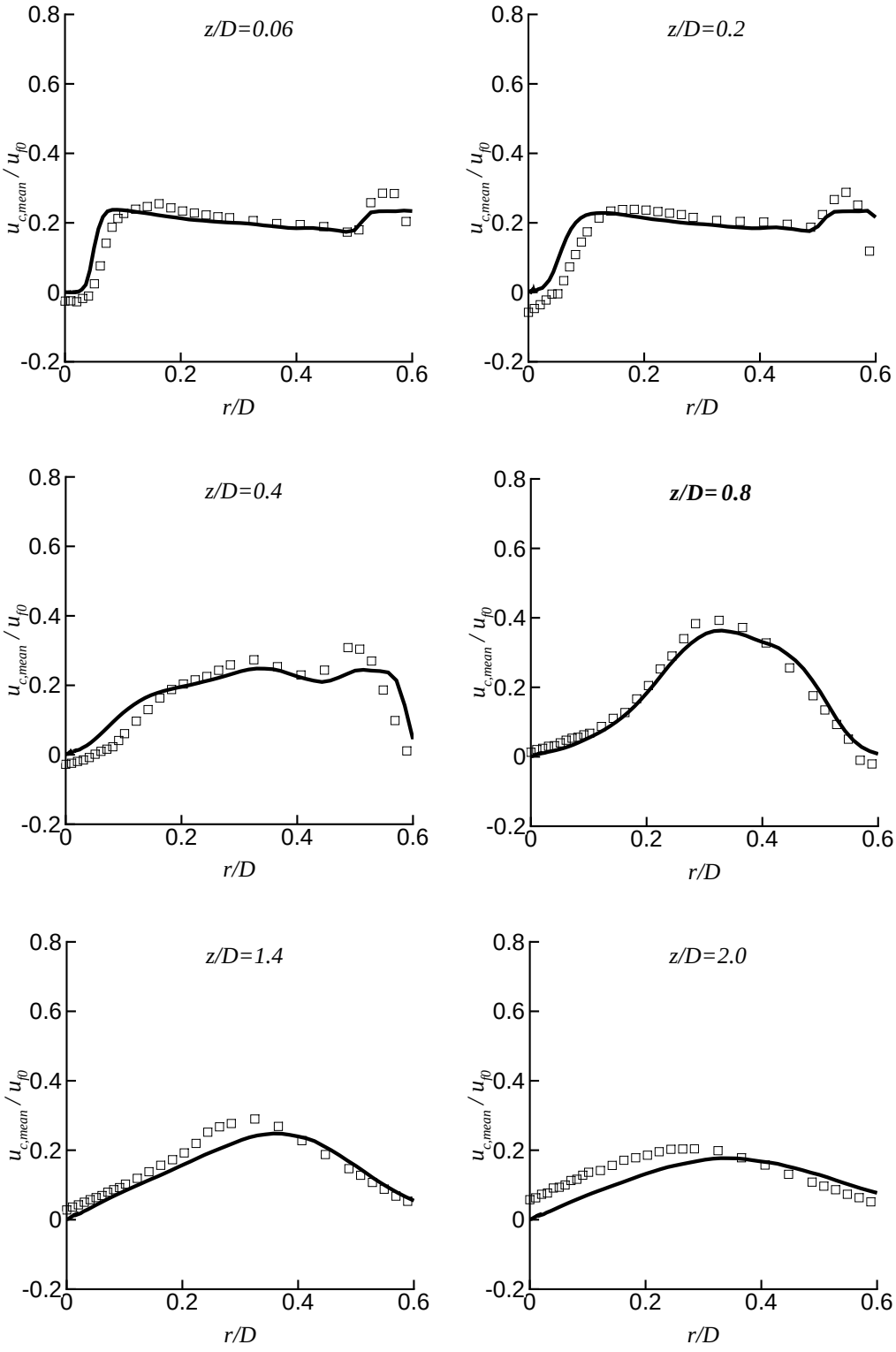

Figure 3.28: Mean circumferential velocity at different axial distances from the burner surface. The solid line is ILES and the square marks are experiment [60]

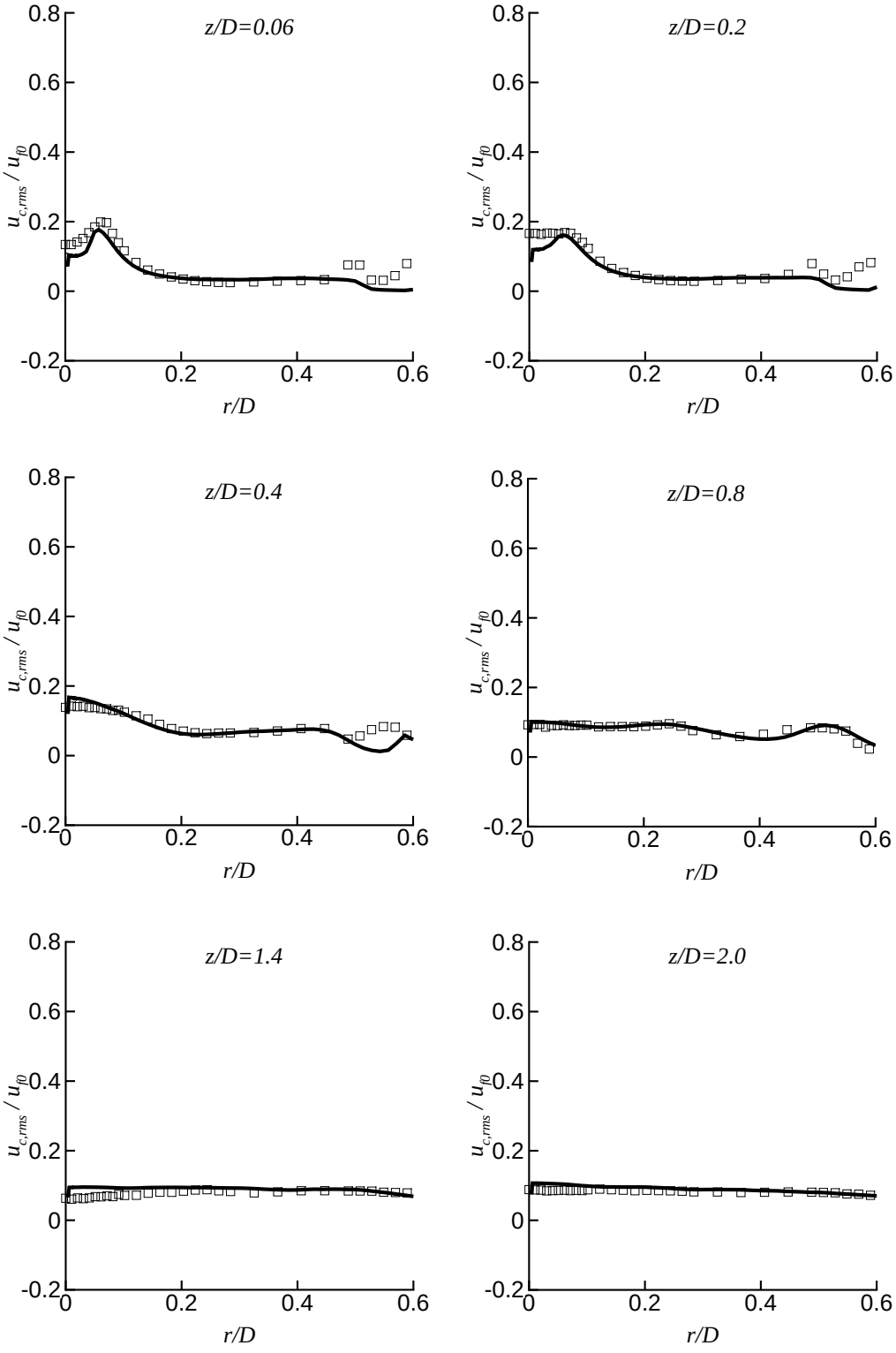

Figure 3.29: Rms circumferential velocity fluctuation at different axial distances from the burner surface. The solid line is ILES and the square marks are experiment [60]

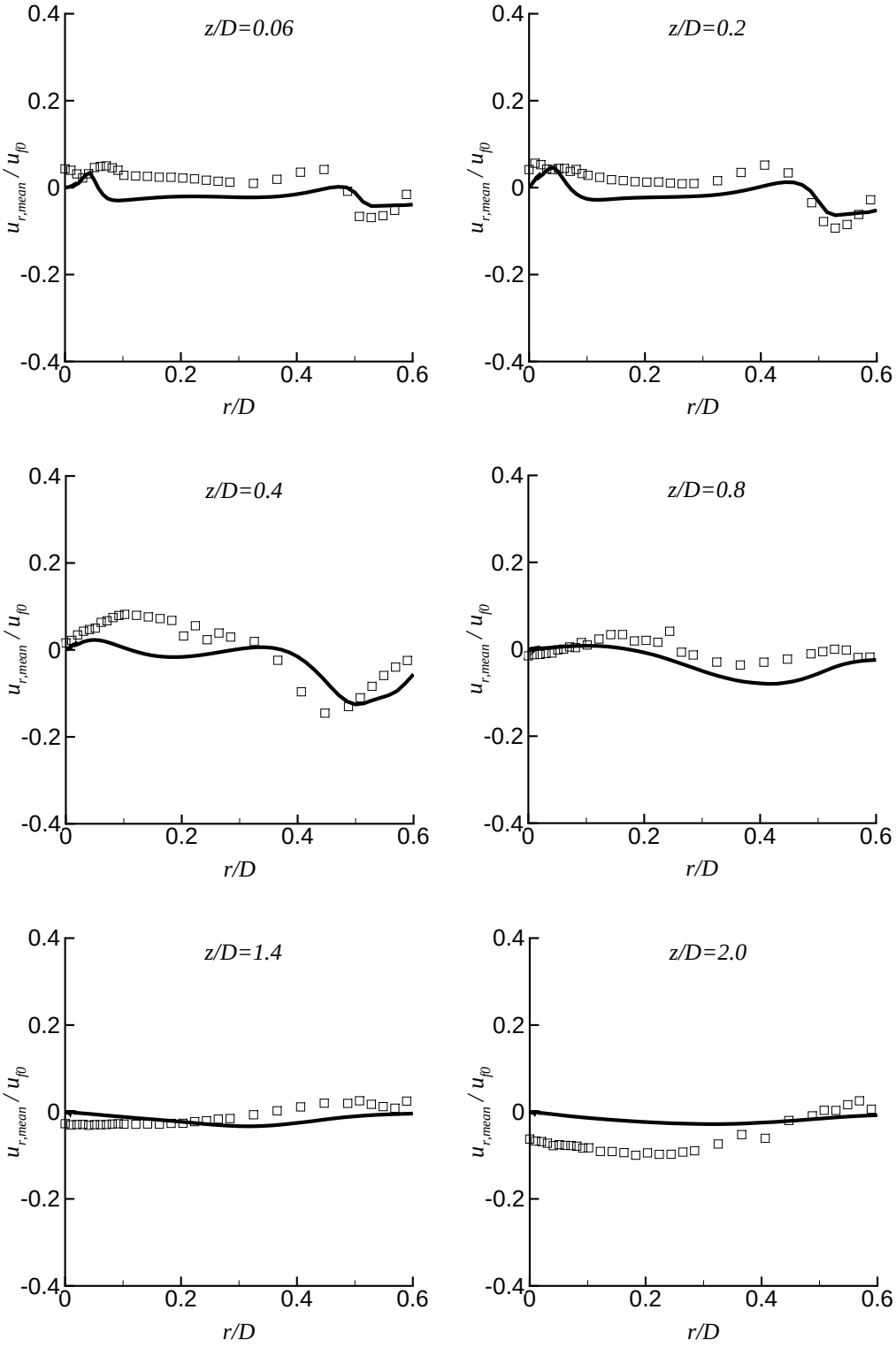

Figure 3.30: Mean radial velocity at different axial distances from the burner surface. The solid line is ILES and the square marks are experiment [60]

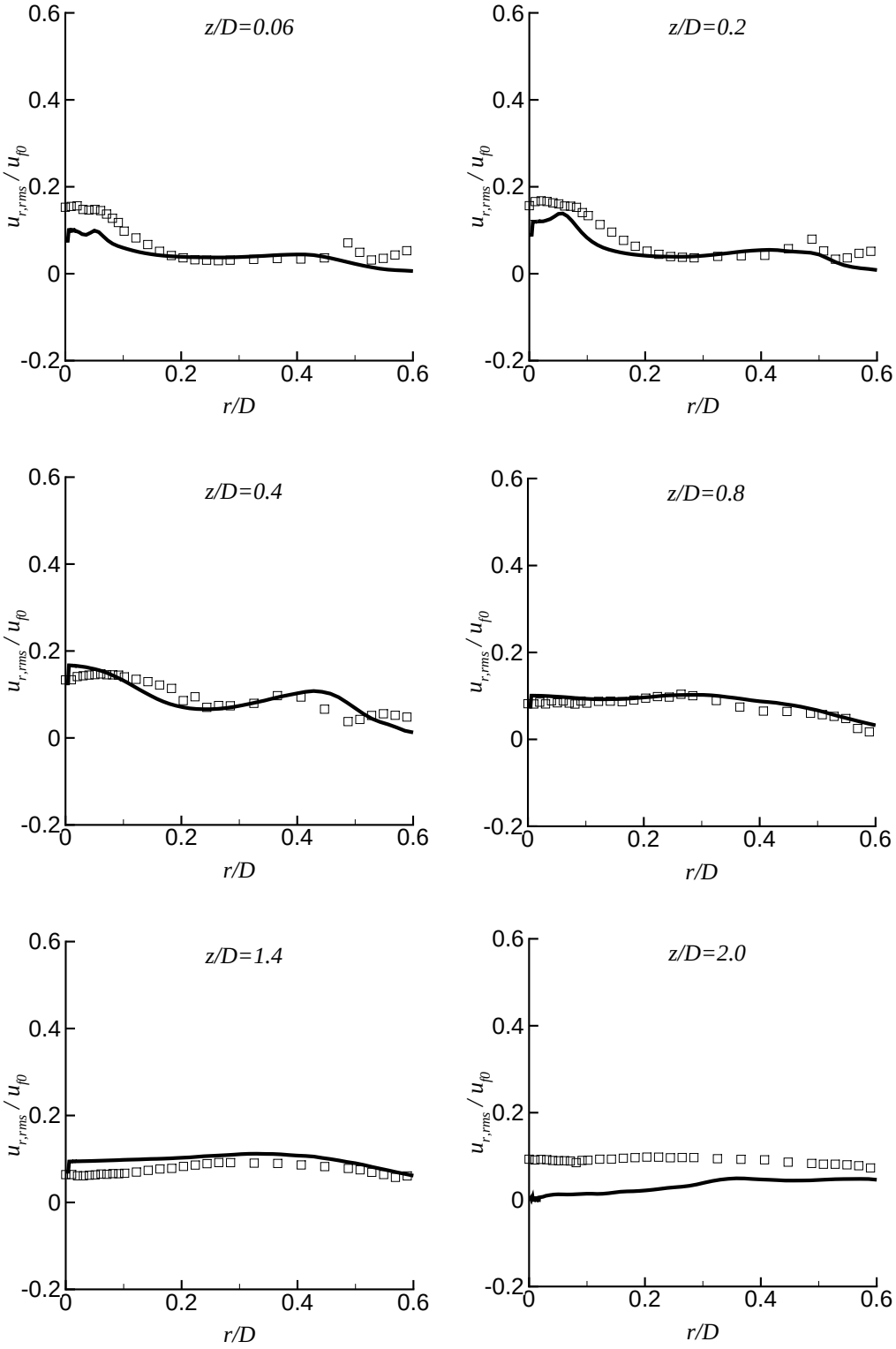

Figure 3.31: Rms radial velocity fluctuation at different axial distances from the burner surface. The solid line is ILES and the square marks are experiment [60]

3.7.3 Swirl Effects

Figure 3.32 shows the mean axial, radial and circumferential velocity profiles of the three different swirl number flows at a constant distance from the bluff body plate, $z/D = 0.4$. The profiles are compared with experimental data by [59]. Note that air is selected as the central fuel jet corresponding to the experimental data. The velocities are normalised by the fuel inlet velocity u_{f0} for each case. In general, the ILES computation results show good agreement with experimental data.

In the axial velocity profile, a discrepancy from experimental data can be seen in the near central region for the non-swirl case while a good agreement can be observed for the low and high swirl cases. The reason for this discrepancy is due to a large change of axial velocity within a small distance at around $z/D = 0.4$ for non-swirl case where high turbulent intensity can be observed (see Figure 3.7).

In the radial velocity profile, experiments show a larger positive velocity at $0.1 < z/D < 0.3$ and a larger negative velocity at $0.35 < z/D < 0.45$ for the low swirl case. These regions have small axial velocity, indicating locations near to the top and bottom edge of the vortices. Since the velocity magnitude and direction at the edge of the vortices vary largely with the simulation inlet conditions, experimental measurement conditions etc, and hence substantial discrepancies can be seen in these regions. However, it should be noted that the absolute values of the radial velocity are small compared to the axial velocity.

In the circumferential velocity profile, simulation results well match to the experimental data. The small difference in the central region can be considered as a variation of the experimental data since ideally circumferential velocity should be zero at the centre line.

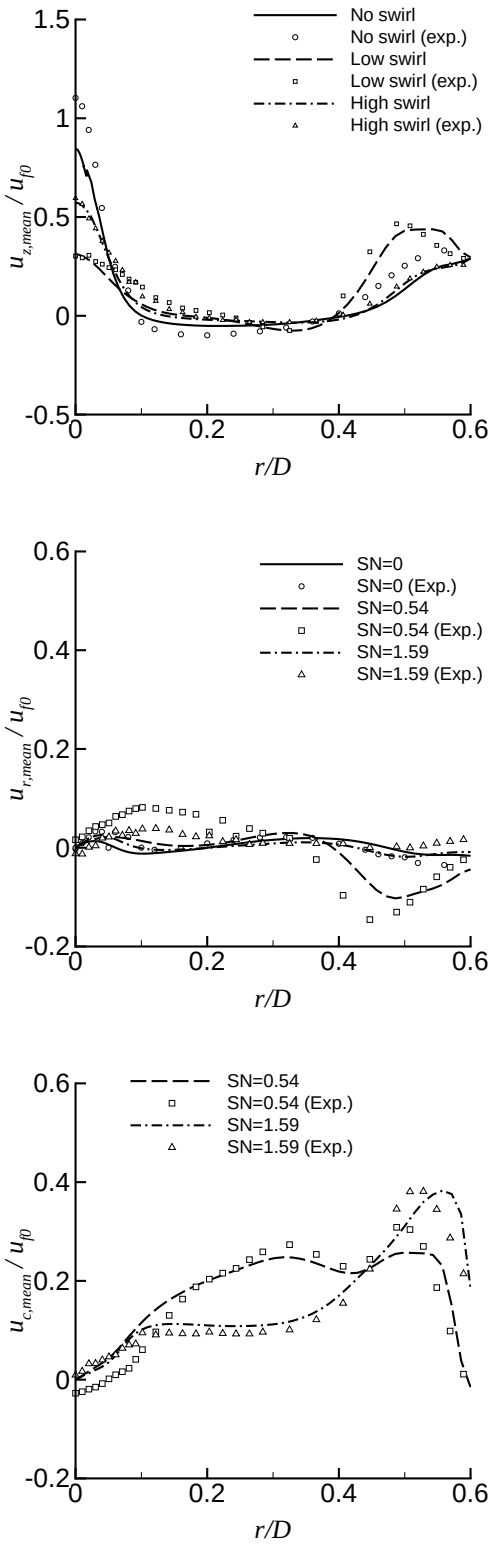

Figure 3.32: Mean velocity profile of three different swirl flows; axial (top), radial (middle) and circumferential (bottom) velocity

3.7.4 Density, Pressure and Viscosity Effects on the Flow Structure

In the previous subsections simulation have been performed with an air jet in order to compare the results to experimental data and to evaluate the accuracy of the simulated flow field. However, the density of actual fuel e.g., methane, is about 43% smaller than air and hence, the momentum of a methane jet is small compared to an air jet, which can result in a different structure of the flow field. Also, pressure and viscosity of the air inflow vary largely depending on the operational condition of the combustor. In this subsection, simulation results with a range of fuel density, air pressure and air viscosity are presented.

Figure 3.33 shows the streamlines and a volume fraction contour map of the central air jet of the non-swirl flow ($SN = 0$). An inner and an outer vortex can be observed in the streamlines at $0.02 < r/D < 0.2$ and at $0.15 < r/D < 0.5$, respectively. The inner vortex is collapsed since the momentum of the air jet is large. A large portion of the fuel jet penetrates to the downstream region ($z/D > 1.0$) without being involved in a recirculation zone. As a result, fuel (air) concentration spreads towards the axial direction. The volume fraction contour map shows that a downstream location, e.g., $(r/D, z/D) = (0.0, 1.5)$ still includes more than 10% of the jet species.

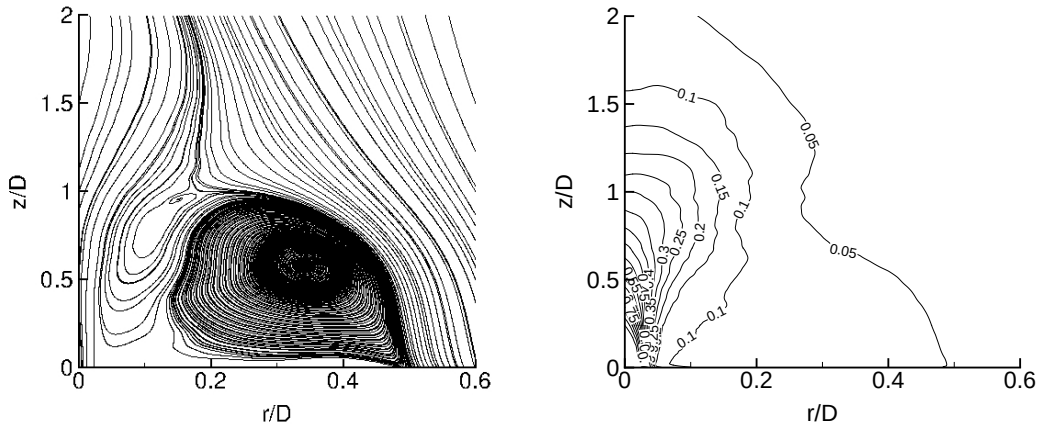

Figure 3.33: Temporally averaged streamlines (left) and volume fraction contour (right) of the air jet, non-swirl flow

Figure 3.34 shows the same simulation results but with a methane jet. A clear inner vortex can be observed in the streamlines since the methane jet momentum is small and hence, a large portion of the jet is entrained into the inner vortex. Regardless of this difference of the inner vortex structure the location of the outer vortex centre and the recirculation zone do not change largely. In contrast, the volume fraction contour map shows significant change. The fuel species does not spread towards the axial direction. The fuel volume fraction is reduced to 5% at the same downstream location $(r/D, z/D) = (0.0, 1.5)$. Furthermore, a flammable region which can be defined as a fuel-air mixture containing 5% to 15% of the fuel volume fraction, is shifted in the radial direction.

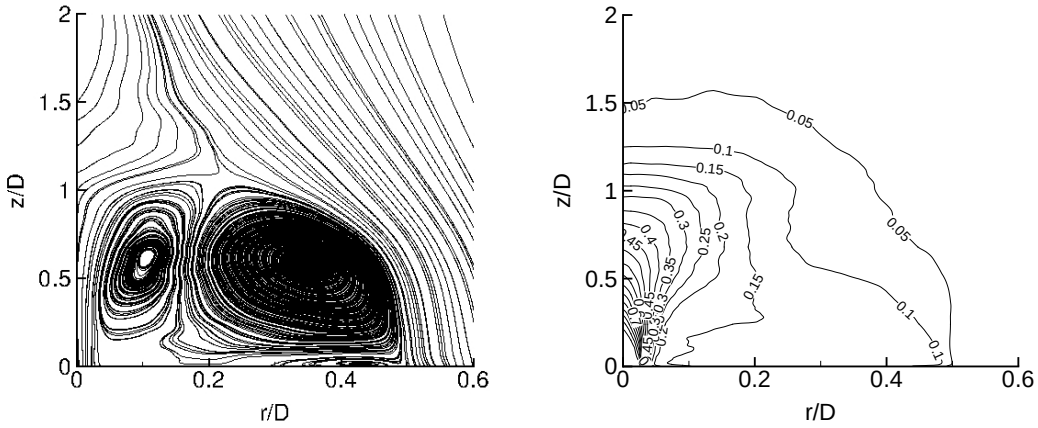

Figure 3.34: Temporally averaged streamline (left) and volume fraction contour (right) of the methane jet, non-swirl flow

The volume of flammable mixture V_{fl} is also essential for ignition of the fuel-air mixing flow, and hence V_{fl} is calculated from the mean volume fraction contour maps.

Figure 3.35 (top) shows the changes of V_{fl} with respect to Atwood number. The air jet case and the methane jet case correspond to $At = 0$ and $At = 0.288$, respectively. V_{fl} is normalised by a nominal volume of this injector geometry defined as $V_0 = 1/4\pi D^3$ which is close to the volume of the recirculation zone of a typical simulation case, e.g., shown in Figure 3.34. Although the mixing location changes as described above, V_{fl} shows only a slight difference with respect to At for all the non-swirl and swirl cases. It should be noted that V_{fl} is used as a mixing parameter and hence, the definition is corresponding to the flammability limit of the methane and air mixture, i.e., 5% to 15% of the methane volume fraction, however, the actual flammable fuel concentration ranges vary with fuel species.

The effects of ambient air pressure and viscosity are investigated in terms of the flammable volume. Figure 3.35 (middle) shows the results of the methane jet, low swirl flow. The curves describe an amount of the volume containing more than 5% fuel volume fraction and 15% fuel volume fraction, representing the lean and rich limits of the methane-air mixture flammability, respectively. Each curve shows 2% difference at most in the range of 0.1 to 1.0*atm* and hence, the flammability volume V_{fl} ($= V_{5\%} - V_{15\%}$) remains unchanged. Figure 3.35 (bottom) shows the air viscosity effect on the methane jet, low swirl flow. The volume of the lean and rich limit are depicted in terms of Reynolds number of the air inflow. With an increase of Reynolds number, which corresponds to decrease of kinematic viscosity coefficient of air, $V_{5\%}$ and $V_{15\%}$ increased similarly, and hence, V_{fl} does not change largely.

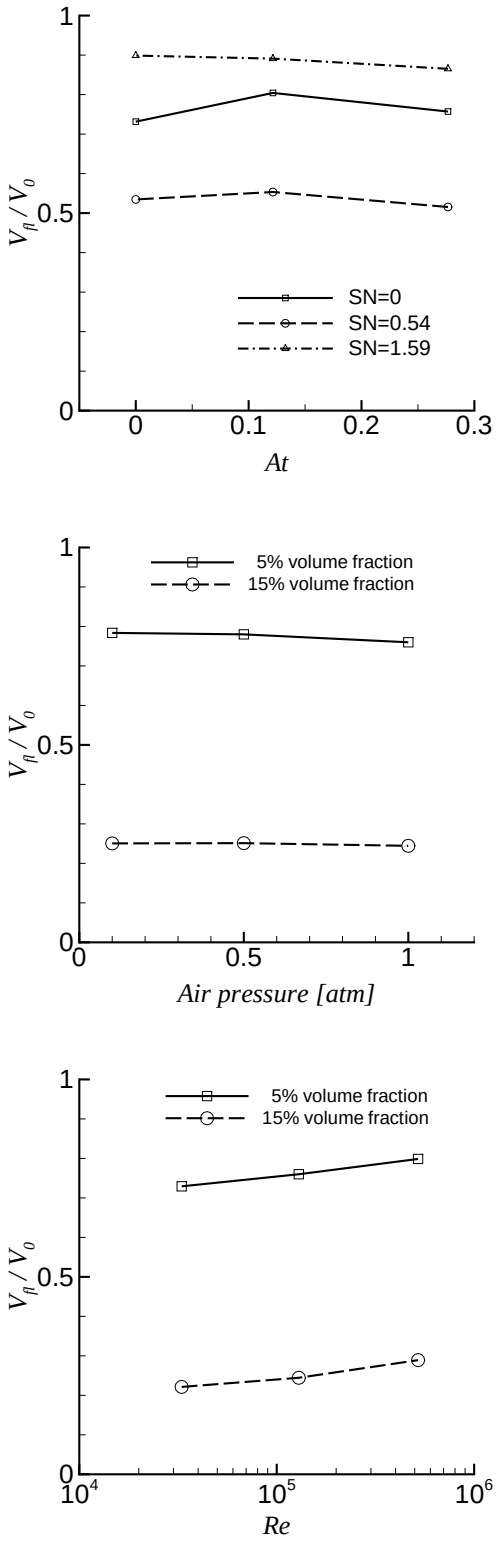

Figure 3.35: Pressure (top) and viscosity (bottom) effects on the flammable mixture volume

3.8 Summary

An ILES technique based on high-resolution and high-order methods was used to investigate a turbulent mixing flow generated by a generic geometry fuel jet burner flow. In the ILES simulation, a finite volume Godunov-type method was used with a high order limiter and an approximate Riemann solver. The governing equations for a compressible, single phase, multi-species, non reactive flow were solved without explicit modelling of the subgrid scales. The subgrid scale effect was accounted by the built-in characteristics of the high-resolution method. For low Mach number flow, the velocity components were modified in order to avoid excessive dissipation, which was shown by the leading order dissipation rate. Up to ninth-order spatial accuracy limiters were used with a third-order explicit Runge-Kutta method for time integration. All simulations were performed with 'Astral' computational cluster in High Performance Computing facility of Cranfield University featuring Intel 5160 Xenon dual-core processors. The computational sampling time to obtain a typical mean flow on the medium grid with the fifth-order limiter was about 1,570 hours.

Mean flows were obtained by averaging flow properties temporally and circumferentially. This was carefully done by the observation of convergence of the velocities. The results were compared with experimental data. The mean axial, radial velocity and rms velocity profiles showed good agreement in the strongly turbulent region, recirculation region and the downstream region of the flow fields. For multi-species flow simulation, methane jet injection into air was simulated with Allaire's mixing model in which volume fractions of species, instead of mass fractions were tracked. The axial and radial distribution of the mixture fraction demonstrated a good match to the experimental data.

The one dimensional kinetic energy spectrum was examined to evaluate the effects of grid resolution on energy dissipation with fifth order spatially accurate limiter. An ideal $k^{-5/3}$ decay of energy could be seen in a certain range for all test cases and the range increased with grid resolution. The cut-off wavenumbers where the energy spectrum curve begins to detach from the $k^{-5/3}$ line were larger than the estimated maximum wavenumbers appearing on the given computational grid. This implies that the numerical dissipation accounted for the energy transportation between large and small eddies sufficiently up to the effective cut-off.

In the same manner the second, fifth and ninth-order limiters were examined on the medium grid in order to investigate the effects of order of accuracy. The simulations were carried out with a 0.6 million point grid. The results showed that the fifth-order limiter achieved good resolution of the kinetic energy dissipation with reasonable computational time compared to the second-order limiter. The ninth-order limiter required substantially larger computational power.

In order to investigate complex flow mechanisms of the bluff body burner, simulations were performed on different density fuel jet flows with corresponding Atwood numbers from 0 to 0.871. The simulations were carried out with a 0.6 million point grid.

The flow field included a recirculation zone containing an inner and an outer vortex. Temporally and spatially averaged mean streamlines and velocity contours showed that with an identical momentum flux of the fuel jets, the flow structure and velocity field were unchanged by Atwood number, except for the central fuel jet region. At the centre axis, the velocity decay rate increased monotonically with the increase of Atwood number, which resulted in the same velocity profile at further downstream. The volume fraction field changed due to the variation of injected fuel volume into the domain, however, a large, constant fuel volume fraction region was formed for all test cases. The fuel volume fraction in this region was controlled by species mixing at a point where fuel and air stream collided. This point is located at the top edge of the recirculation zone, and a large rms volume fraction was observed for all test cases. A mixing parameter which was originally introduced for investigations of species molecular mixing in a mixing layer was applied to the complex turbulent flow. It was revealed that the degree of molecular mixing decreased at the mixing point with the increase of Atwood number. The simulation results showed that this feature of the mixing field and the effects of Atwood number can be described with this parameter.

The effect of swirl on the same jet flows was investigated, as well as flow structure changes due to fluid property, i.e., density, pressure and viscosity. This investigation is based on jet engine operation under a wide range of air conditions. Simulations were performed with the fifth order spatial accurate limiter and with 0.6 million points for three different swirl number flows. A detailed observation of the flow field showed that the ILES simulation captured the swirl flow structure well, including the size and location of recirculation zones. Mean and rms fluctuation velocities in the axial, radial and circumferential direction well agreed with experimental measurements. Density effects were examined by changing the fuel species. The results showed that the shape of the inner vortex in the recirculation zone changed while the outer vortex and the area of recirculation zone remained unchanged. A significant change was observed in the volume fraction contour map, however, the flammable mixture containing near stoichiometric air and fuel did not change. Also, pressure and viscosity effects were examined in the same way and the results showed the flammable volume did not change regardless of the change of flow structure.

CHAPTER 4

ILES of Combustion Flows

4.1 Introduction

Nonpremixed flames can be observed in all types of combustors, from laboratory burners to large scale plant gas turbines, and from spark ignition type engines to flame holding jet engines. A major reason of this is that flame positions and energy releases can be controlled relatively easily by fuel and air supply systems compared to premixed flames configurations, which ensures safe operation of the industrial combustors. However, turbulence coupled with flames makes the combustion phenomena more complicated. This is because turbulence changes the flame structure and enhances chemical reaction while temperature increase by combustion induces gas expansion and instability, which results in increase of turbulence. Therefore, understanding of turbulent nonpremixed combustion, particularly the interaction of chemical reactions with turbulence, has been one of the main topics of the combustion research. Since the phenomena is essentially time dependant and takes place at small length scale, experimental measurements have had limitations to provide accurate information, and therefore, numerical research has been encouraged and widely conducted.

In most of the recent computational work on turbulent nonpremixed flames, e.g., in extensive research of the TNF, summarised in [8], flow field have been solved using the LES approach ([48], [88], [87], [74], [54]). This is because LES can provide instantaneous information of the flow field which is required for precise turbulent flow analysis and hence, it has been recognised as a more promising approach as opposed to RANS. In these conventional LES research filtered governing equations have solved together with a subgrid scale model. As a turbulence model, a Smagorinsky type model with flow dependent coefficients has been typically applied to the subgrid stress term in momentum equation. In the LES including chemical reactions, unknown scalar transport terms also appear in species and energy equations as a result of filtering operation. These terms need to be modelled and a gradient transport assumption together with turbulent Schmidt number has been typically used.

However, the LES approach contains some drawbacks. The essential argument is in commutation between filtered and differentiated variables which is the basic assumption of the conventional LES. As described in [18] this assumption does not hold true

with a variable filter width. Other issues can be induced by explicit descriptions of subgrid scale modelling. For example, even with dynamic procedure for the Reynolds stress term proposed by [28] which enables to avoid manual tuning of the model coefficients, using a universal turbulent model is still arguable. Also, the gradient transport model was pointed out in [69] to be inappropriate for the combustion flow though it has been employed generally due to its simplicity.

ILES techniques, (see reviews [36], [56], [18]), in conjunction with high-resolution methods, described in [22] and [93], has been developed to overcome the disadvantages of the conventional LES approach. In ILES computations it is assumed that the numerical discretisation itself accounts for unresolved scales, in other words implicitly modelling the subgrid scales. Since explicit filtering operation for determination of subgrid scale is not required, the governing equations do not include unknown terms, and therefore, no subgrid scale modelling for the Reynolds stress term and scalar transport terms is necessary.

A major challenge for combustion flow can be a description of the chemical source term. This corresponds to suppose how to account for the contribution of unresolved scale turbulence to the chemical source term. These effects have not been well investigated in the ILES methods. Therefore, applying of a non filtered, simple chemical source term and analysing of the results can be a good starting point as an ILES of combustion flow.

This chapter concerns ILES of turbulent nonpremixed methane flames using a computational fluid dynamics code which has incorporated high-resolution Godunov-type methods. First, fundamental governing equations for turbulent combustion flow and transport properties used in the simulation will be described. The chemical source term with which the turbulent flow and chemistry is coupled and selected chemical reactions are also described. Next, simulation test cases and the governing equations for ILES with a finite rate chemical reaction approach will be introduced. Simulation of a simple one dimensional premixed methane flame propagation, and a two dimensional mixing layer will be presented. The effects of combustion modelling of this approach will be analysed focusing on the chemical reaction rate. Simulation test cases with an infinitely fast chemical reaction approach will then be presented. This model can be considered as the opposite end of the finite rate chemistry approach in terms of turbulence and chemical reaction interaction. In this model chemical reaction takes places instantaneously. The turbulent flow time scale is threfore much longer than the chemical reaction time scale. This is a simple method and can be easily combined to ILES turbulent computation. The results will be shown and analysed focusing on flow field and scalar field.

4.2 Turbulent Combustion Flows

4.2.1 Influence of Turbulence

Several combustion properties are affected by the turbulent motion. In premixed flame configuration, where fuel and oxidiser is mixed before ignition and the species composition of the mixture is uniform in everywhere, flame speed and flame thickness are of importance to characterise the flame. The flame speed depends on the fuel and air ratio, the highest value can be obtained around stoichiometric condition. It has been known that when the turbulence intensity of the unburnt gas is high the flame propagation speed increases, which results in short time of combustion and fast consumption of fuel. It implies that the turbulent flame speed S_T is larger than laminar flame speed S_L. These properties can be related as [71]:

$$\frac{S_T}{S_L} \approx 1 + \frac{u_{rms}}{S_L} \tag{4.2.1}$$

where u_{rms} is the rms of the velocity fluctuations. This equation shows that the flame propagation speed is increased by fluctuating velocity, i.e., turbulent motions. Also, it implies that when u_{rms} is large, the turbulent flame speed S_T can be close to u_{rms} and independent of the laminar flame speed. Regarding the flame thickness, turbulent flame has larger thickness than the laminar flame.

The interaction between turbulence can be expressed by the time scale ratio of flow mixing τ_m and chemical reaction τ_r, i.e., Damköhler number:

$$Da = \frac{\tau_m}{\tau_r} \tag{4.2.2}$$

These time scales can be estimated typically as:

$$\tau_m = \frac{l_t}{u_{rms}} \tag{4.2.3}$$

$$\tau_r = \frac{\delta_0}{S_L} \tag{4.2.4}$$

When $Da << 1$, species mixing takes place in a short time compared to chemical reaction, and flames are ‘thickened’ as schematically shown in Figure 4.1. Oppositely, chemical reaction occurs in a short time compared to the turbulent mixing when $Da >> 1$. In this case, flames are very thin and ‘wrinkled’. The flame structure is unaffected by turbulence and therefore, can be considered similar to laminar flame. Assuming that combustion flows of the bluff body burner has similar flow structures to the non reactive flow examined in the previous chapter, i.e., the large eddies and rms velocity are in the same order, the typical Damköhler number was obtained 0.06.

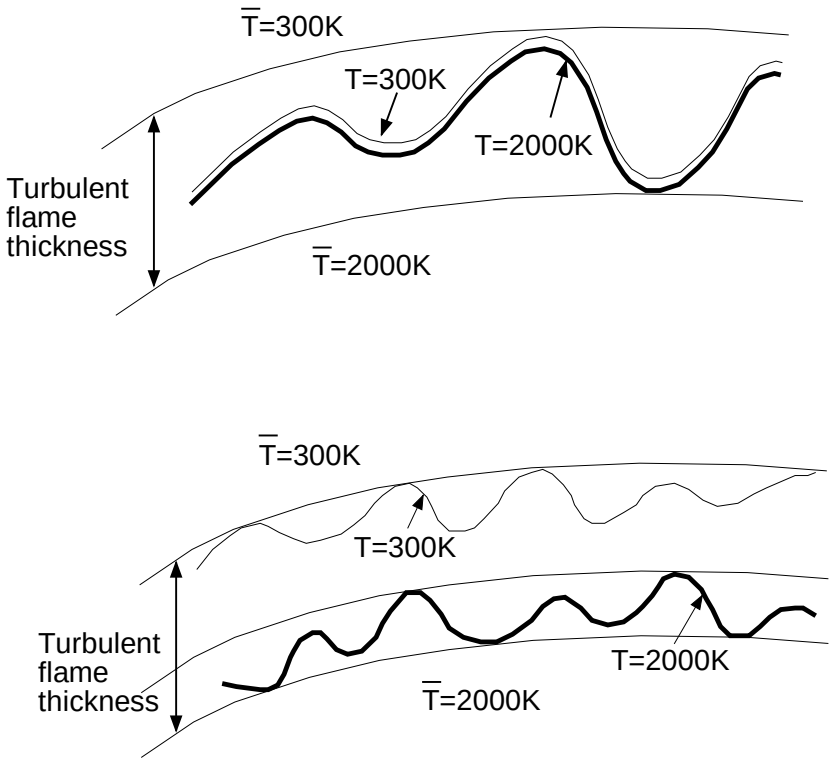

Figure 4.1: Schematic of wrinkled flame ($Da >> 1$) (top) and thickened flame ($Da << 1$) (bottom), after [71]

In nonpremixed flame configuration, where fuel and air meet in the domain, mix and ignite, flame does not propagate. Flame speed cannot express combustion characteristics, instead, flame geometry, i.e., flame position, flame length and transition from laminar to turbulent characterise flames. This implies that the mixing and scalar dissipation is of importance, Flame length can be measured experimentally as schematically shown in Figure 4.2. The flame length increase with the fuel velocity (with the increase of momentum) and after reaches to a certain length it decreases. The transition of the jet to turbulent flow occurs in a high velocity range. Under high fuel velocity conditions, the flames detach from the nozzle and finally blow-off. It should be noted that the chemical reaction rate is increased by the turbulence since fuel velocity increased but the flame length is constant.

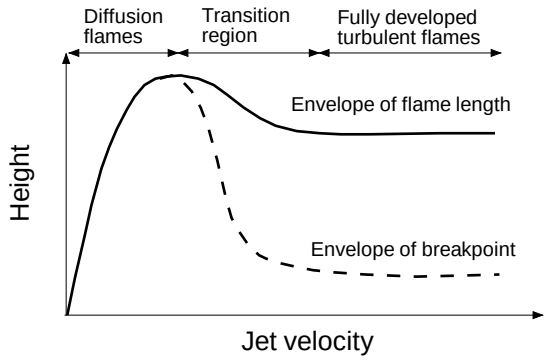

Figure 4.2: Schematic of nonpremixed flame length variation against fuel jet velocity, after [40]

4.2.2 Experimental Research

In combustion flow experiments, premixed flame sheet has been measured and analysed as one dimensional test case, e.g., [9]. These data can be used as benchmark of combustion flow simulations. A planer counter flow flame has also been often investigated e.g., in [14] since not only the flame structure can be analysed as a two dimensional laminar flame but also the acquired data can be provided to look-up tables for turbulent flames computation. As more complicated three dimensional test cases, burner flames of nonpremixed fuel and air jets have been widely investigated. Particularly in the framework of TNF, simple geometry but complex flame shape burners were selected and measured experimental data were provided. Among them the same test case geometry as considered in the previous chapter was extensively investigated experimentally [15, 16, 59, 62], an example of measurements is shown in Figure 4.3. They measured three direction velocity components and their fluctuations by Laser Doppler Velocimetry technique. Also, species mass fractions were measured by Laser Raman Scattering technique. However, these measurements have been done separately.

NOx measurement is another interest in the experimental research. This is because the NOx production time scale is much longer than other chemical reactions. The inlet boundary condition measurements are still difficult as the same as the non reactive flows. In some measurements of these flames, the influence of swirl intensity on flame stability and an extinction of the flame were shown by compositional measurements [3, 61], The effects of inflow conditions on NOx production can be found, for exam-

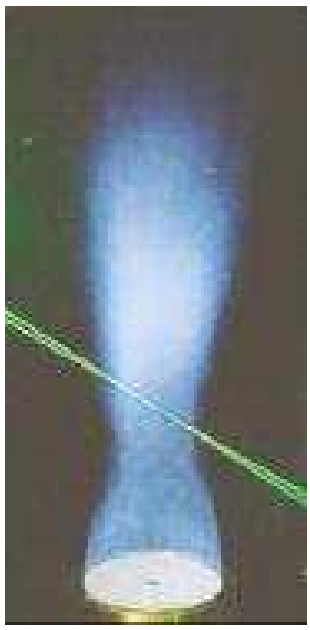

Figure 4.3: Combustion flow measurement of the 'Sydney bluff body burner' [62]

ple, in [13]. Regarding turbulence and acoustic wave interaction, the location of the strong precessing vortex and maximum pressure oscillations are reported to be largely different from a non reactive flow [80], which implies the constant pressure assumption applied in incompressible numerical simulations may reduce accuracy in these regions.

4.2.3 Instantaneous and Filtered Equations

Instantaneous combustion Flow

The compressible flow conservation laws for species, momentum and energy are considered. Fully compressible formulations have an advantage to enable to capture the interaction between flame and acoustics. A typical disadvantage of the use of compressible flow is the computational cost, however, the time step is often limited by the chemical reaction rate, and not by acoustic wave propagation, hence the fully compressible formulation does not induce additional cost for many cases [71].

An instantaneous pressure equilibrium assumption is applied in which each species in the mixture have the same velocity and pressure within a single volume cell. This leads to only one momentum equation for the mixture. Then, the momentum equation can be the same as applied in the non reactive flow simulation:

$$\frac{\partial \rho \mathbf{u}}{\partial t} + \nabla \cdot (\rho \mathbf{u}\mathbf{u}) = -\nabla \cdot \mathbf{P} \tag{4.2.5}$$

where $\mathbf{u}$ and ρ are the velocity vector and density, respectively. The stress tensor $\mathbf{P}$ contains pressure and viscous effect:

$$\mathbf{P} = p\mathbf{I} + \frac{2}{3}\mu(\nabla\cdot\mathbf{u})\mathbf{I} - \mu((\nabla\mathbf{u}) + (\nabla\mathbf{u})^T) \tag{4.2.6}$$

where p, $\mathbf{I}$ and μ, stand for pressure, unit tensor and dynamic viscosity coefficient, respectively.

Each species mass is conserved. For the mass diffusion term, the Hirschfelder and Curtiss approximation is applied:

$$u_{d,k} = -D_k \frac{\nabla X_k}{X_k} \tag{4.2.7}$$

where $u_{d,k}$, D_k and X_k stand for diffusion velocity, diffusion coefficient to the mixture, and mole fraction of species k, respectively. Then, using the relation between mole fraction and mass fraction:

$$X_k = \frac{W_k}{W_m} Y_k \tag{4.2.8}$$

where W_k, W_m and Y_k denote molecular weight of species k, mean molecular weight of the mixture, and mass fraction of species k, respectively. The species mass conservation equation yields:

$$\frac{\partial \rho Y_k}{\partial t} + \nabla\cdot(\rho\mathbf{u}Y_k) = \nabla\cdot\left(\rho D_k \frac{W_k}{W_m}\nabla X_k\right) + \dot{\omega}_k \tag{4.2.9}$$

where $\dot{\omega}$ is the chemical source term. With this species mass conservation equation, all N species appeared in the chemical reaction scheme are tracked. The continuity equation used in the non reactive flow is not required, instead, the total species mass should be conserved:

$$\sum_{k=1}^{N} Y_k = 1 \tag{4.2.10}$$

This means $N+1$ equations are set for N species mass conservation. In order to ensure total mass conservation with the Hirschfelder and Curtiss approximation, an option is sometimes taken in which only $N-1$ species are solved and the sum of their mass fraction is subtracted from unity for the rest species. This method is suitable for the diluted gas system, e.g., air or gases with nitrogen occupying a large portion, however, not appropriate for pure methane and oxygen gas system. For these cases, another option is commonly taken in which the correction velocity $\mathbf{u_c}$ is evaluated instead of solving a global mass conservation equation (see [71]):

$$\mathbf{u_c} = \mathbf{u} + \sum_{k=1}^{N} D_k \frac{W_k}{W}\nabla X_k \tag{4.2.11}$$

Then, the species equation for N species yields:

$$\frac{\partial \rho Y_k}{\partial t} + \nabla\cdot(\rho \mathbf{u_c} Y_k) = \nabla\cdot\left(\rho D_k \frac{W_k}{W_m}\nabla X_k\right) + \dot{\omega}_k \tag{4.2.12}$$

The energy equation has various forms. In the current research total energy E which is a sum of internal energy, kinetic energy and formation enthalpy is tracked. In this formulation, the total energy of the mixture does not change by chemical reaction, and therefore, chemical source terms do not appear in the energy equation:

$$\frac{\partial \rho E}{\partial t} + \nabla\cdot(\rho E \mathbf{u}) = -\nabla\cdot(\mathbf{P}\cdot\mathbf{u}) - \nabla\cdot\mathbf{q} \tag{4.2.13}$$

The enthalpy flux $\mathbf{q}$ includes a heat diffusion term and a species mass diffusion term:

$$\mathbf{q} = \kappa\nabla T - \rho\sum_{k=1}^{N}\left(\rho D_k h_k \frac{W_k}{W_m}\nabla X_k\right) \tag{4.2.14}$$

where κ, T and h are respectively thermal conductivity, temperature and a total enthalpy which includes formation enthalpy and is calculated by a combustion database, [83]. The mass diffusion velocity is also approximated by the Hirschfelder and Curtiss assumption.

To close the system, a perfect gas equation of state is applied:

$$p = \rho C_v(\gamma - 1)T \tag{4.2.15}$$

where C_v and γ represent the specific heat for constant volume and specific heat ratio, also calculated by a combustion database, [83].

Transport Properties

In calculation of transport properties, species transport due to a temperature gradient and heat transport due to a gradient of species concentration, namely Soret and Dufour effects are neglected. The viscous coefficient is dependent of temperature and obtained by Sutherland's law:

$$\mu = \mu_{ref}\left(\frac{T}{T_{ref}}\right)^{3/2}\frac{T_{ref} + T_s}{T + T_s} \tag{4.2.16}$$

where μ_{ref}, T_{ref} and T_s respectively represent reference viscosity coefficient, reference temperature and Sutherland coefficient. These coefficients are those of air at $273.15K$, therefore, $\mu_{ref} = 1.716 \times 10^{-5} kg/m/s$, $T_{ref} = 273.15K$ and $T_s = 110.0K$, respectively. The thermal conductivity and the species diffusion coefficients are calculated with constant non dimensional numbers:

$$\kappa = \frac{\mu C_p}{Pr} \tag{4.2.17}$$

$$D_k = \frac{\mu}{\rho Pr Le_i} \tag{4.2.18}$$

where C_p is heat capacity for the constant pressure calculated by the combustion database, [83], Pr is Prandtl number 0.72, and Le_k is Lewis number that is constant value for each species k, proposed by [85] and shown in table 4.1.

Table 4.1: Species Lewis number for methane air flame

Species	CH_4	O_2	H_2O	CO_2	H_2	CO	N_2
Le_k	0.97	1.10	0.83	1.39	0.30	1.11	1.00

Filtered combustion Flow

A filtering operation of variables is required for conventional LES, and usually, a spatial filtering:

$$\tilde{f}(x) = \int f(x')g(x - x')dx' \tag{4.2.19}$$

is applied. With this filtering, the filtered equations for momentum (4.2.5), species (4.2.12), and energy (4.2.13) can be derived:

$$\frac{\partial \overline{\rho}\tilde{\mathbf{u}}}{\partial t} + \nabla \cdot (\overline{\rho}\tilde{\mathbf{u}}\tilde{\mathbf{u}}) = \nabla \cdot \left(\overline{\mathbf{P}} - \overline{\rho}(\widetilde{\mathbf{u}\mathbf{u}} - \tilde{\mathbf{u}}\tilde{\mathbf{u}}) \right) \tag{4.2.20}$$

$$\frac{\partial \overline{\rho}\tilde{Y}_k}{\partial t} + \nabla \cdot (\overline{\rho}\tilde{\mathbf{u}_\mathbf{c}}\tilde{Y}_k) = \nabla \cdot \left(\overline{\rho D_k} \frac{\overline{W_k}}{\overline{W_m}} \nabla \tilde{X}_k \right) - \nabla \cdot \overline{\rho}(\widetilde{\mathbf{u}Y_k} - \tilde{\mathbf{u}}\tilde{Y}_k) + \tilde{\dot{\omega}}_k \tag{4.2.21}$$

$$\frac{\partial \overline{\rho}\tilde{E}}{\partial t} + \nabla \cdot (\overline{\rho}\tilde{\mathbf{u}}\tilde{E}) = -\nabla \cdot (\overline{\mathbf{P}} \cdot \tilde{\mathbf{u}}) - \nabla \cdot \overline{\mathbf{q}} - \nabla \cdot \overline{\rho}(\widetilde{\mathbf{u}E} - \tilde{\mathbf{u}}\tilde{E}) \tag{4.2.22}$$

where viscous stress and enthalpy flux term are the same shape as equation (4.2.6) and (4.2.14), respectively.

A typical closure for these equations are, applying the Smagorinsky model [82] for the subgrid viscous stress (Equation (1.3.7), and applying a gradient model which is the same idea as Smagorinsky model to the scalar fluxes:

$$\widetilde{\mathbf{u}Y_k} - \tilde{\mathbf{u}}\tilde{Y}_k = -\frac{\nu_t}{S c_t} \nabla \tilde{Y}_k \tag{4.2.23}$$

$$\widetilde{\mathbf{u}E} - \tilde{\mathbf{u}}\tilde{E} = -\frac{\nu_t}{S c_t}\nabla\tilde{E} \tag{4.2.24}$$

where ν_t and $S c_t$ denote turbulent viscosity and turbulent Schmidt number.

4.2.4 The Chemical Source Term

To deal with the chemical source term appeared in Equation (4.2.21) is one of the major problem for combustion computation. The difficulty is that the term is highly nonlinear and therefore the filtered chemical source term cannot be easily expressed as other filtered variables. The dependancy of this term on subgrid distribution of species and temperature also needs to be considered because combustion takes place in the small scales.

In most nonpremixed combustion simulation, the flame thickness is modelled as infinitely thin or artificially thickened and then, with some more assumptions e.g., a constant pressure field and constant diffusion coefficients for all species, computations are separated to turbulent mixing and flame structure calculation. However, in order to investigate the combination of the high-order high-resolution ILES methods and chemical reactions, modelling of a direct representation of the chemical source term is adopted. With this approach, both premixed and nonpremixed combustion problems can be handled in the same computational code.

In this sub section, first introduces analytical solution of the chemical source term with a simplified premixed case. The LES filtered chemical source term will be then discussed.

One dimensional premixed flame propagation is considered as shown in Figure 4.4.

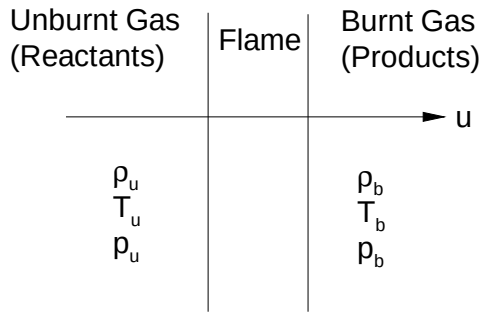

Figure 4.4: Schematic of one dimensional premixed flame propagation

A single step, irreversible chemical reaction is assumed. When the system contains N species, molecular number of reactants and products can be expressed as:

$$\sum_{k=1}^{N} \nu_k^R (Reactant)_k \Rightarrow \sum_{k=1}^{N} \nu_k^P (Product)_k \tag{4.2.25}$$

where ν_k is coefficient of molecular ratio under stoichiometric reaction of species k, and superscript R and P respectively designate reactants and products.

Then total mass should be conserved:

$$\sum_{k=1}^{N} \nu_k^R W_k = \sum_{k=1}^{N} \nu_k^P W_k \tag{4.2.26}$$

where W is molecular weight. Then, the reaction rate of species k of Equation (4.2.25) can be expressed as:

$$\begin{aligned} \dot{\omega}_k &= (Mass\,of\ species\,k\,in\,Reactant - Mass\,of\ species\,k\,in\,Product) \\ &\quad \times Progress\,Rate \\ &= W_k(\nu_k^R - \nu_k^P) K \prod_{k=1}^{N} [X_k]^{\nu_k^R} \end{aligned} \tag{4.2.27}$$

where K is the forward rate of reaction, often modelled by the Arrhenius law:

$$K = A_1 T^b exp\left(-\frac{E_a}{RT}\right) \tag{4.2.28}$$

where, A_1 and b are constants, E_a is an activation energy. If the reactants consist of only two species, namely fuel and oxidiser, the reaction rate can be written:

$$\dot{\omega}_f = W_f(\nu_f^R - \nu_f^P)\frac{\rho Y_o}{W_o}\frac{\rho Y_f}{W_f} A_1 T^b exp\left(-\frac{E_a}{RT}\right) \tag{4.2.29}$$

where subscript f and o denote fuel and oxidiser, respectively. When the reaction takes place at fuel lean condition, it can be roughly assumed that oxidiser mole concentration does not change through the reaction, therefore:

$$\nu_o^P = 0,\ \nu_o^R = 0,\ \nu_f^P = 0,\ \nu_f^R = 1 \tag{4.2.30}$$

and Equation (4.2.29) can be rewritten:

$$\dot{\omega}_f = A_2 T^b \rho Y_f exp\left(\frac{E_a}{RT}\right) \tag{4.2.31}$$

In order to evaluate the shape of the reaction rate, temperature, density and mass fraction will be normalised. For further handling of the chemical reactions and derivation of analytical solution, some assumptions are added.

- Each species molecular weight is the same, $W_k = W$
- Each species specific heat capacity of pressure is the same, $Cp_k = C_p$
- Each species diffusion coefficient is the same, $D_k = D$
- Steady state flow from flame position point of view, $\dfrac{\partial}{\partial t} = 0$

With these assumptions, the species diffusion term in Equation (4.2.14) due to the enthalpy difference is zero, and species Equation (4.2.12) and energy equation expressed with respect to temperature can be rewritten:

$$\rho_u u_u \frac{d\psi}{dx} = \frac{d}{dx}\left(\rho D \frac{d\psi}{dx}\right) + \frac{\dot{\omega}_f}{\psi_{f,u}} \tag{4.2.32}$$

$$\rho_u u_u \frac{d\theta}{dx} = \frac{d}{dx}\left(\frac{\lambda}{C_p}\frac{d\theta}{dx}\right) - \frac{\dot{\omega}_f}{\psi_{f,u}} \tag{4.2.33}$$

where subscript u designates unburnt gas condition. Two variables ψ and θ are, a normalised fuel mass fraction:

$$\psi = \frac{Y_f}{Y_{f,u}} \tag{4.2.34}$$

and a normalised temperature:

$$\theta = \frac{T - T_u}{T_b - T_u} \tag{4.2.35}$$

where subscript b denotes burnt gas condition. By adding Equation (4.2.32) and (4.2.33):

$$\theta + \psi = 1 \tag{4.2.36}$$

can be derived [71]. In premixed flame this relation holds true throughout the field while in nonpremixed flame this does not since mixing and combustion take places in the same timestep. Pressure can be regarded as constant throughout the flame, then density can be normalised by unburnt gas density:

$$\frac{\rho}{\rho_u} = \frac{T_u}{T} = \frac{1 - \alpha_T}{1 - \alpha_T(1 - \theta)} \tag{4.2.37}$$

where α_T is $(T_b - T_u)/T_b$. When the exponential of temperature b can be assumed zero, Equation (4.2.31) can be rewritten:

$$\frac{\dot{\omega}_f}{A_2 \rho_u Y_{f,u}} = \frac{1-\alpha_T}{1-\alpha_T(1-\theta)}(1-\theta) exp\left(-\beta_T \frac{1-\alpha_T(1-\theta)+\beta_T(1-\theta)}{1-\alpha_T(1-\theta)}\right) \quad (4.2.38)$$

where β_T is $(\alpha_T E_a)/(RT_b)$.

Figure 4.5 shows the right hand side of Equation (4.2.38), $f(\theta)$, with two typical value of α_T and β_T [71]. Note that the $\beta_T = 18.4$ case was normalised by its peak value, and that the $\beta_T = 8.0$ case was adjusted so that the sum of the reaction rate (occupied area in the graph) match to the same as $\beta_T = 18.4$ case, which implies both cases have the same flame speed. This figure describes that that the peak of the reaction can be seen at very close to the highest temperature and that the range of non zero reaction rate decreases with flame temperature increases. Therefore, an idea of separation of the field by non chemical reaction zone (with zero reaction rate) and chemical reaction zone (with non zero reaction rate) can be possible particularly for high temperature flow. With this separation, only the high temperature range (if its location can be detected) requires fine mesh in order to capture the flame structure properly.

While an instantaneous, laminar flame reaction rate shows a separation of reactive and non reactive flow field, a turbulent combustion flow can demonstrate non zero reaction rate for all range due to small scale turbulent features [71]. This is because fluctuation of the flow and spatially filtering of the computational method.

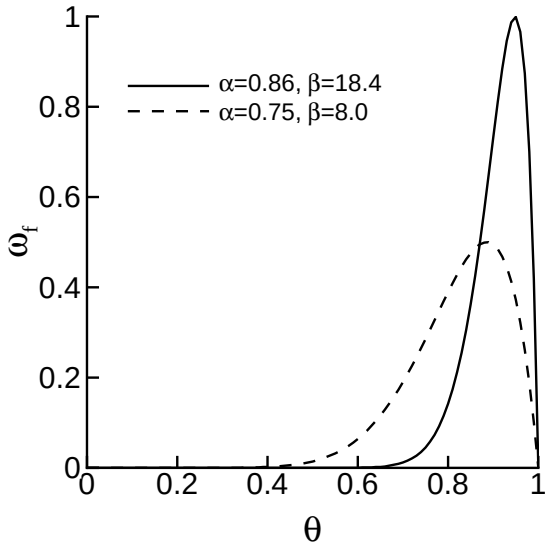

Figure 4.5: Analytical solution of the chemical source term, after [71]

Next, the LES filtered reaction rate appeared in Equation (4.2.21) is modelled with Arrhenius law.

When the fluctuation component is not considered, the reaction rate can be simply assumed from Equation (4.2.29):

$$\overline{\dot{\omega}}_f = A_3 \overline{\rho}^2 \tilde{Y}_o \tilde{Y}_f \tilde{T}^b exp\left(-\frac{E_a}{R\tilde{T}}\right) \tag{4.2.39}$$

This model however, consists of filtered turbulent flow variables. At the subgrid scale the chemical reaction is not accounted and only turbulent flow mixing occurs.

The subgrid effects can be considered by substitution of a decomposition of filtered and fluctuating variables, $\tilde{f} + f''$, into Equation (4.2.29) and Taylor expansion, yields [71]:

$$\overline{\dot{\omega}'}_f = A_3 \overline{\rho}^2 \tilde{Y}_o \tilde{Y}_f \tilde{T}^b exp\left(-\frac{E_a}{R\tilde{T}}\right)\left(\underbrace{1}_{(I)} + \underbrace{\frac{\widetilde{Y_f'' Y_o''}}{\tilde{Y}_f \tilde{Y}_o}}_{(II)} + g\left(\frac{E_a}{R\tilde{T}}\right)\left(\underbrace{\frac{\widetilde{Y_f'' T''}}{\tilde{Y}_f \tilde{T}}}_{(III)} + \underbrace{\frac{\widetilde{Y_o'' T''}}{\tilde{Y}_o \tilde{T}}}_{(IV)}\right) + ...\right) \tag{4.2.40}$$

where correlations of species and temperature fluctuations $\widetilde{Y_f'' Y_o''}$, $\widetilde{Y_f'' T''}$ and $\widetilde{Y_f'' T''}$ need to be modelled. The second term in the parenthesis expresses mixing of fuel and air in the subgrid scale, and the third and fourth terms accounts chemical reaction and mixing interaction in the subgrid scale. Therefore, in the subgrid scale:

- $\overline{\dot{\omega}'}_f$ does not account the interaction between turbulence and chemical reactions if only first term (I) of Equation (4.2.40) is considered. This is the same as Equation (4.2.39). The instantaneous mixing equilibrium condition is assumed, which means the time scale of turbulence is much smaller than that of chemical reactions.
- $\overline{\dot{\omega}'}_f$ does not account the interaction between turbulence and chemical reactions if even first two terms (I) and (II) of Equation (4.2.40) are considered. However, mixing speed is variable and the time scale of turbulence and combustion can be controlled.
- $\overline{\dot{\omega}'}_f$ accounts the interaction between turbulence and chemical reactions if first four terms (I) − (IV) of Equation (4.2.40) are considered.

Another approach was examined in the conventional LES research [25] in which filtered reaction rate was expressed with combining the terms (II) − (IV) in Equation (4.2.40) as:

$$\overline{\dot{\omega}'}_f = A_3 \overline{\rho}^2 \tilde{Y}_o \tilde{Y}_f \tilde{T}^b exp\left(-\frac{E_a}{R\tilde{T}}\right)(1 + \kappa_{SGS}) \tag{4.2.41}$$

where κ_{SGS} is a segregation factor and explicitly modelled based on partially stirred reactor model. In this model a small volume in a cell was assumed to be well reacted

and mixed, and the rest of the volume is not reacted. The segregation factor was estimated from the time scales of the subgrid scale:

$$1 + \kappa_{SGS} = \frac{\tau_{r,SGS}}{\tau_{r,SGS} + \tau_{m,SGS}} = \frac{1}{1 + Da_{SGS}} \tag{4.2.42}$$

where $\tau_{r,SGS}$, $\tau_{m,SGS}$ and Da_{SGS} represent respectively chemical reaction time, mixing time and Damköhler number in the subgrid scale. In Reference [25] $\tau_{r,SGS}$ was evaluated as a ratio of laminar flame speed and laminar flame thickness (Equation (4.2.4)) while $\tau_{m,SGS}$ is calculated from the Kolmogorov time scale and the subgrid time scale. With this model the simulation of the flow behind the triangular flame holder showed fair agreement with experimental data.

In premixed flame, Da_{SGS} can be written as [70]:

$$Da_{SGS} = \frac{S_L}{\delta_0} \frac{\Delta}{u'_{SGS}} \tag{4.2.43}$$

where u'_{SGS} is the characteristic subgrid velocity fluctuation. Assuming that turbulent kinetic energy follows Kolmogorov's $k^{-5/3}$ law (Equation(1.2.5)), and that wavenumbers are proportional to the inverse of the cell width Δ, u'_{SGS} can be expressed as:

$$u'_{SGS} = \left(\int_{k/2}^{k} E'(k) dk \right)^{1/2} = k^{-1/3} \propto \Delta^{1/3} \tag{4.2.44}$$

Therefore, Da_{SGS} is proportional to $\Delta^{2/3}$. When the cell width decreases to the Kolmogorov scale, $\Delta \to \eta_k$, eddies in all scales are accounted and the flow will be fully resolved. This leads to $Da_{SGS} \to 0$ and $\kappa_{SGS} \to 0$ from Equation (4.2.42), reproduces the unfiltered reaction rate as shown in Equation (4.2.29).

In methane air stoichiometric combustion case, with typical values $S_L = 0.4 m/s$ and $\delta_0 = 2.0 \times 10^{-3} m$, κ_{SGS} was evaluated as shown in Figure 4.6. From this graph, 15% discrepancy can be estimated when a grid with cell width $2.5 \times 10^{-5} m$ is used together with a simple chemical reaction model (Equation(4.2.39)) .

4.2.5 Chemical Reactions Scheme

The methane flame is the simplest case among hydrocarbon combustion, however, the detail process may involve tracking of some hundreds of species and some thousands of chemical reaction steps. A selected number of chemical reactions are usually solved in numerical simulation. For methane and air flames, a 'skeletal mechanism' [85] has been often used consisting of 35 elementary reactions and 15 reacting species. The reaction rates of these chemical species are given in the Arrhenius law. Further reduction of the number of reaction steps has been made to introduce global chemical reactions scheme. For example, four global reaction steps with tracking seven species [68], six

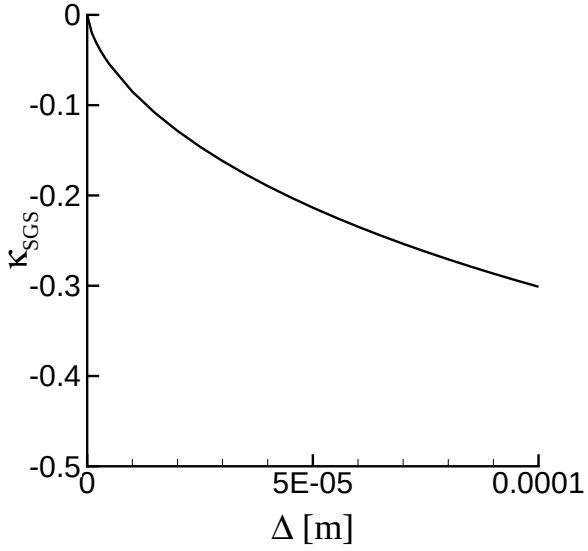

Figure 4.6: Variation of segregation factor

species [43] were proposed, and five global reaction steps including six species were developed in [24]. Those reduced reaction steps agreed well with skeletal elementary reactions scheme, with respect to mass fraction profile of premixed flames. Also, sensitivity analysis in which responses of the gas properties, e.g., density, velocity and mass fraction by change of elementary chemical reactions were examined and showed good matching between skeletal elementary schemes and reduced global reaction steps schemes [77]. A disadvantage of the reduced global steps reaction scheme might be a lack of tracking radicals, particularly *OH* radicals often used for comparison to experimental results.

In the current methane air flame simulation considering the balance of computational cost and accuracy of chemical reactions, reduced global steps reactions are applied. The simplest one step reaction is described as:

$$CH_4 + 2O_2 \Rightarrow CO_2 + 2H_2 \tag{4.2.45}$$

This is an irreversible reaction containing four chemical species. A reversible global four steps reaction scheme proposed by [43], including six species was also examined:

$$CH_4 + \frac{1}{2}O_2 \Rightarrow CO + 2H_2 \tag{4.2.46}$$

$$CH_4 + H_2O \Rightarrow CO + 3H_2 \tag{4.2.47}$$

$$H_2 + \frac{1}{2}O_2 \Rightarrow H_2O \tag{4.2.48}$$

$$CO + H_2O \Leftrightarrow CO_2 + H_2 \tag{4.2.49}$$

where simple Arrhenius type forward reaction rates of each step are obtained via [43] and the backward reaction rate of Equation (4.2.49) is from [58]. The advantage of this scheme is that it can track species H_2 and CO while in the fast chemistry approach which will be discussed in the later section only the one step reaction is available and these species are not tracked. The premixed flame speed of methane and other hydrocarbon fuels were examined using this scheme under various equivalent ratio, then both premixed and nonpremixed flame structure under lean, stoichiometric and rich condition were simulated with respect to species distribution and results showed good agreement with experimental data [43].

4.2.6 Mixture Fraction

A scalar variable, mixture fraction, is often used in analysis of nonpremixed flames since this scalar represents local species ratio of fuel and air. It is similar to the equivalent ratio which also describes a local species ratio and links to mass fraction of species and temperature, however, mixture fraction conserves before and after the chemical reaction.

First, element mass fractions, Z_i, which represents the ratio of the mass of an element i to the mass of the mixture contained in local space, are considered:

$$Z_i = \sum_{j=1}^{N} \xi_{ij} Y_j \tag{4.2.50}$$

where ξ_{ij} is mass ratio of molecule i to species j. The element mass fractions conserve between before and after chemical reactions, but can be changed only by flow mixing. Then, the mixture fraction can be defined as a variable linearly linked to the element mass fraction:

$$f = \frac{Z_i - Z_{i,air}}{Z_{i,fuel} - Z_{i,air}} \tag{4.2.51}$$

where, subscripts air and $fuel$ designate respectively air inflow stream and fuel inflow stream. Therefore, unless additional restrictions are given, mixture fraction can be available for flows in which only two streams, fuel and oxidiser, inflow to the domain separately (they are not premixed).

When a complete chemical reaction, for example Equation (4.2.45) is assumed, mixture fraction can be expressed with respect to mass fractions:

$$f = \frac{\nu Y_f - Y_{O2} + Y_{O2,air}}{\nu Y_{f,fuel} + Y_{O2,air}} \tag{4.2.52}$$

where ν is the mass ratio of fuel and air under stoichiometric condition, 4 for methane and air flame case. As seen in Equation (4.2.51) mixture fraction is a normalised values between 0 to 1: 0 for mixture containing only species originated from oxidiser inflow and 1 for mixture containing only species originated from fuel inflow.

4.3 Finite Rate Chemical Reaction Approach

The focus of this section is to examine a coupling of the ILES high-resolution method and a simple Arrhenius law chemical source term which corresponds to Equation (4.2.39). This model implies $\tau_r \gg \tau_m$ and $\kappa_{SGS} = 0$ in Equation (4.2.42).

4.3.1 ILES with Finite Rate Chemistry

Only selected papers have presented combustion flows with ILES technique. A main challenge is in the correlation of chemical reaction and turbulence in the subgrid scale. This is difficult for ILES since the subgrid scale model is not appeared in equations.

A compressible, nonpremixed mixing layer flame was simulated with ILES method [34]. Inviscid terms were solved by the second order spatial accurate ILES while viscous terms were solved by the central difference scheme. The subgrid stress and the subgrid scale scalar transport terms were considered to be built in the numerical method and therefore, no explicit subgrid scale modelling for these terms were given. For the chemical reaction source term, a one-step, irreversible reaction with the reaction rate following Arrhenius law was applied. This implies that the subgrid scale effects were not modelled, i.e., $\kappa_{SGS} = 0$ as shown in Equation (4.2.41). With a validation of the computational code for one dimensional flame structure, two dimensional mixing layer simulation was performed. The simulation results show that the shear layer growth and products formation were reduced by the energy release due to combustion, and these effects qualitatively agreed with information from experiments. In Reference [35] three dimensional, hydrogen and air combustion, square jets were presented based on the above numerical method, and the focus was on relations between energy release due to combustion and a growth and entrainment of the jet.

The capability of ILES as an engineering tool for combustion flow can be seen in a simulation of a three dimensional complex geometry gas turbine combustor [33]. In this research, again, ILES technique with second order accurate method was applied to the convective terms without explicit subgrid scale modelling. Global one and two steps finite rate Arrhenius law reactions were examined but subgrid contribution of the chemical reaction was neglected. Conventional LES with flame-wrinkling model for chemistry in which laminar flame structure is applied and the velocity and temperature profile along centreline axis showed reasonable agreement with experimental data..

Similarly, an ILES was performed with finite rate reaction following Arrhenius law [25]. For inviscid terms ILES with second order accurate scheme was applied in finite

volume method, and no subgrid viscous and diffusion terms were given explicitly since they were considered to be built in the numerical method. The contribution of the chemical reaction term in the subgrid scale was neglected, and the reaction rate was simply calculated by the implicitly filtered variables. This condition is corresponding to the segregation factor $\kappa_{SGS} = 0$. Simulation of a flame holding behind a flame holder showed that ILES results reasonably agreed with the experimental data and they were comparable to the conventional LES results in which one-equation eddy-viscosity model was used.

4.3.2 Numerical Modelling for ILES

In the ILES computation, the governing equations are solved without explicit filtering operation. Therefore, the governing equations for species, momentum and energy are the same formulation as those of instantaneous flow, shown in Equation (4.2.12), (4.2.5) and (4.2.13).

The governing equations are solved using a finite volume Godunov-type method. As the same scheme as applied in the non reactive flow simulation, for the advective terms fifth-order spatial accuracy MUSCL limiter was used to achieve high-order spatial accuracy, and the HLLC approximate Riemann solver was applied. Also, the velocity components are locally modified for low Mach number flow in the reconstruction process. The viscous, heat and diffusion terms appeared in the right hand side of equations were discretised using standard central differences. For the time integration, a second-order explicit Runge-Kutta method was employed.

With this ILES numerical method, the momentum Equation (4.2.5) is solved with built in subgrid scale modelling, which is equivalent to solve the filtered momentum Equation (4.2.20). Also, unlike the conventional LES equations, unresolved scalar flux terms appeared in filtered species Equation (4.2.21) and energy Equation (4.2.22) are accounted by the numerical dissipation built in the characteristics of the ILES high-resolution method.

For the reaction source term $\dot{\omega}$, non filtered reaction rate from in Equation (4.2.39) is applied. Although this implies that the chemical reaction effects in the subgrid scale are not accounted in the simulation, it is important to know how the turbulence model of the high-resolution method effects on the chemical reaction rate in the temperature field, compared to the laminar flame case shown in Figure 4.5. Therefore, this model is appropriate to examine the combination of ILES with chemical reaction.

4.3.3 1D Simulation of A Premixed Flame

Simulation Setup

One dimensional methane-air laminar premixed combustion simulation has been performed first to validate the ILES numerical method combined with chemical reactions

and thermodynamic transport models. The grid resolution and the time step were examined by results of the flame speed and the flame structure. The computational domain was initially split into two regions at $x = 0$. Unburnt methane-air stoichiometric mixture with standard temperature $T_{std} = 298.15K$ and burnt mixture of water vapour and carbon dioxide with the adiabatic flame temperature $T_{ad} = 2223K$ filled $x < 0$ and $x \geq 0$ regions, respectively. Static pressure of the mixture was $1atm$ throughout the domain. The grid size was set according to the following evaluation of the flame thickness. The flame thickness δ for the stoichiometric mixture can be estimated $0.43mm$ without numerical computation but from thermochemical properties [71]:

$$\delta_D = \frac{2D_u}{S_L}\left(\frac{T_{ad}}{T_{std}}\right)^{0.7} \tag{4.3.1}$$

where D_u and S_L represent a diffusion coefficient of unburnt gas and a flame speed, respectively. This value is within the variation 0.3-1.0mm reported in experimental measurements by [30] and a computation by [5]. The mesh size was set to constant $0.025mm$ so that roughly 15 to 20 grid points can be involved in the flame thickness. As a boundary condition, both ends of the domain were set as open outflows. The physical domain had $40mm$ length which was large enough to avoid initial pressure wave propagating from the flame to the open boundary.

Flame Structure

Figure 4.7 shows species mole fraction profiles within the flame. Note that the horizontal axis was shifted to fit the highest carbon monoxide mole fraction to distance 0. The simulation results well matched to the experimental data by [9]. Pressure difference between unburnt and burnt gas was observed $0.7Pa$ which corresponds to $O(1)$ described in [71]. This implies not only that the premixed flame propagation can be considered as constant pressure phenomena but also that the compressible simulation code applied here works properly.

The flame speed was simply measured $0.32m/s$ by the propagation of an isothermal location in the flame, e.g., $1000K$. A more consistent definition of the flame speed described in [71]:

$$S_L = -\frac{1}{\rho_u Y_u}\int_{-\infty}^{+\infty} \dot{\omega}_{CH4} \tag{4.3.2}$$

yields $0.38m/s$, where subscription u and b represent burnt and unburnt gas, respectively. The flame thickness was evaluated by the maximum gradient of the temperature curve within the flame [71]:

$$\delta_T = \frac{T_b - T_u}{max\left(\frac{\partial T}{\partial x}\right)} \tag{4.3.3}$$

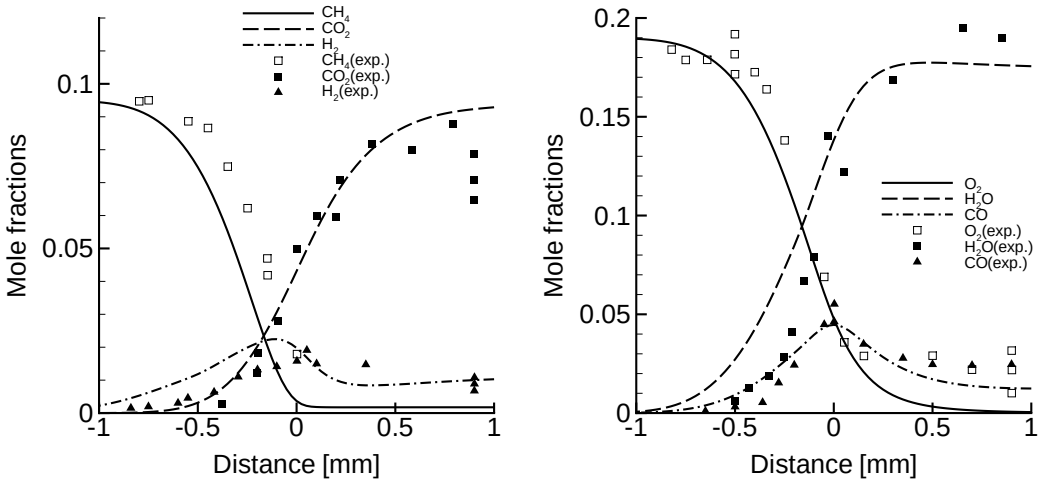

Figure 4.7: Species profiles of the one dimensional premixed flame

The result 0.49*mm* well matched to δ_D, implying that the thermodynamic coefficients used in the simulation are acceptable.

4.3.4 2D Simulation of A Mixing Layer

Simulation Setup

Methane-air turbulent nonpremixed combustion simulation has been performed with a two dimensional parallel flow. As shown in Figure 4.8 the physical domain was rectangular with length 19*mm* for *z* direction along the flow axis and width 14*mm* for *x* direction. The uniform and the same size meshes as employed in the premixed test case were contained in the domain. Methane and air flows were separately incoming to the domain, $x > 0$ for methane and $x \leq 0$ for air, respectively, from the bottom $z = 0$ with a velocity ratio three to one. On the side boundaries (left and right of the domain) a symmetry condition with respect to *x* direction was set, and zero velocity and mass fractions gradient were set on the outflow boundary at the top of the domain. The domain was initially filled with methane and air with constant axial velocity. An fluctuation velocity component which was used in the non reactive flow case was added at the inlet velocities. The initial pressure was set constant 1*atm*, and temperature was 950*K* for methane and 1100*K* for air, respectively. The gas temperatures were high enough to ensure the auto ignition of the mixture. Reynolds number based on the average velocity of the methane and air, average kinematic viscosity and initial mixing layer thickness δ was $\simeq$ 3500. Note that air was considered to consist of only two species, namely nitrogen and oxygen with mass fraction 0.768 and 0.232, respectively.

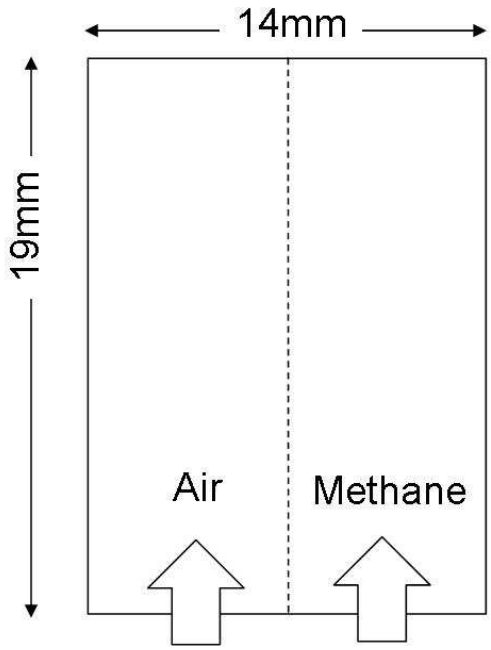

Figure 4.8: Schematic of the two dimensional mixing layer domain

Scalar Field

Figure 4.9 shows contour floods of instantaneous species mole fractions. The methane contour flood shows a growth of a series of eddies and entrainment of species into the other side. The carbon monoxide contour flood depicts that the chemical reaction occurred from the inflow boundary ($z/\delta = 0$). The carbon dioxide mole fraction can be observed only at downstream region and the high concentration can be seen at the edge of the large eddies while high carbon monoxide concentration exists at the centre of the eddies. This implies that the mixing of carbon monoxide and water vapour in the so-called water gas shift reaction (4.2.48) takes place mainly at the edge of the eddies and a rapid mixing after the formation of carbon monoxide is necessary for a complete combustion.

Figure 4.10 shows scatter plots of species mass fraction of the mixture in the domain against mixture fraction f which is defined in Equation (4.2.52). Methane and oxygen mass fraction maps show that the plots are distributed within the region surrounded by a mixing line where non chemical reaction takes places ($\dot{\omega} = 0$), and a fast chemistry line which was obtained by the Burke-Schumann analytical solution assuming one step, irreversible, infinite rate chemical reaction ($\dot{\omega} = \infty$). It is obvious that methane molecules exists in the oxygen rich mixture ($f < 0.055$) and oppositely, oxygen exists in the fuel rich mixture ($f > 0.055$). This implies that the fuel and air exist together in a piecewise volume for which chemical reactions were applied, and that the finite rate chemical reaction properly worked in the ILES simulation. In the oxygen mass fraction map, the plots show a uniform distribution between the mixing line and the equilibrium

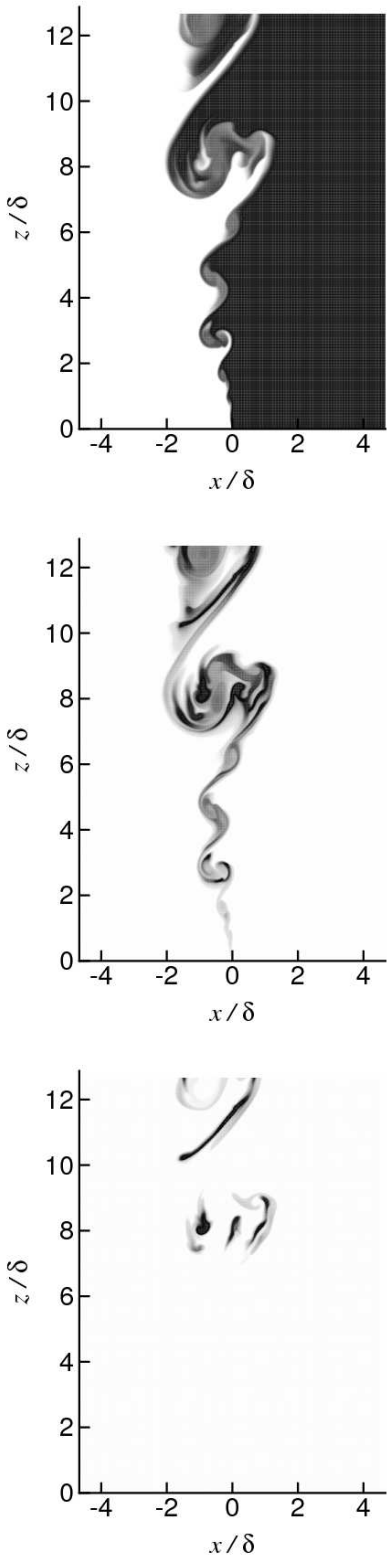

Figure 4.9: Instantaneous mole fraction contour floods of the two dimensional mixing layer: methane (top), carbon monoxide (middle) and carbon dioxide (bottom)

line for a constant mixture fraction, and hence it demonstrates non uniform chemical reaction rate of the mixture. This variety of the chemical reaction rate is due to the shape of the chemical source term (4.2.39) which does not account for the chemical reaction effect in the subgrid scale. The plots concentrates in $f > 0.35$, showing that the fuel rich mixture remains without further chemical reaction. This might result in incomplete combustion. In the water vapour mass fraction map, the plots are located in the lower region than the fast chemistry line in the fuel rich condition, showing slow reaction rate of reaction(4.2.47) and (4.2.49). This is because the intermediate product hydrogen was not reacted properly as described in the chemical reaction (4.2.48). For the same reason, the carbon dioxide scatter plots show smaller values of mass fraction than the analytical values.

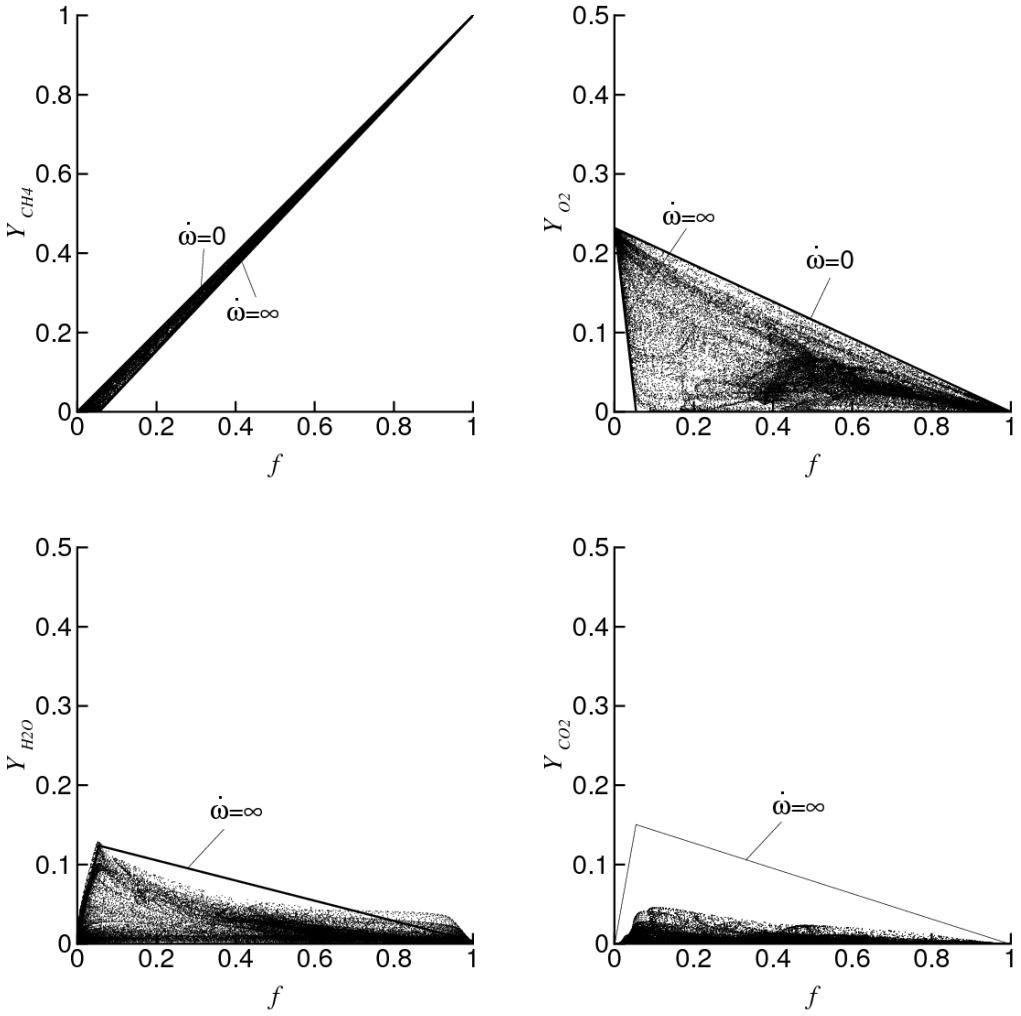

Figure 4.10: Species distribution in mixture fraction field: methane (top left), oxygen (top right), water vapour (bottom left) and carbon dioxide (bottom right)

Effects of the Non Filtered Chemical Source Term on Temperature Field

Figure 4.11 shows a comparison of distribution of the normalised temperature (Equation (4.2.35)) between reversible and irreversible chemical reactions. T_{max} was set as the maximum temperature obtained in the irreversible reaction test case. For irreversible chemical reactions, the backward reaction rate in Equation (4.2.49) was neglected. Analytical temperature profile with irreversible fast chemistry assumption is also plotted in the graph. For the irreversible chemistry test case, the highest temperature is obtained at $f = 0.09$, with the equivalent ratio higher than the stoichiometric condition, 1.0, which reflects the effects of the finite rate chemical reactions as described in [81]. Also, the finite rate reaction influences the temperature distribution. In the fuel rich condition $f > 0.25$, the reaction rate is not high enough to reach to the temperature corresponding to the analytical solution while in the fuel lean condition the scatter plots showed good matching with the analytical solution. For the reversible chemistry test case, the plots showed the similar feature but with about 80% of the maximum temperature compared with the irreversible chemistry test case.

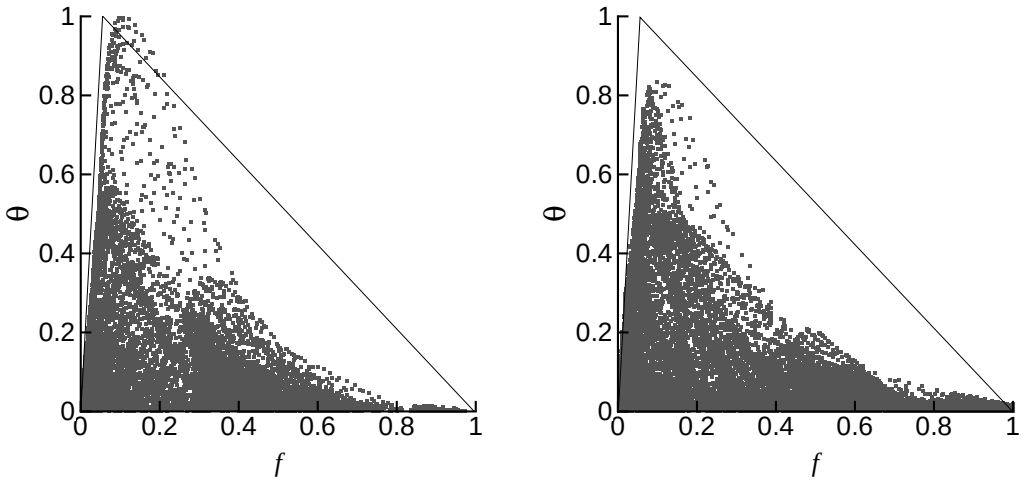

Figure 4.11: Temperature distribution in mixture fraction field for irreversible (left) and reversible (right) chemical reactions

Figure 4.12 shows temperature field at the downstream distance from the flow inlet, $z/\delta = 6$ and 12. At the distance $z/\delta = 6$, the mixture of near stoichiometric condition was not fully ignited. The temperature plots in the fuel lean region $f < 0.03$ show a linear increase but low temperature. At the distance $z/\delta = 12$, mixture of near stoichiometric condition was well ignited and obtained high temperature, and the plots matches the fast chemistry line in the fuel lean region. These observation can match to the DNS research for auto ignition of shearless methane air mixing layer flame [63] where the one step Arrhenius law was used. In their research however, the highest temperature was observed at around $f = 0.2$ in the ignition process while in the current simulation high temperature was obtained at around $f = 0.1$.

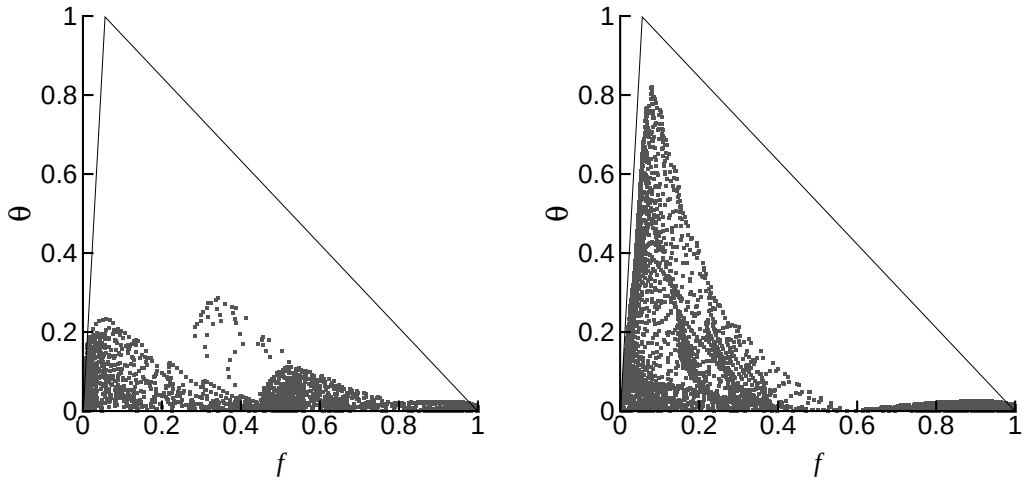

Figure 4.12: Temperature distribution in mixture fraction field: short distance ($z/\delta = 6$, left) and long distance ($z/\delta = 12$, right)

Figure 4.13 shows reaction rate of methane against temperature. The one dimensional premixed flame test case is also presented. Furthermore, DNS of a three dimensional premixed turbulent flame containing 17 species and 73 chemical reactions [79] is shown. Note that the reference data was adjusted to occupy the same area as the ILES premixed case. The distribution shows that a typical nonpremixed flame in which the reaction rate is non-zero for all range of temperature. However, a small reaction rate range can be seen at the low temperature $\theta < 0.1$. This implies that the non filtered Arrhenius law reaction model applied in the simulation is valid for non premixed flames but causes slow combustion. Therefore, when the chemical reaction time is considered to be short compared to the mixing time, the chemical source term should be improved to demonstrate larger values in the low temperature range.

Figure 4.14 shows conditional average of the methane reaction rate at different axial position. It was observed in the early stage $z/\delta < 9$ that the methane reaction rate decreased and the non zero range increased with the flame development. After the flame was developed $z/\delta > 9$, the increase of the reaction rate can be seen. The largest reaction rate was obtained in the process of ignition, $z/\delta = 0.3$ at around $\theta = 0.39$ and its corresponding mixture fraction was 0.11. In reference [63] the largest reaction rate at the time of ignition was obtained at around $f = 0.15$.

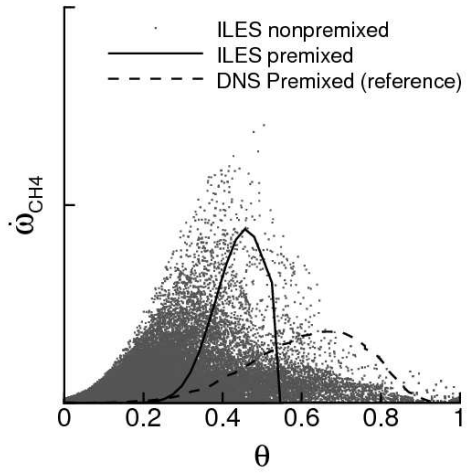

Figure 4.13: Methane reaction rate of nonpremixed flame and premixed flame

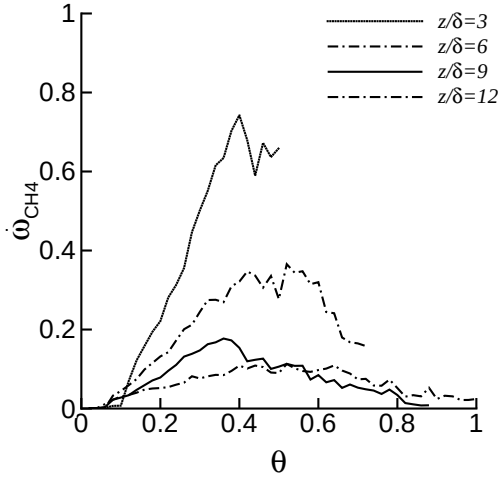

Figure 4.14: Methane reaction rate profile at different distance from the inlet

4.4 Fast Chemistry Approach

As an opposite modelling to the finite rate approach in the previous section, a fast chemistry approach is introduced in this section. In the fast chemistry model the chemical reaction takes places instantaneously, and therefore, the mixing time scale is considered to be longer than the chemical reaction time scale. Therefore, this model is corresponding to $\tau_r \ll \tau_m$ and $\kappa_{SGS} = -1$ in Equation (4.2.42).

An advantage of this method is small computational cost since flame position and structure which depends on the chemical reaction rate do not need to be captured. Instead, temperature and species mass fraction are calculated by linear relation to mixture fraction, and therefore the grid size can be the same as that used in non reactive flow simulation. Therefore, mixture fraction can be a fundamental variable when the fast chemistry approach is applied. Oppositely, a disadvantage is that only four species in Equation (4.2.45) can be tracked and hence, species H_2 and CO, which are commonly observed in experiments cannot be predicted.

In incompressible solvers of RANS and conventional LES, a linear relation between mixture fraction and scalar variables can be explained as follows. Together with the one step irreversible methane air chemical reaction of Equation (4.2.45), the following assumptions are considered,

- Low Mach number approximation ($p = constant$).
- All the diffusion coefficient of species are equal ($D_k = D$).
- All the specific heat capacities for constant pressure are equal ($C_{p,k} = C_p$)).
- The ratio of diffusion to thermal diffusivity is unity ($Le_k = Le = 1$).

Under these assumptions, species mass fraction Equation (4.2.12) and an energy equation which is rewritten with respect to enthalpy can be derived:

$$\frac{\partial \rho Y_k}{\partial t} + \frac{\partial}{\partial x_j}(\rho u_j Y_k) = \frac{\partial}{\partial x_j}\left(\rho D \frac{\partial Y_k}{\partial x_j}\right) + \dot{\omega}_k \tag{4.4.1}$$

$$\frac{\partial \rho h}{\partial t} + \frac{\partial}{\partial x_j}(\rho u_j h) = \frac{\partial}{\partial x_j}\left(\rho D \frac{\partial h}{\partial x_j}\right) + \dot{\omega}_T \tag{4.4.2}$$

where k is fuel or oxidiser and $\dot{\omega}$ is heat release due to chemical reaction. Note that the viscous effect in the enthalpy equation is also neglected since this term is order of Mach squared and small enough in low Mach number flow. Then, a single variable, which is identical to element mass fraction can represent species mass fractions and enthalpy of these equations:

$$\frac{\partial \rho Z_i}{\partial t} + \frac{\partial}{\partial x_j}(\rho u_j Z_i) = \frac{\partial}{\partial x_j}\left(\rho D \frac{\partial Z_i}{\partial x_j}\right) \tag{4.4.3}$$

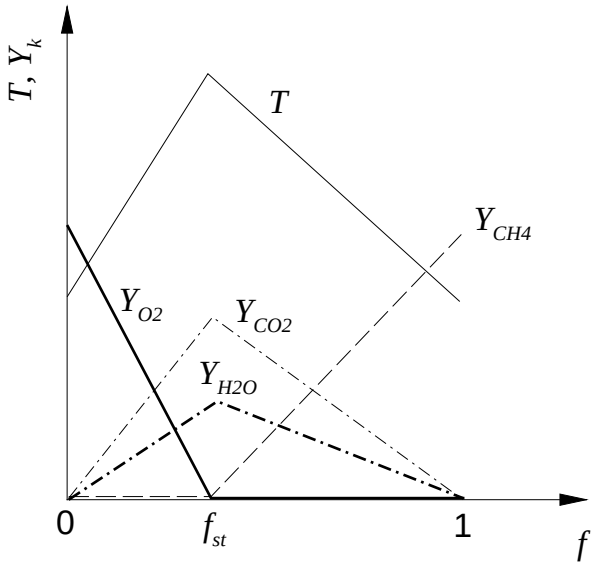

Figure 4.15: Schematic of Burke-Schumann flame structure model

As described in Equation (4.2.51), mixture fraction can replace the element mass fraction. The balance equation with respect to the mixture fraction becomes the same shape as Equation (4.4.3). The computation of chemical reaction can be separated from turbulent flow simulation since the equation does not include a chemical source term .

As a result, incompressible RANS and conventional LES solve conservation equations of mass, momentum and mixture fraction. Flame structure is given by a linear relation between mixture fraction and mass fraction and temperature, for example, the Burke-Schumann model shown in Figure 4.15. At (fuel) lean condition corresponding to $f < f_{st}$, with f_{st} being mixture fraction under the stoichiometric condition, methane does not exist, and oppositely oxygen does not exist at the (fuel) rich condition $f > f_{st}$. At $f = f_{st}$ only carbon dioxide and water vapour exist and the highest temperature is obtained.

4.4.1 Governing Equations for ILES

Since the fast chemistry approach can separate turbulent flow calculation from chemical reaction, the ILES method applied to the non reactive flow in the previous chapter is applied for the turbulent flow calculation. However, mass fractions instead of volume fractions are tracked. Also, correction velocity in Equation (4.2.11) is evaluated to ensure the total mass. With this method four species can be tracked by six equations: species $\times 4$, momentum $\times 1$ and energy $\times 1$. Note that pressure is not constant since

compressible conserved equations are solved, and that specific heat ratio is calculated for each species. However, the diffusion term in the species equation is not calculated. This is because the diffusion coefficient usually much smaller than the turbulent diffusion coefficient [69] which is accounted and produced in the high-resolution method. The heat conductivity is evaluated from viscous coefficient through Prandtl number as the same way as in the non reactive flow simulation. Then, the following ILES conservation equations for species, momentum and energy can be solved for turbulent flow:

$$\frac{\partial \rho Y_k}{\partial t} + \nabla\cdot(\rho \mathbf{u} Y_k) = 0 \tag{4.4.4}$$

$$\frac{\partial \rho \mathbf{u}}{\partial t} + \nabla\cdot(\rho \mathbf{u}\mathbf{u}) = -\nabla\cdot\mathbf{P} \tag{4.4.5}$$

$$\frac{\partial \rho E}{\partial t} + \nabla\cdot(\rho E \mathbf{u}) = -\nabla\cdot(\mathbf{P}\cdot\mathbf{u}) - \nabla\cdot\mathbf{q} \tag{4.4.6}$$

For the chemical reaction calculation, mixture fraction is first calculated as passive scalar by mass fractions, as shown in Equation (4.2.52). The computed mixture fraction is passed into the prerequisite frame structure which is the Burke-Schumann fast chemistry model described in the previous sub section, to obtain the burnt gas mixture composition and temperature. The density of the burnt gas is calculated so that the total mass should be conserved in the cell. And then, pressure of the burnt gas is obtained by the equation of state.

4.4.2 3D Simulation of A Methane Jet Flame

Simulation Setup

Three dimensional swirl flame simulation was performed. The methane and air non-premixed burner geometry and the computational domain size was set as the same as applied in the non reactive flows simulation; axial length is $5 \times D$ and radial length of $8.8 \times D$. Grid resolutions are also the same as the typically adopted in non reaction simulation, as shown in Table 4.2.

Table 4.2: Grid size for the fast chemistry test case

Axial	Radial	Circumferential	Total
300	62	32	0.60×10^6

Mean inflow velocity condition are summarised in Table 4.3 with u_{f0}, $u_{a0,z}$, $u_{a0,r}$ and $u_{a0,c}$ representing fuel, axial air, radial air, and circumferential (azimuthal) air velocity,

(m/s) respectively. The coflow is constant $20.0 m/s$ for all test cases. These inflow conditions correspond to the test cases of swirl flames selected in TNF workshop. In the experiments 2% fluctuation velocity was observed in coflow [59] but this was not accounted in the simulation. The test case is named SM1. In the experiments, compressed natural gas, 90% of which is composed of methane and rest of them are other hydrocarbons, was used instead of pure methane for the velocity measurements. Species measurements had done separately from velocity measurements and done with pure methane gas.

Reynolds number based on the fuel jet velocity, the diameter of fuel nozzle $3.6mm$, and methane gas viscosity is 7.2×10^3. In this combustion test case, turbulent velocity fluctuating component is not added to the fuel and air inflow in order to avoid excessive turbulent fluctuation which can affect the subgrid scale fluctuation u'_{SGS} and segregation factor κ_{SGS} in Equation (4.2.41).

Table 4.3: Inflow velocity [m/s] for the fast chemistry test case

	u_{f0}	$u_{a0,z}$	$u_{a0,r}$	$u_{a0,c}$	SN
SM1	32.7	38.2	0.0	19.1	0.5

Flow Structure

Figure 4.16 shows instantaneous axial velocity, vorticity magnitude contour floods and temporally averaged axial velocity of the SM1 case. The flow structure is similar to the non reactive case and the velocity is slow on the bluff body plate. In the vorticity contour, large vorticity magnitude can be observed far downstream, which was not seen in the non reactive case. In the averaged flow picture the colour balance was adjusted to emphasise the flow shape. The swirling air flow narrowed at around $z/D = 1.0$, similar to the non reactive case shown in Figure 3.24. However no clear recirculation zone can be observed.

Figure 4.17 and 4.18 show mean axial and circumferential velocity profile for the SM1 case, respectively. The profiles are compared with experiments [59] and several conventional LES results [45] in which typical combination of turbulence and chemistry model were applied; Smagorinsky model for turbulence, linear eddy model, flamelet model or filtered density model for chemistry model. For these LES results, only variance is shown at several radial location for clarity. In general, the ILES results showed a fair agreement with experiments and comparable profiles to the conventional LES.

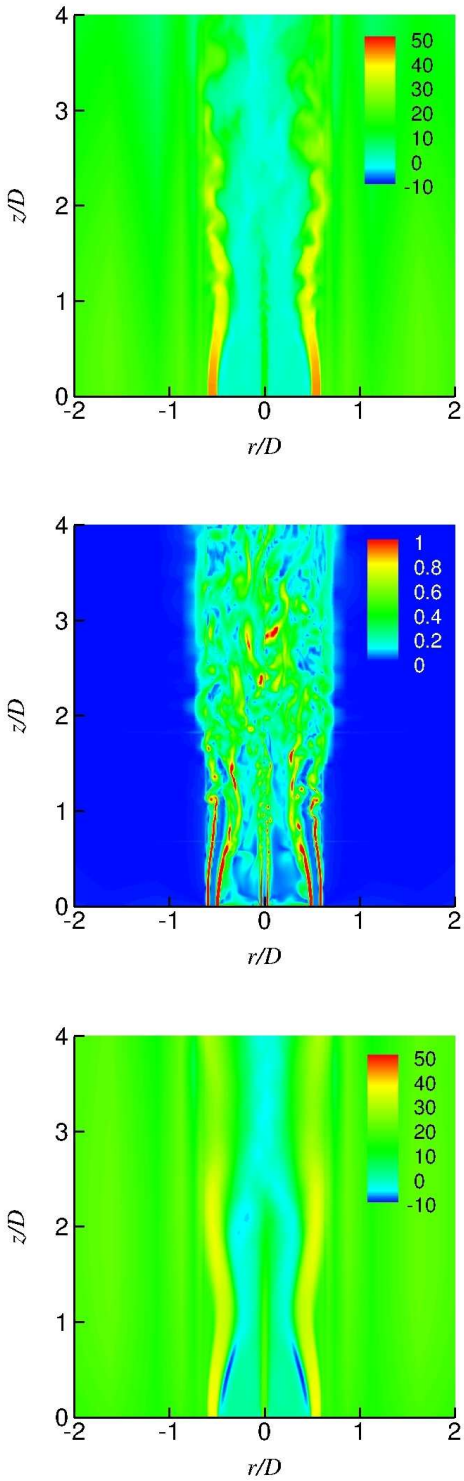

Figure 4.16: Methane air flame with fast chemistry: instantaneous axial velocity [m/s] (top), instantaneous vorticity magnitude normalised by the maximum value in the domain (middle) and temporally averaged axial velocity [m] (bottom)

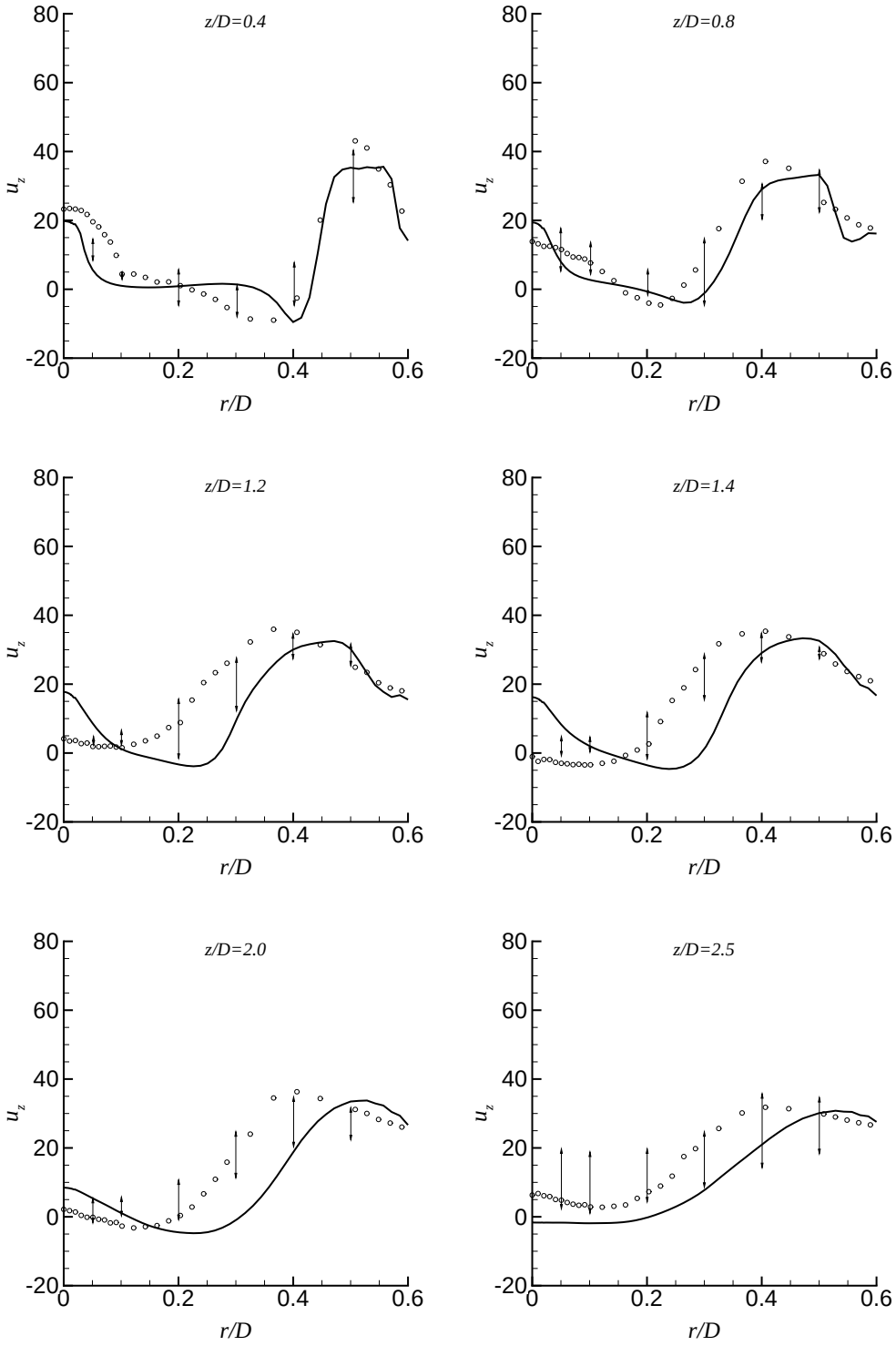

Figure 4.17: Mean axial velocity [m/s] at different axial distances from the burner surface. The solid line is ILES and the circle marks are experiment [59]. Arrows show the variance of several reference LES results [45] at typical radial location

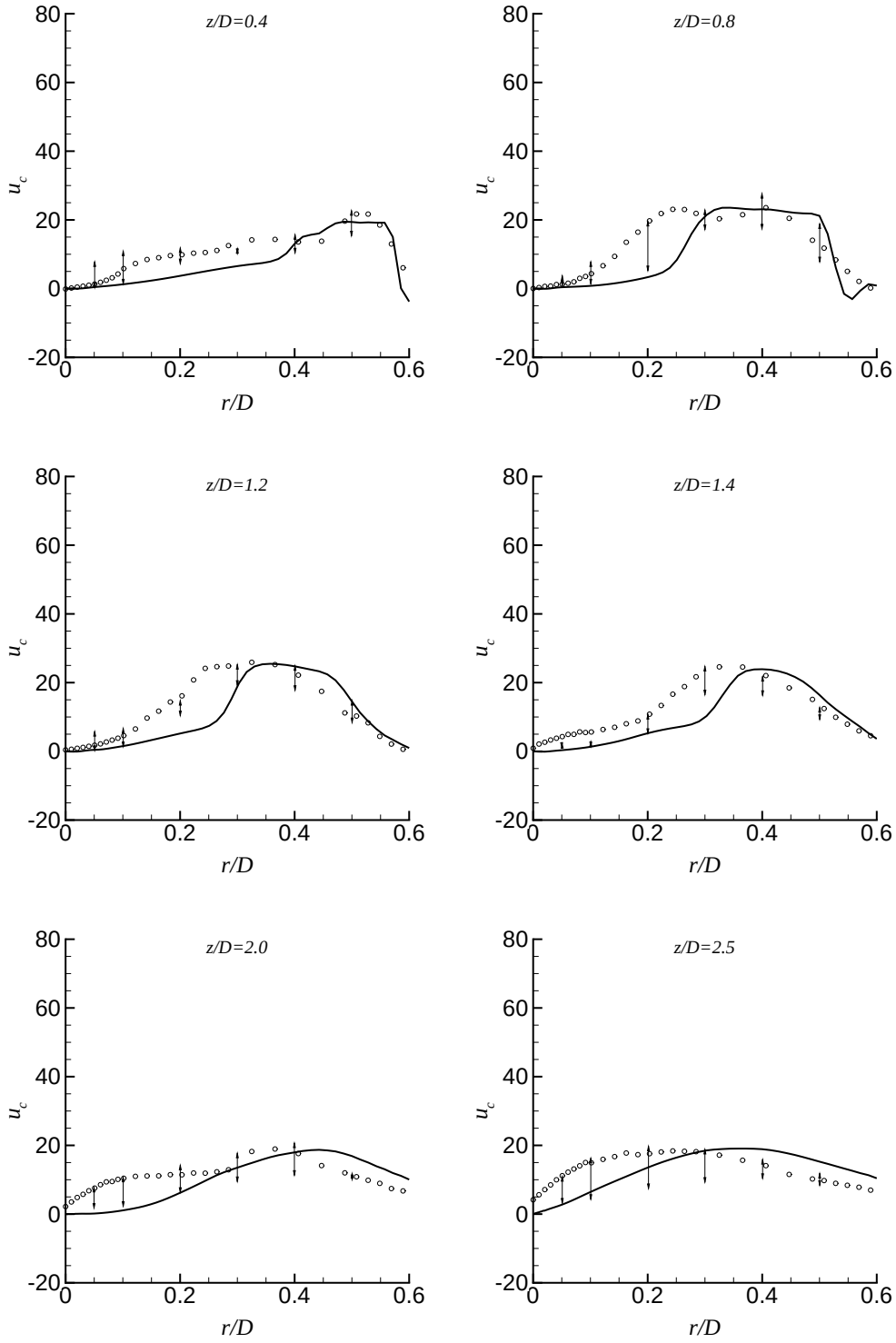

Figure 4.18: Mean circumferential velocity [m/s] at different axial distances from the burner surface. The solid line is ILES and the circle marks are experiment [59]. Arrows show the variance of several reference LES results [45] at typical radial location

Scalar Field

Figure 4.19 (left) shows instantaneous temperature contour flood. The central methane jet penetrates up to $z/D < 1.5$ without combustion, results in low temperature in this region. High temperature region can be observed in the recirculation zones and at the downstream ($z/D > 2.0$). Since temperature and species fractions are correlated to mixture fraction by linear Burke-Schumann model shown in Figure 4.15, the scalar field can be represented by only mixture fraction. However as depicted in Figure 4.19 (right) temporally averaged radial distribution of mixture profile showed a large discrepancy, particularly around the central jet region. This is simply because non fluctuation component was added to the inflow boundary condition. These results implies that the ILES and fast chemistry approach can match and predict flow field reasonably accurate, however, the simple linear correlation of scalar variables and mixture fraction cannot predict well the scalar field without setting accurate inflow boundary fluctuation which effects the segregation factor κ_{SGS}.

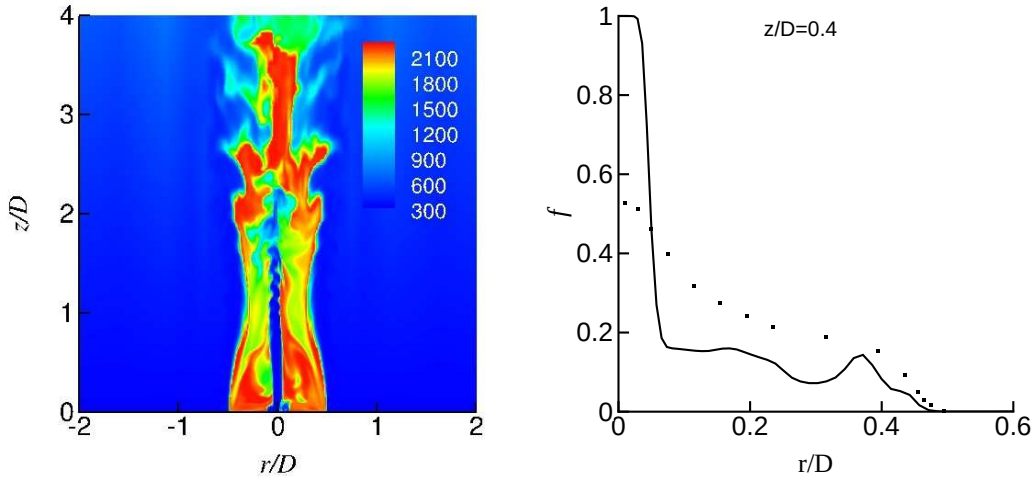

Figure 4.19: Instantaneous temperature [K] contour flood (left) and mean mixture fraction (right)

4.5 Summary

ILES with high-order high-resolution computational modelling was applied to methane and air flame. The governing equations for compressible flow using a finite volume Godunov-type method were solved with applying fifth-order spatial accurate reconstruction methods and with a third order explicit Runge-Kutta time integration.

In the ILES calculation, no filtering operation is set, and therefore, unlike conventional LES, the governing equations of ILES do not include unknown terms in species, momentum and energy equations except for a chemical source term. Therefore, the equations are the same shape as instantaneous (non filtered) equations. The chemical source term does not appear in the energy equation when formation enthalpy is included in conservative total energy and only appears in the species equation. For evaluation of transport properties, Sutherland's law was applied for viscosity and then, heat conductivity and diffusion coefficients were calculated by constant Prandtl number and constant species Lewis number, respectively. The non filtered Arrhenius law was applied for the chemical source term. An analysis showed that the non filtered Arrhenius law cannot represent the filtered (or limited in ILES) chemical source term since the chemical reaction is nearly zero when the temperature increment is small and very large when the temperature increment is large. Also, the analysis showed that the correlations between fluctuations of species mass fraction and temperature needs to be modelled if the turbulent and chemistry interaction is accounted in the subgrid scales. Therefore, the applied model is simple but may not be sufficient for detail analysis of interaction of turbulent mixing and chemical reaction due to the lack of consideration for subgrid scale chemical reactions. However, it is selected in order to investigate the combination of chemical reaction with ILES in the case when the time scale of chemistry is long compared to that of turbulence. For chemical reactions, a finite rate four step global chemical reaction was used since it can track hydrogen and carbon monoxide which can be observed in the slow chemical reactions due to the simple Arrhenius law model.

The combination of ILES and chemical reaction was examined by the flame structure and the flame speed of one dimensional premixed flame computation. The results of species distribution in the flame agreed well to the experimental data. The flame speed based on the temperature profile of the flame well matched to the prerequisite flame speed calculated by thermodynamical properties. Two dimensional mixing layer simulation was then performed to demonstrate ILES of nonpremixed flame. The species scatter maps showed that the plots were within the boundary of the mixing line where gases were well mixed but no ignition took place, and the fast chemistry line where the mixture was fully ignited and chemical reaction occurred. The temperature field was depicted against mixture fraction and the maximum temperature was obtained at the fuel rich mixture side, which corresponded to experimental and other simulation data. Also, the evolution of the temperature field due to the ignition of the mixture was observed along the distance from the fuel and air inlet. A discrepancy from referenced simulations were observed; the reaction rate was not high enough in the fuel rich mix-

ture while the results showed good matching in the fuel lean mixture. The reaction rate of methane plotted against temperature showed non zero reaction rates for all temperature, which is typical for nonpremixed turbulent flames. However, the reaction rate showed small values in the low temperature region and this causes the slow chemical reaction rate. This implies the subgrid scale effect of the chemical source term, which was not accounted in this simulation.

Next, simulation was performed with fast chemistry approach which is regarded as an opposite modelling of the chemical source term with respect to the time scale of chemistry and turbulence, i.e., the case of longer turbulent time scale compared to the chemical time scale. In this approach, turbulent flow simulation was separated from chemical reactions and the chemical source term vanished in the species equation. For flame structure calculation a linear correlation of mass fraction and temperature to mixture fraction, which was computed as a passive scalar from turbulent flow simulation, was applied. The grid resolution could be set as the same as one used in non reactive flow, which made three dimensional simulation possible.

The ILES computation was done with a 0.6 million point grid with fifth-order spatial accurate limiter. Mean velocity filed of a swirl burner flame were compared with experimental data and conventional LES. The discrepancies are large compared to the non reactive case, however, a fair agreement and comparable accuracy were achieved. The scalar field which can be represented by a single variable, mixture fraction was plotted however, the profile could not reach to reasonable agreement with the experiments and LES when no fluctuation component was added to the inflow boundary condition. Simulations were performed with the same computational facility as used in the non reactive flow simulation and the computational time producing a typical result on the medium grid with the fifth-order limiter was about 3,840 hours.

With these results it is considered that the ILES can match to the combustion flow without setting explicit modelling of subgrid viscous term and subgrid transport terms. For well burnt flames in which chemical reaction completes ILES with a simple fast chemistry approach can simulate with reasonable accuracy for velocity filed. For incomplete combustion flames and in the consideration of intermediate species, e.g., carbon monoxide, NOx and radicals, direct calculation of chemical source term is available, however, large error can be possible unless fine grids are applied.

CHAPTER 5

Conclusions and Suggestions

5.1 Conclusions

This thesis covered numerical methods and analyses of non reactive and reactive flows using an ILES technique based on high-resolution and high-order methods.

For the non reactive flow, the ILES simulation solved the governing equations for compressible, single phase, multi-species flow using a finite volume Godunov-type method without explicit modelling of the subgrid scales. Instead of mass fraction tracking a volume fraction tracking method by Allaire was applied. Second, fifth and ninth-order limiters were used to achieve high order spatial accuracy and a third-order explicit Runge-Kutta method for time integration was applied.

Temporally and circumferentially averaged flow profiles were compared with the experimental data. The axial and the radial velocity and rms velocity profiles showed good agreement in the strong turbulent region, the recirculation region and the downstream region of the flow fields. Also, the mixture fraction profiles demonstrated a good agreement to the experimental data in the multi-species flow simulations.

The one dimensional kinetic energy spectrum was examined to evaluate the effects of grid resolution and limiter on energy dissipation in the ILES computation method. An ideal $k^{-5/3}$ decay of energy can be seen in a certain range that increased with grid resolution. In computations with the fifth-order accurate limiter the cut-off wavenumbers were found to be larger than the estimated maximum wavenumbers appearing on the given computational grid. This implies that the numerical dissipation sufficiently accounted for the energy transportation between large and small eddies up to the effective cut-off. The second, fifth and ninth-order limiter were examined on the medium grid. The fifth-order limiter showed good resolution of the kinetic energy dissipation with reasonable computational time compared to the second-order limiter. The ninth-order limiter required substantially larger computational power.

To investigate effects of density differences between fuel and air, numerical simulations were performed on different density fuel jet flows with corresponding Atwood number from 0 to 0.871. Temporally and spatially averaged mean streamlines and velocity contours showed that with an identical momentum flux of the fuel jets, the flow

structure and velocity field were unchanged by Atwood number, except for the central fuel jet region. At the centre axis, the velocity decay rate increased monotonically with the increase of Atwood number, which resulted in the same velocity profile at further downstream. The volume fraction field changed due to the variation of injected fuel volume into the domain, however, a large, constant fuel volume fraction region was formed for all test cases. The amount of the volume fraction in this region was controlled by species mixing at a point where fuel and air stream collided. This point is located at the top edge of the recirculation zone, and a large rms volume fraction was observed for all test cases. A mixing parameter originally introduced for investigating the mixing of molecular species in a mixing layer was applied to complex turbulent flow. It was found that the degree of molecular mixing decreased at the mixing point with the increase of Atwood number. The simulation results showed that the feature of the mixing field and the effects of Atwood number can be described with this parameter.

With regard to the combustion flow simulation, ILES with high-order high-resolution computational modelling was applied to methane air flame and the governing equations for compressible flow were solved using a finite volume Godunov-type method. Just as for non reactive flow simulations, fifth-order spatial accurate reconstruction methods were applied with a third order explicit Runge-Kutta time integration. In the ILES calculation, no filtering operation was set and hence, unlike conventional LES, the governing equations of ILES do not include unknown terms in species, momentum and energy equations except for chemical source term. The chemical source term appears only in the species terms and requires a non filtered Arrhenius law. This model was selected in order to investigate the combination of chemical reaction with ILES for the case when the time scale of chemistry is long compared to that of turbulence. For chemical reaction modelling, a finite rate four step global chemical reaction was applied.

The combination of ILES and chemical reaction was examined by the flame structure and the flame speed of one dimensional laminar premixed flame computation. The results agreed well to the experimental data. Two dimensional mixing layer simulation was then performed to demonstrate ILES of nonpremixed flame. The species mass fraction scatter maps showed that the mixture gas conditions were within the mixing line, where gases are well mixed but no ignition takes place, and the fast chemistry line, where the mixture is fully ignited and chemical reaction occurs. The temperature field was depicted against mixture fraction and the maximum temperature was obtained at the fuel rich mixture side, which corresponded to experimental and other simulation data. Also, the evolution of the temperature field due to the ignition of the mixture was observed along the distance from the fuel and air inlet. A discrepancy from referenced simulations was observed: the reaction rate was not high enough in the fuel rich mixture while the results showed good matching in the fuel lean mixture.

The reaction rate of methane plotted against temperature showed non zero reaction rates for all temperatures, which is typical for nonpremixed turbulent flames. However, the reaction rate showed small values in the low temperature region and this causes the

slow chemical reaction rate. This implies that the effects of the chemical source term in the subgrid scale was not accounted in this simulation.

Simulation was performed with fast chemistry approach that is regarded as an opposite modelling of the chemical source term with respect to the time scale of chemistry and turbulence, i.e., the case of longer turbulent time scale compared to the chemical time scale. In this approach, turbulent flow simulation was separated from chemical reactions and the chemical source term vanished in the species equation. For flame structure calculation a linear correlation of mass fraction and temperature to mixture fraction, which was computed as a passive scalar from turbulent flow simulation, was applied. The grid resolution can be set as the same as one used in non reactive flow and hence, three dimensional simulation is possible. The mean velocity of a swirl burner flame were compared with experimental data and conventional LES and a fair agreement was achieved.

From these results, obtained by the combination of turbulent flow calculation with slow and fast chemistry, it can be concluded that the ILES can match to the combustion flow without setting explicit modelling of subgrid viscous term and subgrid transport terms. For well burnt flames in which chemical reaction is complete ILES with a simple fast chemistry approach can be reasonably accurate. For incomplete chemical reaction flames and in the consideration of intermediate species, e.g., carbon monoxide, NOx and radicals, direct calculation of chemical source term is available but large errors are possible without the application of fine grids.

This work contributed to knowledge of computational fluid dynamics by:

- showing availability of the ILES with high-resolution method to a complex fuel jet mixing flow, and
- describing combinations of ILES turbulent flow with slow and fast chemical reactions.

Also, this work contributed to knowledge of fluid physics by:

- showing effects of a wide range of Atwood number and fluid properties on fuel jet flows.

5.2 Suggestions for Future Work

For non chemical reactive flows the ILES with high-resolution method has already showed promising capability and this work gives further evidence to these encouraging results: However, some topics are still open to ILES. For example, in the recent TNF workshop [46] some indexes were proposed to examine quality of LES: These depend on turbulent viscosity and so are not available for ILES. Instead an investigation of kinetic energy can be a method to check the quality of ILES and this was described in this work: High computational cost will be required if all flow field (grid point) are to be examined. Regarding the numerical simulation of mixing flows of fuel jets, detail investigations of transport properties can be an interesting topic. In this work, diffusion terms in volume fraction equations were neglected as these terms are usually small compared to turbulent diffusion terms, but in multi-species flows the effect of Schmidt number (or Lewis number) is not well understood for ILES.

For combustion flows more issues are open to ILES. Whether the ILES method can truly mimic the subgrid scale models for species and energy equations still requires further evidence. And, the major challenge is in the chemical source term. In order to represent the filtered chemical source term some models have been proposed in LES, e.g., a linear eddy model and a presumed density function model. Therefore, investigations of these methods combined with ILES can result in contributions to both numerical methods and flow physics.

Bibliography

[1] S. Ahmed, R. Balachandran, T. Marchione, and E. Mastorakos. Spark ignition of turbulent nonpremixed bluff-body flames. *Combustion and Flame*, 151(1-2):366–385, 2007.

[2] Y. Al-Abdeli and A. Masri. Recirculation and flowfield regimes of unconfined non-reacting swirling flows. *Experimental Thermal and Fluid Science*, 27(5):655–665, 2003.

[3] Y. Al-Abdeli and A. Masri. Stability characteristics and flowfields of turbulent non-premixed swirling flames. *Combustion Theory and Modelling*, 7(4):731–766, 2003.

[4] G. Allaire, S. Clerc, and S. Kokh. A five-equation model for the simulation of interfaces between compressible fluids. *Journal of Computational Physics*, 181(2):577–616, 2002.

[5] G. Andrews and D. Bradley. The burning velocity of methane-air mixtures. *Combustion and Flame*, 19(2):275–288, 1972.

[6] D. Balsara and C. Shu. Monotonicity preserving weighted essentially non-oscillatory schemes with increasingly high order of accuracy. *Journal of Computational Physics*, 160(2):405–452, 2000.

[7] J. Bardina, J. Ferzinger, and W.Reynolds. Improved subgrid scale models for large eddy simulation. In *AIAA 13th Fluid and Plasma Dynamics Conference*, AIAA-80-1357, 1980.

[8] R. Barlow, A. Dreizler, J. Frank, J. Janicka, A. Kempf, R. Lindstedt, A. Masri, J. Oefelein, and S. Pope. Proceedings of the ninth international workshop on measurement and computation of turbulent nonpremixed flames, 2008.

[9] J. Bechtel, R. Blint, C. Dasch, and D. Weinberger. Atmospheric pressure premixed hydrocarbon-air flames: Theory and experiment. *Combustion and Flame*, 42:197–213, 1981.

[10] B. Boersma, G. Brethouwer, and F. Nieuwstadt. A numerical investigation on the effect of the inflow conditions on the self-similar region of a round jet. *Physics of Fluids*, 10(4):899–909, 1998.

[11] G. Brown and A. Roshko. On density effects and large structure in turbulent mixing layers. *Journal of Fluid Mechanics*, 64(4):775–816, 1974.

[12] J. Chen, A. Choudhary, B. de Supinski, M. DeVries, E. Hawkes, S. Klasky, W. Liao, K. Ma, J. Mellor-Crummey, N. Podhorszki, R. Sankaran, S. Shende, and C. Yoo. Terascale direct numerical simulations of turbulent combustion using S3D. *Computational Science & Discovery*, 2(1):015001, 2009.

[13] T. Cheng, Y. Chao, D. Wu, T. Yuan, C. Lu, C. Cheng, and J. Chang. Effects of fuel-air mixing on flame structures and NOx emissions in swirling methane jet flames. *Symposium (International) on Combustion*, 27(1):1229–1237, 1998.

[14] Z. Cheng, J. Wehrmeyer, and R. Pitz. Experimental and numerical studies of opposed jet oxygen-enhanced methane diffusion flames. *Combustion Science and Technology*, 178(12):2145–2163, 2006.

[15] B. Dally, D. Fletcher, and A. Masri. Flow and mixing fields of turbulent bluff-body jets and flames. *Combustion Theory and Modelling*, 2(2):193–219, 1998.

[16] B. Dally, A. Masri, R. Barlow, and G. Fiechtner. Instantaneous and mean compositional structure of bluff-body stabilized nonpremixed flames. *Combustion and Flame*, 114(1-2):119–148, 1998.

[17] A. Dicorato, E. Covelli, A. Frassoldati, T. Faravelli, and E. Ranzi. Low emissions bluff-body burner. http://www.fluent.com/about/news/newsletters/04v13i2/s9, accessed in August 2010.

[18] D. Drikakis. Advances in turbulent flow computations using high-resolution methods. *Progress in Aerospace Sciences*, 39(6-7):405–424, 2003.

[19] D. Drikakis, C. Fureby, F. Grinstein, and D. Youngs. Simulation of transition and turbulence decay in the Taylor-Green vortex. *Journal of Turbulence*, 8:N20, 2007.

[20] D. Drikakis, F. Grinstein, and D. Youngs. On the computation of instabilities and symmetry-breaking in fluid mechanics. *Progress in Aerospace Sciences*, 41(8):609–641, 2005.

[21] D. Drikakis, M. Hahn, A. Mosedale, and B. Thornber. Large eddy simulation using high resolution and high order methods. *Philosophical Transactions of the Royal Society of London Series A*, 367, 2009.

[22] D. Drikakis and W. Rider. *High-Resolution Methods for Incompressible and Low-Speed Flows*. Springer, 2005.

[23] G. England, P. Kalt, G. Nathan, and R. Kelso. The effect of density ratio on the near field of a naturally occurring oscillating jet. *Experiments in Fluids*, 48:69–80, 2010.

[24] D. Fletcher, B. Haynes, F. Christo, and S.Joseph. Combustion modelling for an entrained flow biomass gasifier. In *The 1st International Conference on CFD in the Mineral & Metal Processing and Power Generation Industries*, 435-442, 1997.

[25] C. Fureby. ILES and LES of complex engineering turbulent flows. *Journal of Fluids Engineering*, 129(12):1514–1523, 2007.

[26] C. Fureby and F. Grinstein. Large eddy simulation of high-Reynolds-number free and wall-bounded flows. *Journal of Computational Physics*, 181:68–97, 2002.

[27] C. Fureby, F. Grinstein, G. Li, and E. Gutmark. An experimental and computational study of a multi-swirl gas turbine combustor. *Proceedings of the Combustion Institute*, 31(2):3107–3114, 1 2007.

[28] M. Germano, U. Piomelli, P. Moin, and W. Cabot. A dynamic subgrid-scale eddy viscosity model. *Physics of Fluids A*, 3(7):1760–1765, 1991.

[29] S. Ghosal. An analysis of numerical errors in large-eddy simulations of turbulence. *Journal of Computational Physics*, 125(1):187–206, 1996.

[30] J. Gottgens, F. Maussi, and N. Peters. Analytic approximations of burning velocities and flame thicknesses of lean hydrogen, methane, ethylene, ethane, acetylene, and propane flames. *Symposium (International) on Combustion*, 24(1):129–135, 1992.

[31] F. Grinstein. Recent progress on monotone integrated large eddy simulation of free jets. *JSME International Journal, Series B: Fluids and Thermal Engineering*, 49(4):890–898, 2007.

[32] F. Grinstein and C. Fureby. Recent progress on MILES for high Reynolds number flows. *Journal of Fluids Engineering*, 124(4):848–861, 2002.

[33] F. Grinstein and C. Fureby. LES studies of the flow in a swirl gas combustor. *Proceedings of the Combustion Institute*, 30(2):1791–1798, 1 2005.

[34] F. Grinstein and K. Kailasanath. Chemical energy release and dynamics of transitional, reactive shear flows. *Phys.Fluids A*, 4(10):2207–2221, October 1992 1992.

[35] F. Grinstein and K. Kailasanath. Three-dimensional numerical simulations of unsteady reactive square jets,. *Combustion and Flame*, 100(1-2):2–10, 1995.

[36] F. Grinstein, L. Margolin, and W. Rider. *Implicit Large Eddy Simulation: Computing Turbulent Fluid Dynamics*. Cambridge University Press, 2007.

[37] M. Hahn and D. Drikakis. Assessment of large-eddy simulation of internal separated flow. *Journal of Fluids Engineering*, 131(7):071201, 2009.

[38] M. Hahn and D. Drikakis. Implicit large-eddy simulation of swept wing flow using high-resolution methods. *AIAA Journal*, 47(3):618–629, 2009.

[39] A. Harten. High resolution schemes for hyperbolic conservation laws. *Journal of Computational Physics*, 49:357–393, 1983.

[40] H. Hottel and W. Hawthorne. Diffusion in laminar flame jets. *Symposium on Combustion and Flame, and Explosion Phenomena*, 3(1):254–266, 1949.

[41] B. Imine, A. Saber-Bendhina, and O. Imine. Effects of a directed co-flow on a non-reactive turbulent jet with variable density. *Heat and Mass Transfer*, 42:39–50, 2005.

[42] G. Jiang and C. Shu. Efficient implementation of weighted ENO schemes. *Journal of Computational Physics*, 126:202–228, 1996.

[43] W. Jones and R. Lindsteds. Global reaction schemes for hydrocarbon combustion. *Combustion and Flame*, 73:233–249, 1988.

[44] P. Kalt, Y. Al-Abdell, A. Masri, and R. Barlow. Swirling turbulent non-premixed flames of methane: Flow field and compositional structure. *Proceedings of the Combustion Institute*, 29(2):1913–1919, 2002.

[45] A. Kempf. Sydney/Sandia bluff-body and swirl flames. In *Proceedings of the Eighth International Workshop on Measurement and Computation of Turbulent Nonpremixed Flames*, 21-89, 2006.

[46] A. Kempf. Aspects of LES quality. In *Proceedings of the Ninth International Workshop on Measurement and Computation of Turbulent Nonpremixed Flames*, 80-111, 2008.

[47] A. Kempf, R. Lindstedt, and J. Janicka. Large-eddy simulation of a bluff-body stabilized nonpremixed flame. *Combustion and Flame*, 144(1-2):170–189, 2006.

[48] A. Kempf, W. Malalasekera, K. Ranga-Dinesh, and O. Stein. Large eddy simulations of swirling non-premixed flames with flamelet models: A comparison of numerical methods. *Flow, Turbulence and Combustion*, 81(4):523–561, 2008.

[49] J. Kim, P. Moin, and R. Moser. Turbulence statistics in fully developed channel flow at low Reynolds number. *Journal of Fluid Mechanics*, 177(1):133–166, 1987.

[50] K. Kim and C. Kim. Accurate, efficient and monotonic numerical methods for multi-dimensional compressible flows: Part II: Multi-dimensional limiting process. *Journal of Computational Physics*, 208(2):570–615, 2005.

[51] A. Kolmogorov. A refinement of previous hypotheses concerning the local structure of turbulence in a viscous incompressible fluid at high Reynolds number. *Journal of Fluid Mechanics*, 13(1):82–85, 1962.

[52] A. Lefebvre. *Gas Turbine Combustion*. Taylor and Francis, 1998.

[53] X. Liu, S. Osher, and T. Chan. Weighted essentially non-oscillatory schemes. *Journal of Computational Physics*, 115:200–212, 1994.

[54] W. Malalasekera, K Ranga Dinesh, S. Ibrahim, and M. Kirkpatrick. Large eddy simulation of isothermal turbulent swirling jets. *Combustion Science and Technology*, 179(8):1481, 2007.

[55] L. Margolin and W. Rider. A rationale for implicit turbulence modeling. *International Journal for Numerical Methods in Fluids*, 39:821–841, 2001.

[56] L. Margolin, W. Rider, and F. Grinstein. Modeling turbulent flow with implicit LES. *Journal of Turbulence*, 7:N15, 2006.

[57] L. Margolin, P. Smolarkiewicz, and A. Wyszogrodzki. Implicit turbulence modelling for high Reynolds number flows. *Journal of Fluid Engineering*, 124:862–867, 2002.

[58] M. Marklund, R. Tegman, and R. Gebart. A self-consistent CFD-model for pressurised high temperature black liquor gasification. *Journal of the International Flame Research Foundation*, 200801:1–34, 2008.

[59] A. Masri. Bluff body and swirl flames database. http://sydney.edu.au /engineering/aeromech/thermofluids/main_frame.htm accessed in August 2010.

[60] A. Masri and Y. Al-Abdeli. Swirl stabilized jets and flames. In *Proceedings of the Sixth International Workshop on Measurement and Computation of Turbulent Nonpremixed Flames*, 159-171, 2002.

[61] A. Masri, P. Kalt, and R. Barlow. The compositional structure of swirl-stabilised turbulent nonpremixed flames. *Combustion and Flame*, 137(1-2):1–37, 2004.

[62] A. Masri, J. Kelman, and B. Dally. The instantaneous spatial structure of the recirculation zone in bluff-body stabilized flames. *Symposium (International) on Combustion*, 27(1):1031–1038, 1998.

[63] E. Mastorakos, T. Baritaud, and T. Poinsot. Numerical simulations of autoignition in turbulent mixing flows. *Combustion and Flame*, 109:198–223, 1997.

[64] W. Meier, O. Keck, B. Noll, O. Kunz, and W. Stricker. Investigations in the TECFLAM swirling diffusion flame: Laser Raman measurements and CFD calculations. *Applied Physics B: Lasers and Optics*, 71(5):725–731, 2000.

[65] B. Merci, D. Roekaerts, B. Naud, and S. Pope. Comparative study of micromixing models in transported scalar PDF simulations of turbulent nonpremixed bluff body flames. *Combustion and Flame*, 146(1-2):109–130, 7 2006.

[66] S. Murugappan and E. Gutmark. A novel swirling injector for improving mixing in high speed flows. In *Proceedings of 39th AIAA/ASME/SAE/ASEE Joint Propulsion Conference and Exhibit*, AIAA-2003-4785, 2003.

[67] A. Olivani, G. Solero, F. Cozzi, and A. Coghe. Near field flow structure of isothermal swirling flows and reacting non-premixed swirling flames. *Experimental Thermal and Fluid Science*, 31(5):427–436, 2007.

[68] N. Peters. Numerical and asymptotic analysis of systematically reduced reaction schemes for hydrocarbon flames. In *Numerical simulation of combustion phenomena*, pages 90–109. Springer-Verlag, 1985.

[69] N. Peters. *Turbulent Combustion*. Cambridge University Press, 2000.

[70] H. Pitsch and L. De Lageneste. Large-eddy simulation of premixed turbulent combustion using a level-set approach. *Proceedings of Combustion Institute*, 29:2001–2008, 2002.

[71] T. Poinsot and D. Veynante. *Theoretical and Numerical Combustion*. R. T. Edwards, 2001.

[72] S. Pope. *Turbulent Flows*. Cambridge University Press, 2000.

[73] S. Pope. Ten questions concerning the large-eddy simulation of turbulent flows. *New Journal of Physics*, 6(35):1–24, 2004.

[74] K. Ranga Dinesh and M. Kirkpatrick. Study of jet precession, recirculation and vortex breakdown in turbulent swirling jets using LES. *Computers & Fluids*, 38(6):1232–1242, 6 2009.

[75] R. Read, J. Rogerson, and S. Hochgreb. Relight imaging at low temperature, low pressure conditions. In *Proceedings of the 46th AIAA Aerospace Sciences Meeting and Exhibit*, AIAA-2008-957, 2008.

[76] F. Ricou and D. Spalding. Measurements of entrainment by axisymmetrical turbulent jets. *Journal of Fluid Mechanics*, 11:21–32, 1961.

[77] B. Rogg. Systematically reduced kinetic mechanisms: Sensitivity analysis. In *13th International Colloquium on Dynamics and Explosions and Reactive Systems*, 1991.

[78] E. Ruffin, R. Schiestel, F. Anselmet, M. Amielh, , and L. Fulachier. Investigation of characteristic scales in variable density turbulent jets using a second-order model. *Physics of Fluids*, 6(8):2785–2799, 1994.

[79] R. Sankaran, E. Hawkes, J. Chen, T. Lu, and C. Law. Structure of a spatially developing turbulent lean methane-air Bunsen flame. *Proceedings of the Combustion Institute*, 31:1291–1298, 2007.

[80] L. Selle, G. Lartigue, T. Poinsot, R. Koch, K. Schildmacher, W. Krebs, B. Prade, P. Kaufmann, and D. Veynante. Compressible large eddy simulation of turbulent combustion in complex geometry on unstructured meshes. *Combustion and Flame*, 137(4):489–505, 2004.

[81] K. Seshadri and N. Peters. Asymptotic structure and extinction of methane-air diffusion flames. *Combustion and Flame*, 73(1):23–44, 1988.

[82] J. Smagorinsky. General circulation experiments with the primitive equations I. the basic experiment. *Monthly Weather Review*, 91(3):99–164, 1963.

[83] G. Smith, D. Golden, M. Frenklach, N. Moriarty, B. Eiteneer, M. Goldenberg, T. Bowman, R. Hanson, S. Song, W. Gardiner Jr., V. Lissianski, and Z. Qin, http://www.me.berkeley.edu/gri_mech/ accessed in August 2010.

[84] P. Smolarkiewicz and L. Margolin. MPDATA: A finite-difference solver for geophysical flows. *Journal of Computational Physics*, 140:459–480, 1998.

[85] M. Smooke. *Reduced Kinetic Mechanisms and Asymptotic Approximations for Methane-Air Flames*. Springer-Verlag, 1991.

[86] R. Spiteri and S. Ruuth. A new class of optimal high-order strong-stability-preserving time discretization methods. *SIAM Journal on Numerical Analysis*, 40(2):469–491, 2002.

[87] O. Stein and A. Kempf. LES of the sydney swirl flame series: A study of vortex breakdown in isothermal and reacting flows. *Proceedings of the Combustion Institute*, 31(2):1755–1763, 2007.

[88] O. Stein, A. Kempf, and J. Janicka. LES of the sydney swirl flame series: An initial investigation of the fluid dynamics. *Combustion Science and Technology*, 179(1):173–189, 2007.

[89] B. Thornber. *Implicit Large Eddy Simulation for Unsteady Multi-component Compressible Turbulent Flows*. PhD thesis, Cranfield University, 2007.

[90] B. Thornber and D. Drikakis. Implicit large-eddy simulation of a deep cavity using high-resolution methods. *AIAA Journal*, 46(10):2634–2645, 2008.

[91] B. Thornber, D. Drikakis, R. Williams, and D. Youngs. On entropy generation and dissipation of kinetic energy in high-resolution shock-capturing schemes. *Journal of Computational Physics*, 227(10):4853–4872, 2008.

[92] B. Thornber, A. Mosedale, D. Drikakis, D. Youngs, and R. Williams. An improved reconstruction method for compressible flows with low Mach number features. *Journal of Computational Physics*, 227(10):4873–4894, 2008.

[93] E. Toro. *Riemann Solvers and Numerical Methods for Fluid Dynamics Third Edition*. Springer-Verlag, 2009.

[94] B. van Leer. Towards the ultimate conservative difference scheme. II. monotonicity and conservation combined in a second-order scheme. *Journal of Computational Physics*, 14(4):361–370, 1974.

[95] B. van Leer. Towards the ultimate conservative difference scheme. IV. a new approach to numerical convection. *Journal of Computational Physics*, 23(3):276–299, 1977.

[96] L. Vervisch and T. Poinsot. Direct numerical simulation of non-premixed turbulent flames. *Annual Review of Fluid Mechanics*, 30(1):655–691, 1998.

[97] Z. Wang and Y. Andreopoulos. Density and compressibility effects in turbulent subsonic jets part 1: mean velocity field. *Experiments in Fluids*, 48:327–343, 2010.

[98] P. Wilson and M. Andrews. Spectral measurements of Rayleigh-Taylor mixing at small Atwood number. *Physics of Fluids*, 14(3):938–945, 2002.

[99] D. Youngs. Modelling turbulent mixing by Rayleigh-Taylor instability. *Physica D: Nonlinear Phenomena*, 37:270–287, 1989.

[100] D. Youngs. Numerical simulation of mixing by Rayleigh-Taylor and Richtmyer-Meshkov instabilities. *Laser and Particle Beams*, 12:725–750, 1994.